Development of high surface area and hydrothermally stable MCM-41 as a potential catalyst for carbon dioxide conversion into carbamates

Ahmad Rafiq

A thesis submitted in the partial fulfilment of the requirements of Teesside University for the Degree of Doctor of Philosophy

May 2019

Abstract

MCM-41 is a mesoporous silica molecular sieve with very high surface area, narrow pore size distributions and simple pore size engineering which makes it potential catalyst support for the eco-friendly CO_2 conversion into carbamates using alkyl halides and amines. Despite all the merits, MCM-41 suffers a lack of hydrothermal stability. The highly ordered pore-network of MCM-41 collapses when MCM-41 comes in contact with moisture. In this work, highly ordered MCM-41 having high hydrothermal stability was prepared using tetraalkylammonium bromide salts and post-synthesis hydrothermal treatment. Powder X-ray diffraction results confirmed the presence of a highly ordered characteristic hexagonal MCM-41 structure. Nitrogen physisorption analysis revealed an unprecedented ultra-high specific surface area of 3000 m^2g^{-1}, calculated using the Brunauer-Emmett-Teller (BET) method and a very narrow pore size distributions (2.6-3.7nm) calculated by the Barrett-Joyner-Halenda (BJH) model. The pore-wall thickness of MCM-41 was found to be 2 nm. The MCM-41 material synthesised exhibited high hydrothermal stability by retaining its structure after boiling in water for 48 hours which is the highest hydrothermal stability reported to date. The most hydrothermally stable MCM-41 samples reported in the literature showed a structural decline after 12-24 hours boiling in water. The ultrahigh surface area MCM-41 thus prepared was impregnated with vanadium using the wet impregnation technique. The wide-angle X-ray diffractograms revealed an extremely uniform dispersion of V species without any degradation of MCM-41 structure. In future, the vanadium impregnated MCM-41 synthesised in this research can potentially be employed as a catalyst for the conversion of

CO_2 into carbamates and many other useful chemicals. Due to its high surface area, MCM-41 prepared in this work can also be impregnated with other potential catalysts such as ammines and metal oxides associated with CO_2 conversions. MCM-41 can also be exploited for carbon capture and storage.

Declaration

The work contained in this thesis is entirely my original work, except where otherwise stated and has not been submitted for another degree anywhere else.

I certify that the statement above is correct

Ahmad Rafiq

List of Figures

List of Tables

Table of Contents

Acknowledgement

It has been a great privilege to have completed my PhD with one of the best supervisors at the Teesside University, Professor Maria Olea and Dr Joseph McGinnis. Completing my PhD under such sincere and dedicated supervisors is a cherished experience. I want to express my sincere gratitude to Professor Maria Olea for providing me with the opportunity to be a part of her research team since 2009.

I am also very grateful to Dr Joseph McGinnis for the diligent and meticulous feedback he has always provided on my research work. During the last and the most challenging year of my PhD, it was Dr Joseph's dedication and Professor Maria's encouragement, which enabled me to complete my thesis. My supervisors offered me a priceless wealth of knowledge. However, the most valuable benefits I have always enjoyed from my supervisors are their dedication, selflessness and sincerity.

Chapter 1

Introduction

1.1 Background

Explosive growth in the scientific developments and thriving human population call for an ever-increasing demand for energy. The International Energy Outlook 2016 Reference Case (IEO2016) reports electricity as the world's chief source and rapidly growing form of end-use energy consumption. World's net electricity generation is predicted to increase up to 69% by 2040 in the IEO 2016 (from 21.6 trillion kilowatt-hours (kWh) in 2012 to 25.8 trillion kWh in 2020 and 36.5 trillion kWh in 2040) (U.S. Energy Information Administration (2016)).

Energy sources employed to generate electricity fall in two categories, non-renewable sources and renewable sources. Non-renewable sources include coal, natural gas and petroleum liquids. The idea of renewable energy sources came on the horizon of the scientific world at the end of the 20^{th} century when the increase in the greenhouse gases emissions raised environmental concerns. The primary cause of greenhouse gas emissions is fossil fuel combustion in transport and power generation sector. The scientific community is, therefore, endeavouring to develop strategies to incorporate renewable energy sources for power generation to reduce CO_2 emission. Renewable energy sources are either completely CO_2 neutral (solar, wind and hydropower) or produce lesser emissions (Biofuels) than fossil fuels.

Renewable energy sources are replenished naturally within the human life span. These sources include wind, water and sunlight which replenish spontaneously in a short timescale, unlike non-renewable sources which take millions of years to regenerate, e.g. petroleum, gas and coal. Renewable energy sources are the fastest-growing energy sources with an anticipated steady annual increase from 2012 to 2040.

Natural gas and nuclear power are the second and third fastest-growing sources of energy besides renewable energy sources, from 2012 to 2040 (U.S. Energy Information Administration (2016)). Natural gas has a higher calorific value than coal, and it is comparatively a cleaner option among fossil fuels because of low emissions. Natural gas is, therefore, expected to remain a much-preferred option among non-renewable sources. U.S. Energy Information Administration, as of 2016, predicts the global natural gas consumption to increase from 3.4 trillion cubic meters in 2012 to 5.7 trillion cubic meters in 2040.

Figure 1.1 Energy Sources Projection fuels (U.S. Energy Information Administration (2016))

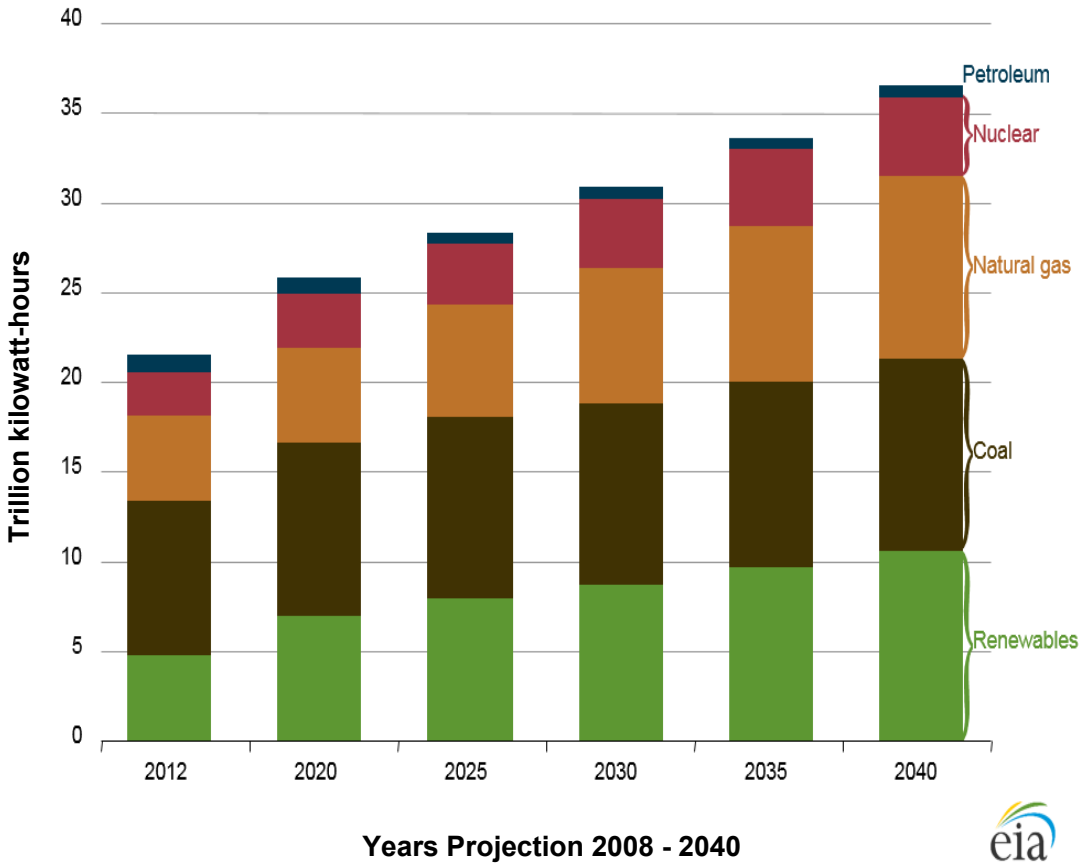

Figure 1.1 shows the utilisation of renewable energy sources is expected to increase over the coming decades beside the non-renewable energy sources, which will continue to rule the energy markets. Annual Energy Outlook Reference Case 2019 published by the U.S. Energy Information Administration (EIA) further explains the trend; the employment of renewables is expected to increase from 18% to 31% from 2010 to 2050 while the consumption of coal and nuclear power (non-renewables) is anticipated to decline. Demand of natural gas, due to its abundance in many regions of the world, high calorific value, attractive industrial tariffs and low capital costs of gas-fired plants, is expected to increase (34% to 39%) in its exploitation as an energy resource hence, predicted to be the most

preferred non-renewable option according to projections till 2050 as shown in Figure 1.2

Figure 1.2 Electricity generation from selected fuels (U.S. Energy Information Administration (2019))

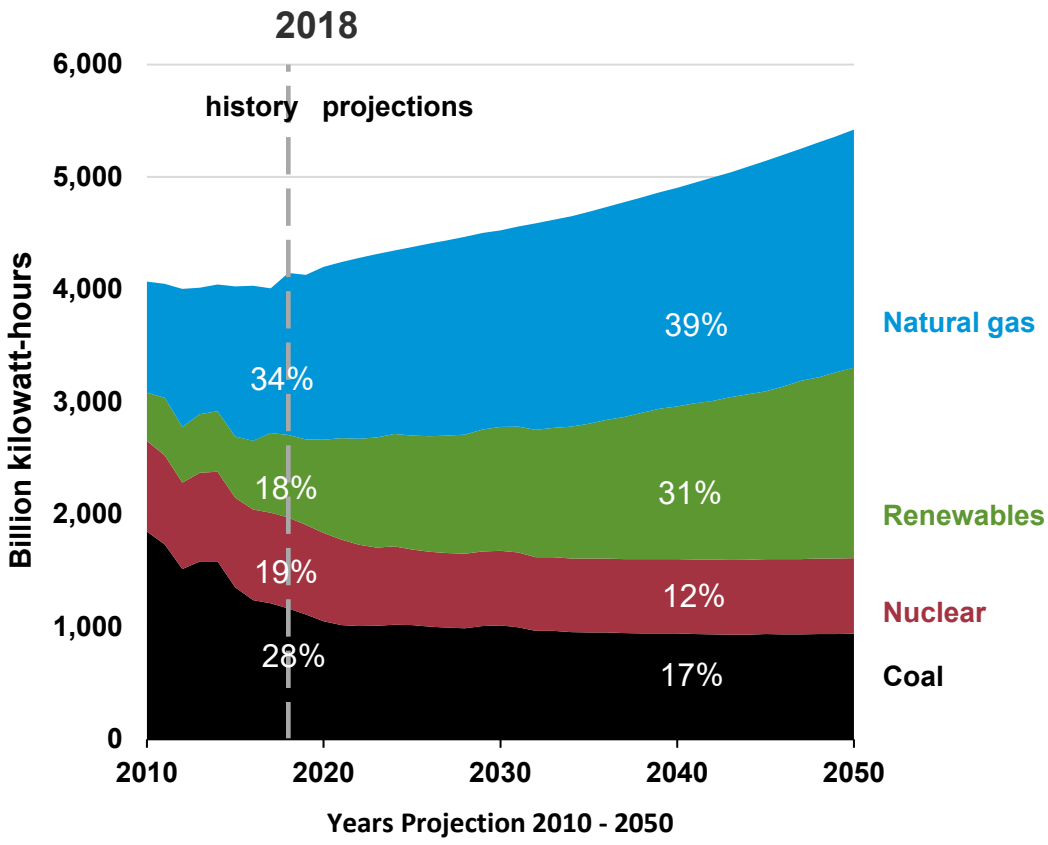

Contribution of renewable energy sources is projected to increase by 2050 with solar, wind and hydroelectric power to be the main contributors as shown in Figure 1.3.

Figure 1.3 Renewable electricity generation, including end-use (U.S. Energy Information Administration (2019))

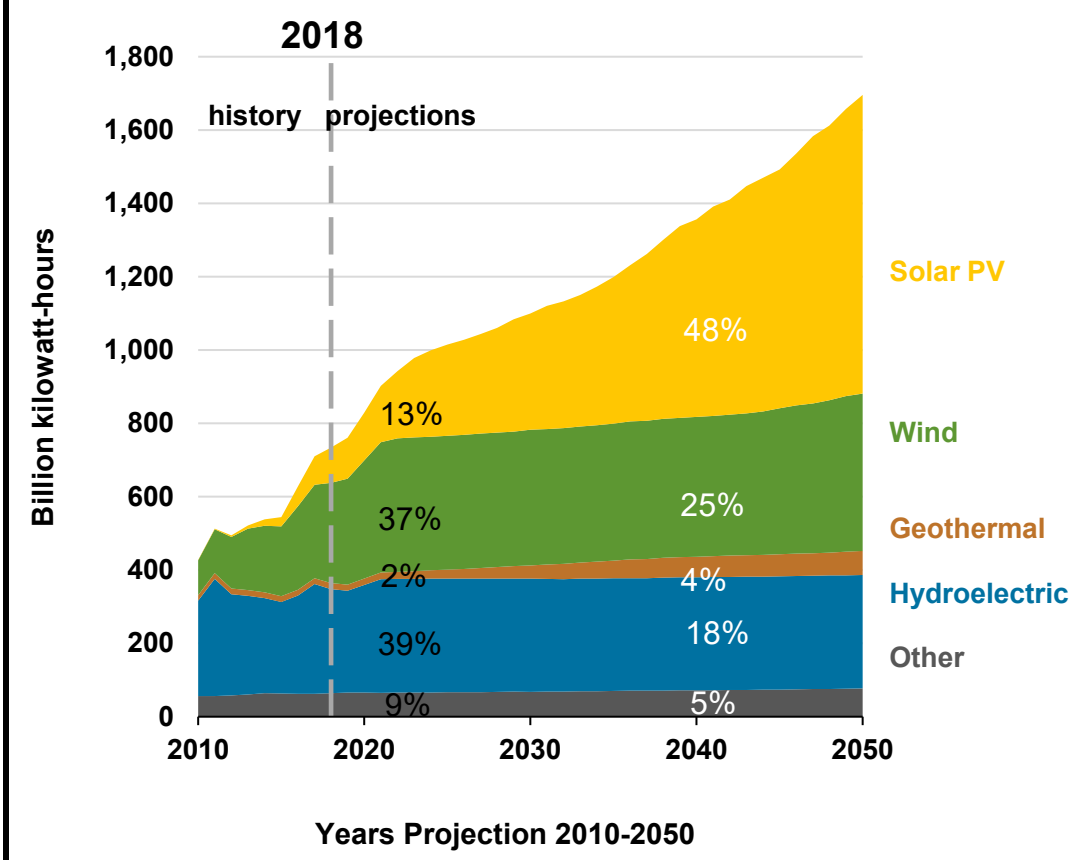

It is evident from the reference cases 2016 and 2019 projections discussed above that fossil fuels are forecasted to predominantly rule the power generation sectors resulting in more and more CO_2 emission into the atmosphere.

1.2 The Research problem

Section 1.2 is devoted to the problems brought up by the current energy generation and energy utilisation system and the strategies to address these problems. The primary concern raised by the present energy system is CO_2 emission due to fossil fuel combustion. Replacing the non-renewables with renewables is an extremely time-intensive process which can take decades to be only partially effective. According to U.S. Energy Information Administration (2016), non-hydropower renewables such as solar and wind power accounted for 5% of total world generation in 2012; their share in 2040 is anticipated to be 14%, most of it coming from wind power. The problem of CO_2 emissions, however, needs quick solutions to curb the increasing amount of CO_2 in the atmosphere.

1.2.1 Carbon dioxide emission

CO_2 released in the environment is causing severe environmental concerns like global warming and greenhouse effect. Although fossil fuel combustion for power generation makes a significant contribution to CO_2 emission, this is not the only mean by which CO_2 pollutes the environment. The sources of CO_2 emission fall in three major categories; stationary, mobile and natural sources as listed in Table 1.1 (Song, 2002 and 2006).

Table 1.1 Major Sources of CO_2 emission (Song, 2002 and 2006)		
Sources	**Causes**	***Description***
Stationary sources	Electrical power generation plant	Fossil fuel combustion. Inefficient energy generation and energy management.
	Process and manufacturing plants	Sugar industry, steel industry and cement industry are the prime examples. The cement industry makes the highest contribution to CO_2 emission in the industrial sector.
Mobile sources	Agricultural machinery	Tractors, and other cultivation, irrigation and harvesting heavy machinery used in modern world agriculture.
	Construction machinery	All the heavy machinery used in the erection of buildings from small houses to skyscrapers.
Natural sources	Humans, animals and plants, earthquakes and volcanic eruptions.	CO_2 is necessary for the presence of life on this environment; plants utilise it in photosynthesis, and hence CO_2 becomes the base of the whole food chain on this planet. The production of CO_2 from natural sources is part of the CO_2 cycle on earth.

Continuous emission of CO_2 from these sources is causing severe environmental implications. The increase in the atmospheric concentration of CO_2 was only 15 ppm from 1000 A.D to 1900 A.D based on the Antarctic ice core data (Song, 2006; Mauna Loa Observatory, Hawaii, 2019). Figure 1.4 illustrates that the concentration of atmospheric CO_2, as recorded by Mauna Loa Observatory and Scripps Institution of Oceanography (SIO), has risen dramatically from 1960 to 2019.

Figure 1.4 Atmospheric CO_2 records at Mauna Loa Observatory, Hawaii 2019

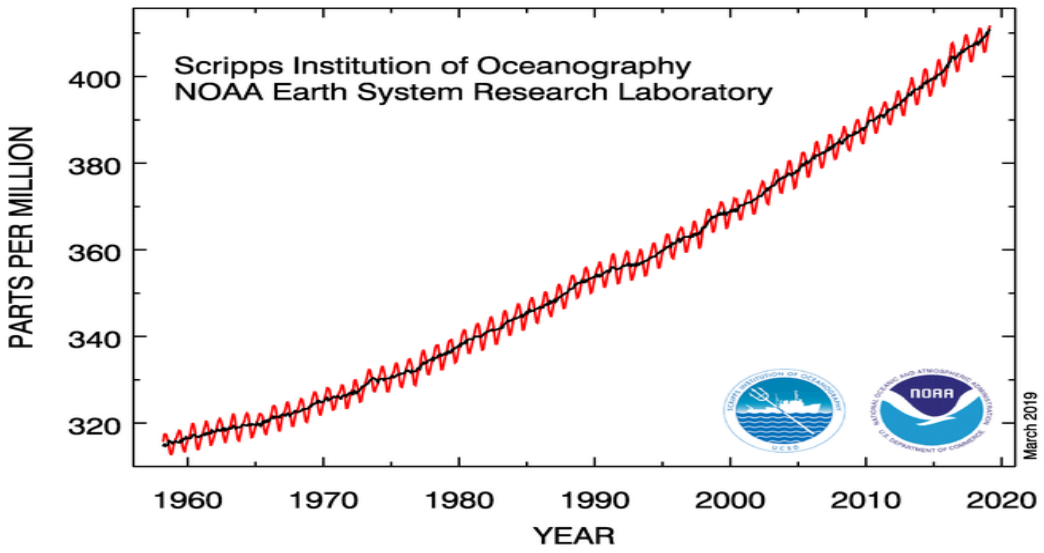

Figure 1.5 Atmospheric CO_2 records at Mauna Loa Observatory, Hawaii 2019

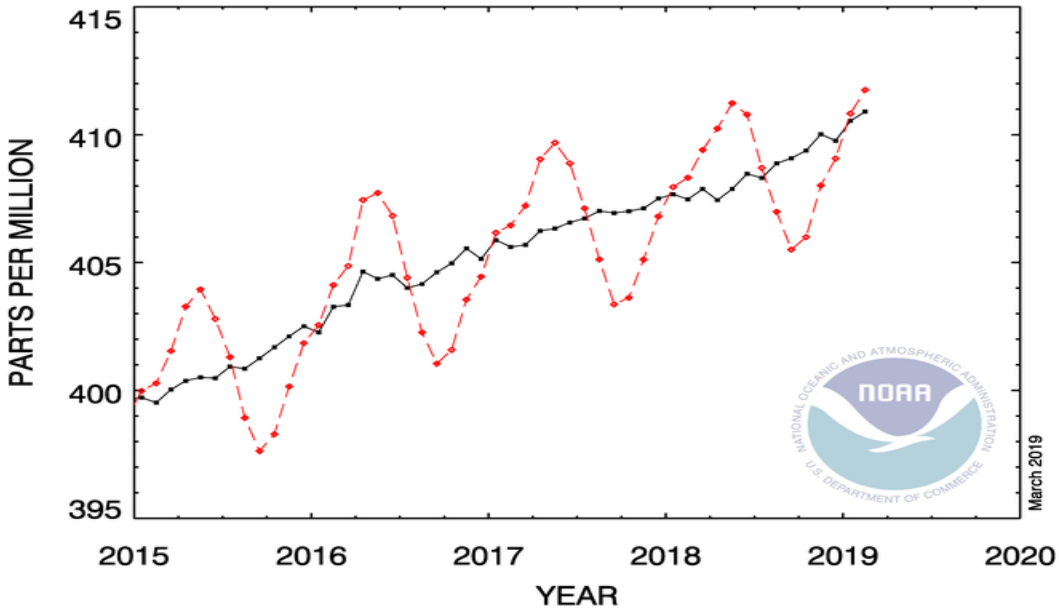

Figure 1.5 provides a further understanding of the alarming increase in the amount of CO_2 in the environment; the concentration of CO_2 between February 2018 and February 2019 increased from 408 ppm to 411 ppm. Such a steady increase in the amount of CO_2 in the atmosphere is a massive concern to the environment which requires the scientific community to evolve processes and technologies that are energy efficient and develop strategies to fix the amount of CO_2 released to the atmosphere. Beside fossil fuel combustion, increase in overall world population during the 20^{th} century is another cause of increased CO_2 concentration. More people means more energy consumption in respect to the modern amenities, industries and facilities available in modern societies. Overall world population is thriving; hence, more energy is required to maintain the standards and necessities of life in the 21^{st} century. The issues of fossil fuel depletion and CO_2 atmospheric concentrations suggest the reorganisation of the whole energy utilisation and energy management system based on green technologies and environmentally benign processes to save the environment.

1.3 Proposed solution

1.3.1 CO_2 Management and Utilisation

Energy utilisation (generation and consumption) is governed by the Carnot Cycle, which establishes the fact that even under ideal conditions, energy cannot be fully utilised with 100% efficiency. According to U.S Energy Information and Administration (IEA) report in 2003, electric power generation plants dissipated 65% of the energy input as conversion loss. The overall energy efficiency of the transport sector is much lower than the electric power generation plants. Hence, the current energy generation system wastes 65 to 80% of energy input before utilisation into the output (Song, 2002 and 2006). This inefficient energy

generation and utilisation system have created a so-called "natural link" between energy utilisation and increasing CO_2 emissions. The biggest challenge of the 21st century is, therefore, to decouple the spontaneous link between CO_2 emission and energy utilisation by supplying the world with renewable energy resources and green electricity, e.g. solar, wind and hydroelectricity. Hence, to improve energy management and energy utilisation, it is required to improve the energy efficiency of the existing system. Inventing new processes and technologies capable of overcoming the existing thermodynamic efficiencies and replacing them for the existing ones, or by modifying the current technologies to reduce the energy dissipation and conversion losses, e.g. using energy-saving electrical appliances and efficient industrial processes can help curb the problem of CO_2 emissions. Table 1.2 illustrates the list of challenges and the strategies to cope with the CO_2 emission problem.

It is evident from the above discussion that the so-called "natural link" between energy utilisation and CO_2 emission is due to the vast consumption of fossil fuels as input for energy generation. However, fossil fuels are the most economical fuels in today's world, and for this reason, fossil fuels will remain as the primary source of energy in the foreseeable future. The alarming rate of increase in atmospheric CO_2 concentration dictates that it is high time to avail renewable energy resources even if they are slightly uneconomical because they are beneficial in the longer run. Using hydrogen as an energy source is considered as the most useful and practical option because it can decouple the so-called "natural link" between energy utilisation and environmental pollution. Hydrogen fuel is practically zero-emission fuel which provides energy with no polluting by-products but pure water.

Table 1.2 Challenges and Possible Strategies for CO_2 Management (Song, 2002 and 2006)			
S. No.	**Energy Challenges for the 21st century**	**Possible Solution**	**Example in Present Scenario**
1	Energy generation and utilisation with little or no emission.	Green fuels and electricity with little or no CO_2 emission	Hydroelectricity, solar electricity, wind, wave and geothermal energy
2	Curb the environmental pollution problem	Reduction in CO_2 emission	Fuels with higher hydrogen to carbon ratio release less CO_2 for more energy.
		Improvement in industrial processes	Solar heat to provide heat for endothermic chemical processes. Selective catalysts to minimise the CO_2 production right at the source
		CO_2 capture and storage, sequestration and utilisation in other processes	Enhanced oil recovery
3	Improving the energy efficiencies of current energy utilisation system.	Develop new systems capable of overcoming the present energy conversion limitations	Energy-saving appliances
4	Renewable energy sources	Increase the utilisation and of renewable energy sources and production of biofuels	Converting Biomass into fuels (Biodiesel, Biogas)
5	Utilising CO_2 in the carbon-based feedstock.	Chemical conversion of CO_2 into other useful chemicals	The polymerisation of CO_2 into polycarbonates and polyurethanes, Dry reforming and other chemicals

Using wind, wave, solar energy and hydropower as renewable energy sources is a useful idea. Although these options do not pollute the environment and are safely practised in many countries worldwide, their application is limited. The power generation from a renewable energy source depends on its availability; for example, some areas of the world may enjoy better solar exposure and others have more wind power than hydro and solar power. A term called "Capacity Factor" is helpful to understand the situation as mentioned above. Capacity factor

is the unit less ratio of actual electrical energy output over a given period to the maximum possible electrical energy output over that period. The maximum energy output of a given power plant is its continuous operation at full capacity for a given time. The capacity factor of a power plant can never exceed its availability factor, which is the time the plant is available to produce power. The availability factor and the capacity factor cannot be high for renewable sources. The solar capacity factors are better in South Asia and parts of Africa, and the wind capacity factors are better in Australia and New Zealand. The average five-year solar capacity factor for the United States is 15% whereas for Canada its only 6%. The average wind power capacity factor in the U.S. was 30% from 2008 to 2012, whereas in China for the same period it was only 18%. Russia has only 3% wind capacity factor. The capacity factors for the Nuclear power plants are the least variable and therefore the highest. Between 2008 and 2012 in the U.S., the baseline nuclear power plant capacity factor was 90% because the nuclear plants are operational almost the whole year. China's reported coal-powered plants capacity factor was 51% from 2008 to 2012 (U.S. Energy Information Administration (2016)).

The above discussion makes it clear that the consumption of fossil fuels in the foreseeable future is inevitable, and they will continue to dominate the power generation sector. The new energy utilisation system should, therefore, comprise of all the available options for renewable energy production as well as CO_2 management to handle the increasing amount of CO_2 in the atmosphere. Entirely replacing or modifying the existing energy utilisation system is a time-intensive process, technologies in this field are nascent with slower progress rates; time,

however, demands some instant solution to manage CO_2 concentration in earth's atmosphere.

Conversion of CO_2 into other useful chemicals is another valuable idea which can provide an instant solution to impede the increasing CO_2 in the environment. CO_2 conversion can contribute to the CO_2 management as well as provide the industries with an abundant and cheaper C_1 feedstock. Carbon dioxide chemical conversion is a field with many gaps, and the scope to fill in the gaps is vast. In the past, utilisation of CO_2 into useful chemicals had been hampered by the facts that the cost of CO_2 capture, its separation, transportation and purification were very costly. Chemical conversion of CO_2 appears to be a less attractive venue for investment due to the high stability of the CO_2 molecule, enormous energy requirements and costly co-reactants, e.g. H_2 and CH_4. The best possible strategy is to utilise CO_2 to replace other hazardous materials, thus adding value to CO_2 chemical conversion. Conversion of CO_2 has many merits over other CO_2 management options. Using renewable energy resources, as mentioned above, has limitations, and it is a time-intensive process. Utilising wind and hydropower may cause severe ecological perturbation in the longer run; for instance, using wind energy can perturb birds' natural habitat and migration patterns, hydroelectricity generation can have impacts on aquatic life (Song, C.S., 2002 and 2006). Biofuels seem a quite attractive and economical option, but these are also not wholly CO_2 neutral.

Nature presents a useful strategy for the conservation of the environmental balance of CO_2 in the process of photosynthesis. In the process of photosynthesis H_2O is converted to oxygen and hydrogen, the latter in the form of the reduced species NADPH (the reduced form of nicotinamide adenine dinucleotide

phosphate, NADP+). This reaction occurs in the thylakoid membranes of chloroplasts of green plants, and some microorganisms like algae and cyanobacteria. The reduced species, NADPH have the energy from the captured light stored in the form of chemical bonds. NADPH, in turn, is transferred to the stroma of the chloroplast, where reaction with CO_2 occurs as shown below.

$$6CO_2 + 12NADPH + 12H^+ \rightarrow C_6H_{12}O_6 + 12NADP^+ + 6H_2O$$

Nature serves as a model and source for inspiration. For hundreds of years, CO_2 balance on earth has been maintained by plants and other microorganisms through chemical conversions. It is, therefore, a useful idea to convert CO_2 into other chemicals and thus contributing to fixing the CO_2 in the atmosphere.

1.4 Conclusion

The above discussion concludes that despite the endeavours to incorporate renewable energy resources, fossil fuels will remain the primary source of energy in the foreseeable future. It is required to adopt strategies that can efficiently reduce the ever-increasing CO_2 in the atmosphere. Conversion of CO_2 into other useful chemicals is a valuable idea of utilising Carbon dioxide as a C_1 feedstock to be converted into other chemicals like carbamates and polycarbonate. The amount of CO_2 in the global atmosphere is continuously increasing, and the amount of "C" feedstock currently utilised in the manufacture of various organic materials and chemicals is far less than the amount of CO_2 expelled by the industrial sector and power plants. Nearly 110 million tonnes per year of carbon dioxide is used as the feed for production of limited chemicals such as urea, methanol, polycarbonates, cyclic carbonates and other chemicals while the global emission is more than 30 Gigatonnes for 2016 as shown in Figure 1.6 (Zangeneh *et al*., 2011).

Figure 1.6 Global Carbon Dioxide Emissions (U.S Energy Information and Administration IEO2016, 2016)

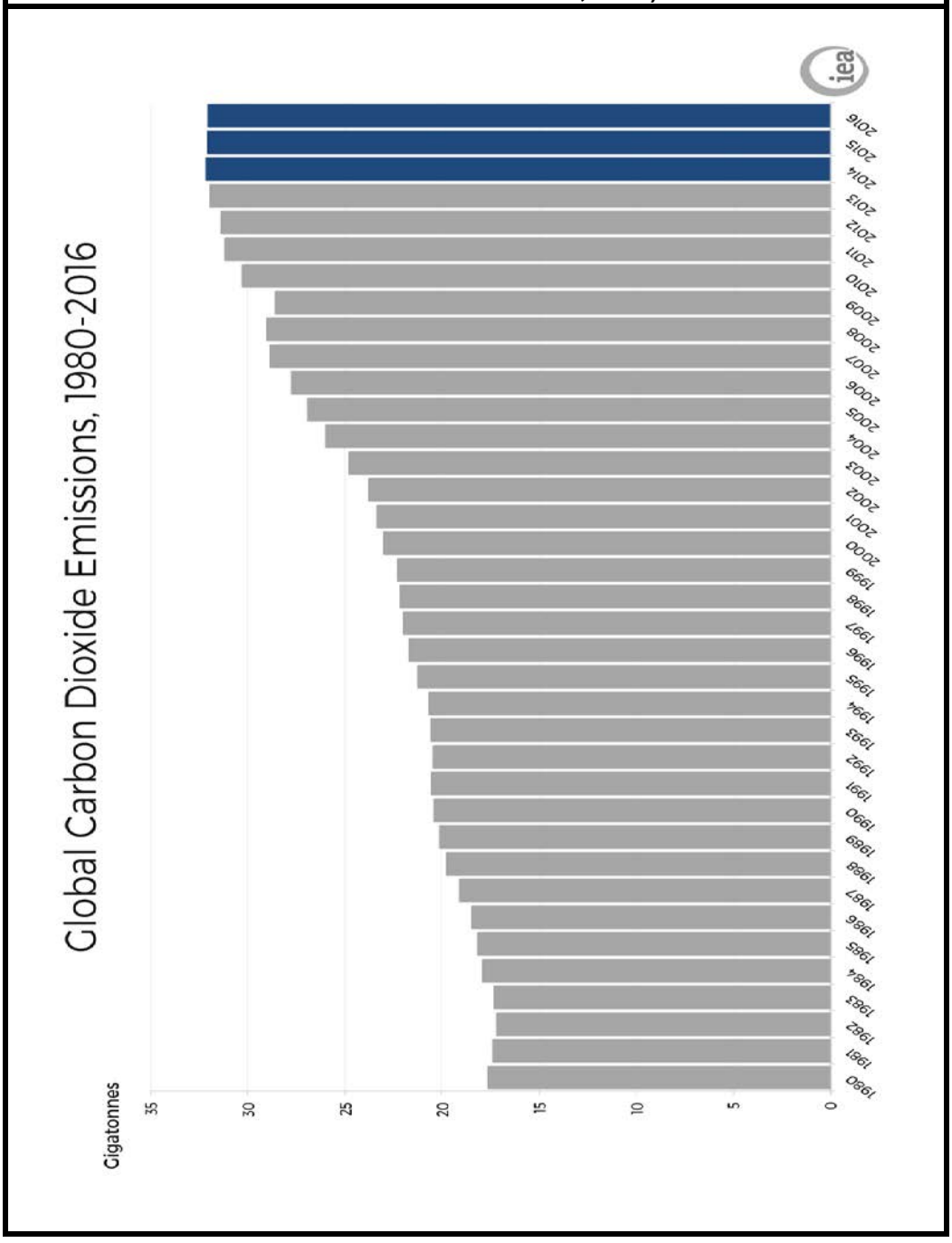

References

Mauna Loa Observatory, Hawaii. (2019) *Earth System Research Laboratory Global Monitoring Division.* Available at: https://www.esrl.noaa.gov/gmd/ccgg/trends/full.html. (Accessed: March 2019).

Song, C.S. (2002) 'CO_2 Conversion and utilization: an overview', *Energy and Fuels*, 16(5), pp. 1329.

Song, C.S. (2006) 'Global challenges and strategies for control, conversion and utilization of CO_2 for sustainable development involving energy', *Catalysis Today*, 115(1-4), pp. 2.

U.S Energy Information and Administration (2016) *International Energy Outlook 2016*. Available at www.eia.gov/forecasts/ieo (Accessed: 23 March 2017)

U.S Energy Information and Administration (2019*) Annual Energy Outlook 2018*. Available at www.eia.gov/aeo (Accessed: 06March 2019)

Zangeneh, F.T., Sahebdelfar, S. and Ravanchi, M.T. (2011) 'Conversion of carbon dioxide to valuable petrochemicals: An approach to clean development mechanism,' *Journal of Natural Gas Chemistry* 20(3), pp. 219.

Chapter 2

Literature Survey

2.1 Background

Carbon dioxide is not merely an undesired greenhouse gas. Its presence in the atmosphere is essential to the earth's ecological system. CO_2's inherent capacity to trap sunlight helps in maintaining the warmth of the atmosphere, without CO_2 earth would be all frozen (Halmann & Steinberg, 1999). CO_2 also serves as a raw material for the process of photosynthesis in plants to make their food hence commencing the food chain on earth (Griffin and Seemann, 1996). A fixed amount of CO_2 is, therefore, vital for the continuation of life on earth. The natural carbon cycle is responsible for fixing the amount of carbon or ultimately, carbon dioxide in the atmosphere (Aresta *et al.,* 2007). CO_2 can potentially contribute as a cheaper, harmless, inflammable and abundant C_1 feedstock in the synthesis of organic chemicals and synthetic materials. The amount of carbon dioxide emitted in the flue gases from the industries is much higher than the amount of "C" (carbon feedstock) currently utilised for manufacturing chemicals, organic materials and liquid transportation fuels (Zangeneh *et al.*, 2011). The most concentrated sources of CO_2 include flue gas from electrical power generation plants, effluents from the partial oxidation units in petrochemical plants, effluents from gasification units and water-gas-shift unit in NH_3 and H_2 manufacturing plants. The CO_2 stream from these plants can be supplemented with captured CO_2 for the production of useful chemicals (Song, C.S., 2002 and 2006).

2.2 CO_2 Utilisation into Useful Chemicals

2.2.1 Carbon dioxide reactivity

Carbon dioxide can react in several modes to serve as a C_1 feedstock. In C-C synthesis reactions, C in the polarised carbonyl group (C=O) of CO_2 may act as an electrophile by linking up with the nucleophilic C in the substrate molecule.

$$:\ddot{O}=C^{+}=\ddot{O}: \quad + \quad R^{-}-MgX \quad \rightarrow \quad RCOOMgX \quad \rightarrow \quad RCOOH \quad \text{(Eq. 1)}$$

Due to the higher electronegativity of two oxygen atoms, the electron density tends to be closer to the O atoms, the electron-deficient C atom (in CO_2) thus acts as an electrophile and reacts with the nucleophilic carbon atom in the Grignard's Reagent to form an unstable intermediate which ultimately yields a carboxylic acid. Alternatively, the CO_2 molecule can be activated by electron transfer to the CO_2 molecule, resulting in a polarity inversion termed as "*Umpolung"*. The nucleophilic character bearing CO_2 molecule (after polarity inversion) can react with a carbocation or a proton to give a C-C or C-H bond respectively. For example, the electrolytic reduction of CO_2 with H_2O into formic acid, formaldehyde or methanol, electrons are transferred to CO_2 to form a C-H bond (Lee *et al*., 2015).

$$CO_{2(g)} + 2H^{+}_{(aq)} + 2e^{-} \rightarrow HCOOH_{(aq)} \text{ (eq. 2)}$$

CO_2 thus reacts in two contradicting ways depending on whether CO_2 is provided with the electrons first to attain a nucleophilic character or the electrons are provided to the substrate in which case CO_2 will act as an electrophile. In both cases, it is hard to establish which route is followed by CO_2 because the intermediates are unstable and therefore, short-lived.

CO_2 interaction with transition metals is complex to understand. Figure 2.1 explains the five primary modes of transition metal-CO_2 coordination. In mode 1, a metalo-acid derivative is formed by the donation of electrons from the metal to the C atom. In mode 2, CO_2 donates its paired electrons to the metal atom and forms σ bond; as a result, the electron density tends to be higher towards the metal atom.

Figure 2.1 CO_2 activation by transition metals (Huang *et* al., 2010)

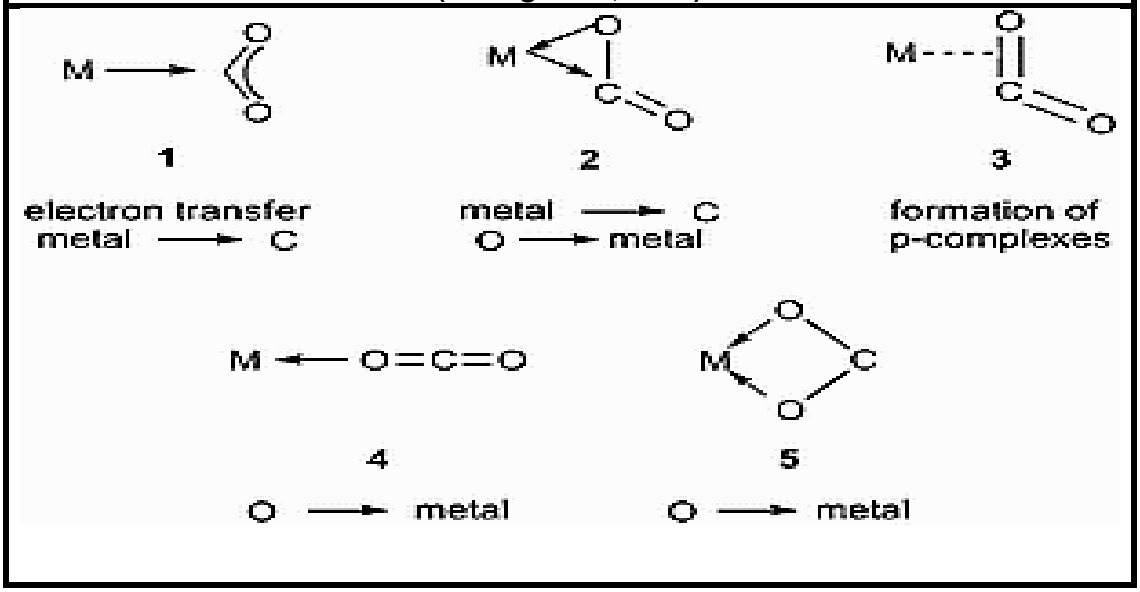

At this stage, the back donation of the excess electron by the metal atom to the empty π-orbital of the CO_2 occurs; hence, the bond between C and O is weakened (CO_2 activation). In mode 3, a π-complex is formed with the coordination of transition metal atom with a C=O double bond. Chelation of O atom in CO_2 molecule to the transition metal centre forms stable metal complexes, as shown in the modes 4 and 5 in Figure 2.1. However, this kind of complexes (mode 4 and 5) are less probable and only occur for compounds with high oxidation states (Huang *et* al., 2010).

There are several possible chemical conversions of CO_2 discussed in the literature, each having its unique benefits (Inui, 1996; Omae, 2006; Song, 2001;

2002 and 2004). Only the significant conversions in heterogeneous catalysis, which not only exploit CO_2 as a feedstock but also replace it with other costly or hazardous raw materials are discussed in the following lines. Whether these conversions can effectively curb the amount of excess CO_2 in the environment is a difficult question to answer; nevertheless, these conversions are eco-friendly and can potentially replace some of the hazardous raw materials with CO_2. The environmentally most benign CO_2 conversions which are of greater interest in the scientific community include dry reforming, tri-reforming, and polymerisation of CO_2.

Dry reforming uses Ni-based catalysts, and noble metal-supported catalysts including Rh, Ru, Pd and Ir. Noble metal catalysts afford good conversion and selectivity, but their high costs and limited availability is a disadvantage to these processes. Another problem is the vast extent of coke formation due to the CO_2 disproportionation reaction and CH_4 cracking under high temperature (600-850^0C) (Rezae *et al*., 2006).

Tri-reforming is a unique process which incorporates all the three methods (steam reforming, dry reforming and partial oxidation) of syn-gas generation synergistically in a single reactor to generate syn-gas with desired H_2/CO ratios (1.5-2.0). A CH_4 conversion of 95% and 84% conversion of CO_2 in tri reforming has been reported on supported nickel catalyst (Song, 2001; 2002 and 2004). The most significant advantage of tri-reforming is a deterrence to carbon formation, making it possible to use supported nickel catalysts rather than expensive noble metals essential for dry reforming (Moon, 2005).

Another useful conversion of CO_2 is polymerisation. CO_2 has two C=O bonds capable of polymer formation by utilising one of the π-bonds to make σ- bond with

other compounds. Polycarbonates, polypyrones, lactone intermediates and polyurethanes can be synthesised using carbon dioxide. Polycarbonates and polyurethanes are the most important class of polymeric materials which have found extensive applications in the modern world. Polycarbonates are known for their transparency and toughness. Polyurethane is a generic name for a large group of synthetic materials having different compositions and correspondingly different characteristic profiles. All polyurethanes are manufactured by the polyaddition of a diisocyanate; however, the characteristic chain link, usually only present to a minor extent, is the urethane group. In most cases, the urethane group links poly-(alkylene ether) or polyester sequence with molecular masses between ca. 200 and 6000. Polyurethane has numerous merits over other plastics and rubbers they possess better abrasion, superior impact resistance and tear-resistance with higher load-bearing capacity. CO_2 utilisation into a polymer with such incredible characteristics will be a significant contribution to the fields of engineering, process and manufacturing industries.

2.2.2 The utilisation of CO_2 in Carbamate synthesis

Organic carbamates and cyclic carbonates are precursors of polyurethanes and polycarbonates, respectively. Conventionally these precursors are manufactured by using poisonous phosgene gas. The carbon atom in phosgene is utilised to bridge two nucleophilic units making it useful for the synthesis of chemicals like urea, carbamates and cyclic carbonates. This research deals with the development of potential catalysts and catalyst supports for organic carbamates synthesis; therefore, only carbamate synthesis is shown below in equations 3 and 4.

Carbamate synthesis:

$$RNH_{2(Amine)} + O = C\ Cl_{2(phosgene)} \xrightarrow{yield} RN = C = O_{(Isocyanate)} + 2HCl \quad \text{(Eq.3)}$$

$$RN = C = O_{(Isocyanate)} + R'OH_{(Alcohol)} \xrightarrow{yield} RNHC(O)OR'_{(Carbamate)} \quad \text{(Eq.4)}$$

Phosgene is a poisonous gas which is linked with some environmental and safety shortcomings like the Bhopal tragedy, happened in 1984 at a methyl isocyanate plant in India. Another drawback of phosgene is the financial penalty it incurs for the removal of chlorine contents as NaCl. NaOH is required for the disposal and conversion of waste salt solutions, aggravating the environmental issues associated with phosgeneous carbamate production (Srivastava *et* al., 2004).

2.2.3 Synthesis of carbamates using CO_2

Carbon dioxide can act as a carbonylating agent instead of phosgene; besides this, carbon dioxide is an abundant and safer option to replace phosgene. Chaturvedi (2012) has discussed a wide range of chemical conversions of CO_2 into carbamates using gaseous as well as supercritical CO_2. There is a wide range of chemicals that have been used alongside CO_2 and amines, and CO_2 alone for carbamate synthesis. Some of the relatively more straightforward conversions are discussed below.

On reaction with amines, CO_2 yields carbamic acid. The reaction is reversible due to the unstable carbamic acid.

$$CO_2 + R - NH_2 \rightleftharpoons R - NH - COOH \quad \text{(Eq. 5)}$$

Carbamates can be synthesised using CO_2, amines and unsaturated ethers. Longer reaction time (70 to 80 hrs), low yield (3 to 12%) and limitation of the synthesis to only secondary aliphatic amines are the drawbacks of this scheme.

$$R_2NH + CO_2 + CH_2 = CH - O - et \longrightarrow R_2N - C - O \quad \text{(Eq. 6)}$$

Alternatively, CO_2 can be reacted with alkyl halides and primary and secondary aliphatic amines to synthesise organic carbamates, as shown in Eq.7. The reaction time (45 hours) is less than that for the scheme in Eq.6, and the yield is slightly higher (6-25%) than the yield from the scheme in Eq.6.

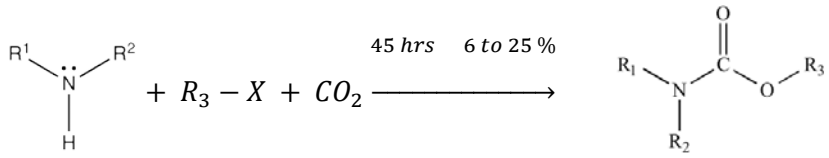

(Eq. 7)

The drawbacks are the same as that for the scheme in Eq.6 except for the reaction-times, and yields are slightly better, i.e. approximately 45 hours of reaction time and 6-25% yield. Heterogeneous catalysis has been used for the conversion of gaseous carbon dioxide into carbamates mentioned above. The challenges heterogeneous catalyst face for these conversions are low yields, recyclability and use of solvents as discussed below.

The conversion of CO_2 into carbamates via Eq.7 proceeds in two steps. The reaction of a primary amine with CO_2 yields the carbamate anion. Carbamic ammonium salt formed in Eq.8 is unstable. In the absence of an efficient catalyst, the alkyl halide reacts with the amine formed by the reverse reaction in Eq.8, resulting in the formation of N-alkylated products as the major products. In the presence of an efficient catalyst, the carbamic ammonium salt is stabilised and reacts with an alkyl halide to yield the corresponding carbamates (Srivastava ***et al***., 2004).

$$2R'NH_2 + CO_2 \rightleftharpoons [R'NHCOO^-][R'NH_3^+] \quad \text{(Eq. 8)}$$

$$[R'NHCOO^-][R'NH_3^+] + RX \quad \rightarrow \quad R'NHCOOR + R'NH_2 + HX \quad \text{(Eq. 9)}$$

Conventional catalysts used for the conversion mentioned above are onium salts, basic-catalysts, sterically hindered organic bases, crown ethers and solid caesium carbonates. The catalysts named above are homogeneous catalysts

except for caesium carbonate, which is a solid catalyst. Caesium carbonate, although a heterogeneous catalyst, only catalyses the reaction when used in substantial quantity. $CsCO_3$ also requires tetrabutylammonium bromide/iodide as co-catalysts to stabilise the carbamate anion to prevent direct N-alkylation and alkylation of the product (Srivastava *et al*., 2004). Heterogeneous catalysts are more desirable than the homogeneous catalysts for several reasons including; ease of separation of reactants and products and the catalyst itself from the mixture of reactants and products, low amount of catalyst is usually required to catalyse the reaction another disadvantage of using the onium salts is their disposal which poses environmental and economic challenges. The challenges to heterogeneous catalysts in the conversion of gaseous CO_2 into carbamates are low yields, low recyclability and use of solvents as discussed in Section 2.3.

2.3 Catalysts for CO_2 Conversion into Carbamates

Li *et al.* (2011) reported several metal oxide catalysts for the synthesis of various alkyl carbamates using gaseous CO_2, ammonia, and alcohols. They found that the V_2O_5 catalysts had shown 98% selectivity and proved to be the most efficient among all the metal oxide catalysts they had used. The V_2O_5 catalysts also exhibited high recyclability the carbamates yields; however, were only 25%. Among the metal oxide catalysts, V_2O_5 was found to be the most efficient catalyst. Srivastava *et al*. (2004; 2005 and 2006) also reported several catalysts for CO_2 utilisation into polymers. Their work emphasised on polycarbonates synthesis; however, they also synthesised carbamates via the above mentioned eco-friendly reaction (Eq.7, Page 23).

2.3.1 Titanosilicates Molecular Sieve and Metal Phthalocyanine Complexes Encapsulated in Zeolite-Y

The reaction proceeds in two steps. The reaction of a primary amine with CO_2 yields the carbamate anion, which reacts with various alkyl halides to give the corresponding carbamates (Srivastava *et al*., 2004).

$$2R'NH_2 + CO_2 \rightleftharpoons [R'NHCOO^-][R'NH_3^+] \quad \text{(Eq. 8)}$$

$$[R'NHCOO^-][R'NH_3^+] + RX \quad \rightarrow \quad R'NHCOOR + R'NH_2 + HX \quad \text{(Eq. 9)}$$

Conventional catalysts for the above reaction are onium salts, basic-catalysts, sterically hindered organic bases, crown ethers and solid caesium carbonate. The reaction of CO_2, aniline and n-butyl halide yields two products; butyl-*N*-phenyl carbamate as the main product while *N, N*-dibutylaniline is also produced as a side product.

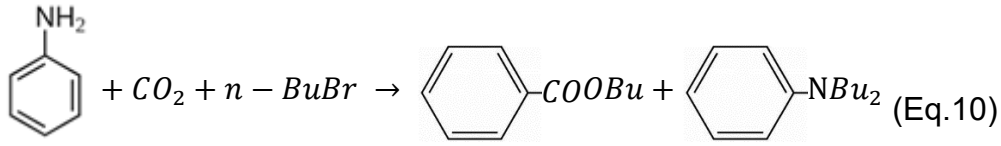

(Eq.10)

Titanosilicates and zeolite encapsulated metal complexes were used as catalysts. The reaction was carried out using solvents; CH_3CN, CH_3OH and strong donor solvent, *N, N*-dimethylformamide (DMF). DMF exhibited the highest aniline conversion (26%) as compared to 5.9 and 3.9 % shown by CH_3CN and CH_3OH respectively. The high solubility of CO_2 in DMF is the main reason for high aniline conversion in DMF solvent. The author has also reported that the carbamate selectivity was also dependent on the solvents. In the absence of solvents, the reaction occurred with *N*, *N*-dibutylaniline (64%) as the major product and carbamate (36%) as the minor product. The selectivity of carbamates was found to be lower in DMF (59%) and higher in case of the other two solvents (90%). Titanosilicates and zeolite encapsulated metal complexes catalysts were

found superior to other solid catalysts, $CsCO_3$ and onium salts. Tetrabutylammonium bromide/iodide is required as co-catalysts along with CsCO3 to stabilise the carbamate anion and avert direct N-alkylation and alkylation of the product. Recovery/recycle/disposal of such onium salts pose environmental and economic challenges which can be avoided with the use of Titanosilicates and zeolite encapsulated metal complex catalysts. These catalysts afford 80% carbamate yield at mild but optimised conditions of temperature and pressure (353K and 3.4bar) with high recyclability and a little loss in catalytic activity.

2.3.2 Zeolite Based Organic-Inorganic Hybrid Catalysts

Srivastava *et al*. (2005) have reported the synthesis of both aryl and alkyl carbamates under mild conditions using the zeolite-based organic-inorganic hybrid catalyst. Synthesis under mild conditions of temperature and pressure are highly desirable for increasing the life expectancy and preserving the activity of the catalyst. A wide range of organic carbamates was synthesised, without any solvent, in high yields using the as-synthesised form of zeolite beta. The principle behind the efficiency of the catalyst lies in the synthesis of the molecular sieves. Microporous and mesoporous molecular sieves are synthesised using various quaternary ammonium surfactants as templates which remain inside the structure of the catalysts unless removed by calcination. An uncalcined catalyst, therefore, has quaternary ammonium ions, present inside the structure which acts as a catalyst for the conversion of CO_2 into carbamates in the presence of alkyl halides and amines. The reaction between a primary amine and CO_2 readily yields ammonium carbamate as shown in Eq. 11.

$$2RNH_2 + CO_2 \rightleftharpoons [RNHCOO^-][RNH_3^+] \qquad \text{(Eq. 11)}$$

The quaternary ammonium ion acts as a catalyst by stabilising the carbamate anion with ion exchange. The equilibrium shifts towards the right side, as shown in Eq. 12 (Srivastava *et al*., 2005).

$[RNHCOO^-][RNH_3^+] + Et_4N^+X \leftrightharpoons [RNHCOO^-][Et_4N^+] + [RNH_3^+X^-]$ (Eq.12)

Further reaction of this stabilised carbamate anion with n-BuBr yields the corresponding alkyl carbamate.

$[RNHCOO^-][Et_4N^+] + [RNH_3^+] + n-BuBr \rightleftharpoons RNHCOO(nBu) + RNH_2 + Et_4N^+X^- + HBr$ (Eq. 13)

In the absence of an efficient catalyst, carbamic ammonium salt would be unstable, and the amine formed by the reverse reaction would react with n-BuBr yielding predominantly the nitrogen-derived products as shown in Eq.14.

$$RNH_2 + nBuBr \xrightarrow{yields} RNH(n-Bu) + HBr \qquad \text{(eq. 14)}$$

The distinguishing features of this catalyst were, high carbamates selectivity (85 to 95 %) over nitrogen derived products (N-alkylated products), it was a single-step process, no solvent was required and the catalysts afforded high recyclability. Furthermore, the high selectivity without requiring any solvent minimised the formation of waste products. The zeolite-based organic-inorganic hybrid catalysts, therefore, followed all the principles of green chemistry.

It should be noted here that the catalyst supports mentioned above are zeolites. The micro-porous dimensions of zeolite pose severe mass transfer limitations when large reactant molecules are involved. This problem is circumvented by improving the zeolite pore size either by reducing the zeolite crystal size or by providing a new mesoporous system inside the microporous zeolite dimensions. However, to overcome the mass transfer limitations of zeolites, it is more logical to replace zeolites altogether with mesoporous materials. Extensive work is

available in the literature on the syntheses of mesoporous materials like SBA-15 and MCM-41. Due to their highly ordered pore network and larger pore sizes than zeolites, these materials have shown reliable results in numerous conversions. The following two catalysts proposed by Srivastava *et al.* (2005 and 2006) are mesoporous materials.

2.3.3 Adenine-modified Ti-SBA-15 Solid Catalysts

Srivastava *et al*. (2005) have reported the adenine modified Ti-SBA-15 as the first organo-functionalized mesoporous titanosilicate catalysts used in the synthesis of carbamates using CO_2 as a raw material. Several amines were reacted with CO_2 and butyl bromide to synthesise alkyl and aryl carbamates, as shown in Table 2.1.

Table 2.1 List of Amines reacted with CO_2 and n-Butyl Bromide (Srivastava *et al.,* 2005)

Amine	Alkyl halide	Cabonylating agent	Carbamate
Aniline	n-Butyl Bromide	CO_2	n-butyl-*N*-phenyl carbamate
2,4,6 Trimethylaniline	n-Butyl Bromide	CO_2	n-butyl-*N*-2,4,6-trimethylphenyl carbamate
Benzylamine	n-Butyl Bromide	CO_2	n-butyl-*N*-methyl phenyl Carbamate
Cyclohexylamine	n-Butyl Bromide	CO_2	n-butyl-*N*-cyclohexyl carbamate
Hexylaniline	n-Butyl Bromide	CO_2	n-butyl-N-hexyl carbamate
Octylamine	n-Butyl Bromide	CO_2	n-butyl-*N*-octyl carbamate.

Owing to the acidic nature of activated CO_2, it can also react with amine (N-H) functionality in adenine modified SBA-15 and adenine modified Ti-SBA-15 to form carbamate. Adenine modified Ti-SBA-15 catalysts rendered a carbamate selectivity 89% without any solvent. SBA-15 alone was found only weakly active

for CO_2 conversion. Upon titanium functionalization, a slight increase in the catalytic activity was reported.

On the other hand, adenine functionalised SBA-15 alone only slightly enhanced catalytic activity. However, when the Ti-SBA-15 was modified with adenine, the selectivity had shown a significant increase. Hence, both Ti and adenine together created a synergistic effect by enhancing the selectivity and accomplishing complete conversion of amines. The author conducted aniline adsorption on different supports and found that the aniline adsorption increases with the incorporation of Ti (Lewis acid). Hence, Ti ions facilitate the adsorption of aniline, and the adenine functionality favours the activation of CO_2.

In the case of carbamate synthesis; Ti-SBA-15-pr-Adenine was successfully recycled three times without any loss in the activity of the catalyst. The activity was severely declined after the third recycle. The author suggested that the decline in the activity was due to the deposition of carbonaceous matter. In polycarbonate synthesis, the catalyst was recycled several times with a small decrease in the selectivity. However, in the absence of solvent, the activity started to decline after each recycling. Although the solvent had shown no significant effect on the activity and selectivity of the catalysts, it was found to increase the life of the catalyst.

2.3.4 Solid as-synthesized MCM-41 Catalyst

Srivastava *et al*. (2006) reported the as-synthesized MCM-41 as the most efficient catalyst for the synthesis of carbamates using CO_2, alkyl halides and amines. The catalyst was found superior to the previous catalysts from Srivastava *et al*. (2004; $2005_{(a)}$ and $2005_{(b)}$) even in the absence of a solvent. The selectivity of the catalysts did not significantly change; however, the most significant merits of

MCM-41 over the other catalysts were, maintaining a very high selectivity without a solvent and its effectiveness for CO_2 conversion even in a small quantity, as shown in Table 2.2 and Table 2.3.

Table 2.2 Comparison of Catalysts for CO_2 Conversion into Carbamates

S.No	Catalysts	Selectivity	Recycles	Amount of catalyst (mg)/mmol substrate
1	Titanosilicate molecular sieve and metal phthalocyanine complexes encapsulated in zeolite-Y.	80-92% (80^0C,3.4 bar) (solvents used)	Not reported	100 / 2
2	Zeolite-based Organic-Inorganic hybrid catalysts.	84-95% (80^0C, 3.4 bar) (solvents used)	Eight.	150/10
3	Adenine-modified Ti-SBA-15 Solid Catalysts.	89% (solvent) (80^0C,3.4 bar)	Three	100 + 0.95 mmol adenine/g catalyst/ 12
4	Solid as-synthesized MCM-41 catalyst.	84-95% (80^0C, 3.4 bar)	Five	50 / 18

Table 2.3 Comparison of Catalysts for CO_2 Conversion into Polycarbonates				
S.No	Catalyst	Selectivity	Recycles	Amount of catalyst (mg)/mmol substrate
1	Zeolite-based Organic-Inorganic hybrid catalysts	88.5-98.2% (no solvent) 98.6% (DMF) 120^0C , 6.9bar	eight	150/18
2	Adenine modified Ti-SBA-15 Solid Catalysts	100% (CH_3CN, CH_3OH) 89.1%(DMF) 120^0C, 6.9 bar	low	100mg+0.95mmol adenine/g catalyst/12
3	Solid as-synthesized MCM-41 catalyst	100% (DMF) 80-93.7% (No solvent) 120^0C, 6.9bar	five	50mg / 18mmol

Quaternary ammonium halides are employed as homogeneous catalysts in industrial processes for the synthesis of cyclo-carbonates and the synthesis of carbamates. The turn-over frequencies defined as the number of moles of the substrate converted per mole of the catalysts per hour (h^{-1}), increases in the following order Me_4N+(12.4) < Et_4N+ (29.9) < Pr_4N+ (42.9) < Bu_4N+ (46.3) < cetyltrimethylammonium ion (52.8). Hence, cetyltrimethylammonium ion affords the highest activity. This ion is present inside the structure of as-synthesized MCM-41 as the surfactant template (cetyltrimethylammonium bromide) and can, therefore, be used in the form of solid as-synthesised MCM-41 catalyst for the conversion of CO_2 into carbamates. The benefit of using as-synthesised MCM-41 over the commercial homogeneous catalysts is its ease of separation. The quaternary ammonium halides, when used as homogeneous catalysts, are soluble in mixtures of reactants and products, therefore, pose separation issues. Sophisticated separation methods are required for the separation of the catalysts and purification of the product making their use a

complex issue in homogeneous catalysis. In this case, solid as-synthesised MCM-41 was separated from the reaction and product mixture by centrifugation only.

2.4 Gaps in the Existing Research

Table 2.2 and Table 2.3 (Page 31) show a comparison of the salient features of each catalyst used in the conversion of CO_2 into carbamates and polycarbonates, respectively. High recyclability of a catalyst is merit, which makes the catalyst more economical for industrial-scale application. The comparison of catalysts shows the zeolite-based organic-inorganic hybrid catalyst sustained eight recycles in the presence of solvents, which is the highest among all the catalysts. However, in the absence of a solvent, the structure of the catalysts was severely deteriorated. Adenine modified Ti-SBA-15 was successfully recycled three times. Solid as-synthesized MCM-41 was recycled five times without any structural deterioration; no solvent was used. Srivastava *et al*. (2006) suggested that the MCM-41 structure played a crucial role in accomplishing high carbamate conversion with a minimal amount of catalysts. It is proposed here that the vital function of MCM-41 structure in CO_2 conversion into carbamates can be exploited to impregnate MCM-41 with other catalytic species such as those mentioned by Li *et al.* (2011). However, it is indispensable to note that MCM-41 used in the aforementioned chemical conversion was in the as-synthesised form, has shown only five successful recycles. The pore structure of the as-synthesised catalyst is supported internally by the hydrophobic core formed by the surfactant micelles during the sol-gel synthesis. After calcination, the hydrophobic core (surfactant template) is lost, MCM-41 structure is devoid of this additional support,

and the structure becomes vulnerable further deterioration. Impregnation of the catalysts can also cause a further decline in the MCM-41 structural stability.

2.5 MCM-41 Synthesis

2.5.1 Mesoporous Materials

Porosity is a feature which confers useful textural characteristics to a solid catalyst, such as high surface area at lower densities, making it suitable for heterogeneous catalysis. Solid materials possess an overwhelming natural tendency to minimise void spaces within their structure, making it difficult to find naturally occurring highly porous materials to fulfil the criteria for a suitable catalyst. Manufacturing highly porous solids capable of catalysing a chemical reaction is an art. A large number of active catalysts can be employed to catalyse chemical reactions. Primarily these include, metals and metal oxide catalysts supported on various catalyst supports like alumina, silica and zeolites. Among the catalysts mentioned above, zeolites afford high selectivity and high conversion due to their highly ordered structure, narrow pore size distribution and very high surface areas. Zeolites are microporous materials having an average pore diameter of the order of a few molecular dimensions, (< 2nm). The smaller pore size of zeolites is mainly responsible for the high selectivity achieved from zeolites. However, these small pore sizes may also cause mass transfer limitations, especially when larger molecules are involved. Mesoporous molecular sieves such as SBA-15 and MCM-41 also possess high surface areas, highly ordered structure and narrow pore size distribution, but the average pore diameter (2-50 nm) is more significant than that of zeolites. Hence, the mass transfer limitations of zeolites can be overcome by using mesoporous molecular sieves.

2.5.2 Preparation of Mesoporous Molecular sieves (Sol-Gel method)

Mesoporous molecular sieves are prepared in the laboratory by sol-gel method. The process of sol-gel involves polymerising silica around surfactant self-assembly. Surfactant molecules assemble themselves to constitute the overall structure and morphology of mesoporous materials; hence, they are often called structure-directing agents (SDA) or templates.

"*A template is defined according to its functional role as a structure (usually organic) around which a material (typically inorganic) nucleates and grows in a skin-tight fashion so that upon removal of the template, its geometric and electronic characteristics are replicated in the inorganic material* (Pal and Bhaumik 2013).

Amphiphilic surfactants consist of two parts, hydrophilic part and hydrophobic part. Both parts behave distinctly in polar and non-polar solvents. In a polar medium, such as water, the hydrophilic component is attracted towards the water while the hydrophobic part tends to orientate itself away from water.

Figure 2.2 Micelle formation
(https://blog.biotek.com/2012/10/determination-of-critical-micelle.html)

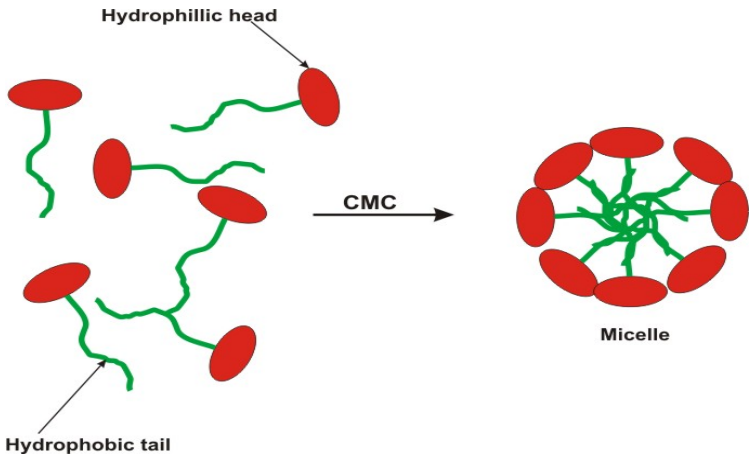

Surfactants molecules thus arrange themselves in the forms of clusters with hydrophobic parts inside and hydrophilic components outside. These clusters are called micelles. The minimum concentration at which surfactant micelles start to form is called critical micellar concentration or CMC. CMC is unique to each surfactant. Above CMC the self-assembly of micelles further grow and form 3D spherical or 2D rod-like structures. These rod-like structures continue to arrange themselves into a hexagonal 3D formation; as shown in Figure 2.2. An inorganic precursor polymerises around the SDA (structure-directing agent or template) self-assembly once it is formed. After the polymerisation of the inorganic precursor, the SDA can either be removed by calcination or by washing in various solvents. The porous network replicated by the SDA inside the siliceous material is used as a catalyst itself or as catalyst support. Mesoporous materials like SBA-15 and MCM-41 are synthesised using this technique. Figure 2.3 shows two pathways for the formation of the final material. In cooperative self-assembly, the precursor starts polymerising simultaneously, as the SDA self-assembly is formed. The liquid crystal thus formed is not a pure liquid crystal. In the true liquid crystal templating, the concentration of surfactant is so high that pure liquid crystals (liquid-crystalline phase) are formed without any intervention of the silica precursor.

Figure 2.3 Mesoporous structures formation
(a) Cooperative self-assembly (b) True Liquid Crystal Templating
(Li and Zhao 2013)

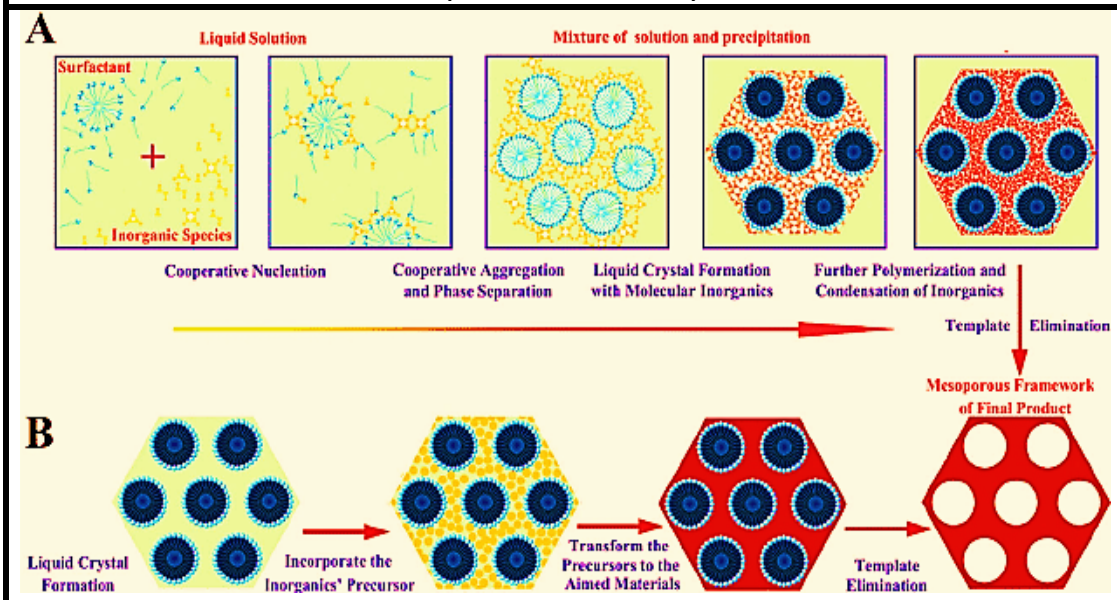

The chemistry of sol-gel preparation is broadly explained as the combination of two chemical reactions, partial hydrolysis of tetra-functional alkoxide (usually tetraethyl orthosilicate) followed by the condensation resulting in the formation of a three-dimensional polymeric network which makes the gel as shown in equations 15, 16 and 17. A mineral acid or a base normally catalyse the hydrolysis. Typical examples of the bases used as catalysts are NH_3, NaOH, NH_4OH and in some cases, KOH has also been used; HCl and in some instances HF have also been used as an acid to catalyse the reaction (Brinker and Scherer, 1989).

Hydrolysis:

$$Si(OC_2H_5)_4 + H_2O \rightleftharpoons Si(OC_2H_5)_3OH + C_2H_5OH \quad \text{(Eq.15)}$$

Condensation:

$$Si(OC_2H_5)_3OH + Si(OC_2H_5)OH \rightleftharpoons (C_2H_5)_3Si - O - Si(C_2H_5)_3 + H_2O \quad \text{(Eq.16)}$$

$$Si(OC_2H_5)_3OH + (C_2H_5O)Si(OC_2H_5)_3 \rightleftharpoons (C_2H_5)_3Si - O - Si(C_2H_5)_3 + C_2H_5OH \quad \text{(Eq.17)}$$

The chemical reaction starts with the hydrolysis of TEOS (tetraethyl orthosilicate), which involves the replacement of the OR group with the OH group (Eq. 15). After hydrolysis, the partial condensation occurs in which siloxane bonds (Si-O-Si) are formed (Eq.16 & 17). Generally, the condensation starts before the hydrolysis is complete. Solvent, pH, catalysts and Si: H_2O ratios play a vital role in the formation of the products. The condensation reaction once started, continues to build larger and larger polymeric molecules by the process of polymerisation. These polymeric molecules cross-link to form a three-dimensional network. By introducing assemblies of surfactant molecules, porosity can be generated in these three-dimensional structures.

2.5.3 Selection of Precursor and SDA (Structure Directing Agent)

Beck *et al*. (1992) presented the earliest work on MCM-41 synthesis. They investigated the use of various surfactant chain lengths ranging from C_4 to C_{16} and different silica precursors from colloidal silica to tetraethyl orthosilicate (TEOS) to study the wall properties. They also used the swelling agents like mesitylene to enlarge the surfactant micelles, which in turn could increase the pore size of the final material. There are several MCM-41 syntheses available in the literature; however, only the recipes which are directly related to this research are taken into account.

Most researchers have used tetraethyl orthosilicate and sodium silicate as silica precursors. Tetraethyl orthosilicate is an expensive ingredient which increases the cost for large scale industrial production. Sodium silicate is commercially manufactured from quartz sand and sodium carbonate at 1300^0C, which consumes a large amount of energy. These drawbacks suggest that the conventional method of producing mesoporous materials is energy-intensive and

expensive. Therefore, some other routes are required for the large scale commercial production of the silica precursor.

Liou (2011) utilised electronic packaging resin waste as a silica source for the synthesis of mesoporous materials like MCM-41. Their synthesis involved alkali extraction of silica from the resin ash and then converting it into mesoporous material using cetyltrimethylammonium bromide as a surfactant. Electronic packaging resin waste contains a high proportion of silicon (approximately 80 weights %) converting this waste into mesoporous materials like MCM-41 makes it an economically viable source for large scale commercial production at relatively low temperature. MCM-41 produced with the above method contained metallic impurities like Sb, Fe, Al, and Cr. It was observed that the total contents of impurities decreased under highly acidic and highly basic conditions. The silica obtained at pH 5 had the highest amount of impurities, i.e. metal contents. They also studied the effect of hydrothermal temperature and the effect of gelation pH on the quality of MCM-41. The presence of a considerable amount of metallic impurities makes this route less attractive in this research because the presence of metal impurities can cause the MCM-41 structure to collapse during calcination (Pal and Bhaumik, 2013; Brinker and Scherer,1989). Silicon alkoxide (as TEOS) is therefore preferred over sodium silicate.

Cai *et al.* (1999) synthesised highly ordered MCM-41 using extremely low surfactant concentration (0.5-0.1 wt %) using, TEOS, cetyltrimethylammonium bromide (CTAB), distilled water, NH_4OH at room temperature. The author has also prepared samples using NaOH instead of NH_4OH. The characteristics of the samples prepared using each base were similar. The degree of order (based on XRD reflection peaks) of the MCM-41 prepared by each base was identical. The

template was removed by calcination in air at 550^0C. The main advantages of this process are a low amount of surfactant, synthesis at room temperature, which makes the process kinetically controlled unlike most of the preparations reported in the literature which are thermodynamically controlled.

In this research, Cai *et al.* (1999) recipe have been adopted for MCM-41 synthesis. NH_4OH is used as a base instead of NaOH due to the concern raised by Pal and Bhaumik (2013) and Brinker and Scherer (1989) about the Na atom, causing the structural damage to MCM-41. The complete recipe is described in Chapter 4.

References:

Aresta, M., Dibenedetto, A. and Quaranta, E. (2016) 'State of the art and perspectives in catalytic processes for CO_2 conversion into chemicals and fuels: The distinctive contribution of chemical catalysis and biotechnology', *Journal of catalysis*, 343, pp. 2.

Beck, J.S., Vartuli, J.S., Roth, W.J., Leonwicz, M. E., Kresge, C.T., Schmitt, K.D., Chu, C.T.W., Olson, D.H., Sheppard, E.W. (1992) ' A new family of mesoporous molecular sieves prepared with liquid crystal templates', *Journal of the American chemical society*, 114(27), pp. 10834.

Brinker, C.J. and Scherer, G.W. (1989) 'Hydrolysis and condensation: Silicates', *Sol-Gel Science*, New York: Academic Press, INC an imprint of Elsevier Science, pp. 97.

Devdutt, C. (2012) ' Perspectives on the synthesis of organic carbamates', *Tetrahedron*, 68(1-7), pp. 15.

Cai, Q., Lin, W.Y., Xiao, F.S., Pang, W,Q., Chen, X.H., Zou, B.S. (1999) 'The preparation of highly ordered MCM-41 with extremely low surfactant concentration', *Microporous and Mesoporous Materials*, 32(1-2), pp. 1.

Griffin, K.L. and Seemann, J.R. (1996) 'Plants, CO_2 and photosynthesis in the 21st century', *Chemistry and Biology*, 3(4), pp. 245.

Halmann, M.M. & Steinberg, M. (1999) 'Greenhouse gas carbon dioxide mitigation: Science and Technology', *Journal of American Chemical Society*, 123(29), pp. 7197.

Huang, K, Sun, C.L. and Shi, Z.J. (2010) ' Transition-metal-catalysed C-C bond formation through the fixation of carbon dioxide', *The Royal Society of Chemistry*, 40(5), pp. 2435.

Inui, T. (1996). 'Highly effective conversion of carbon dioxide to valuable compounds on composite catalysts', *Catalysis Today*, 29(1-4), pp. 329.

Lee, S., Ju, H.K., Machunda, R., Uhm, S., Lee, J.K., Lee, H.J. and Lee. J. (2015) 'Sustainable production of formic acid by electrolytic reduction of gaseous carbon dioxide', *Journal of Material Chemistry A*, 3, pp. 3029.

Li, J., Qi, X, Wang, L., He, Y. and Deng, Y. (2011) 'New attempt for CO_2 utilization: One-pot catalytic syntheses of methyl, ethyl and n-butyl carbamates', *Catalysis Communications*, 12(13), pp. 1224.

Liou, T.H. (2011) 'A green route to the preparation of MCM-41 silicas with well-ordered mesostructure controlled in acidic and alkaline environments', *Chemical Engineering Journal*, 171(3), pp. 1458.

Li, Wei & Zhao, Dongyuan. (2013) 'An overview of the synthesis of ordered mesoporous materials', *Chemical Communications*, 49(10), pp. 943.

Moon D J. (2005) 'Development of tri-reforming catalyst for utilization of CO_2 in SOFC and MCFC fuel reforming applications', *Proceedings of the 8th International Conference on Carbon Dioxide Utilization*, Oslo, Norway, 22-26 June.

Omae, I. (2006) 'Aspects of carbon dioxide utilization', *Catalysis Today*, 115(1-4), pp. 33.

Pal, N. and Bhaumik, A. (2013) 'Soft templating strategies for the synthesis of mesoporous materials: Inorganic, organic-inorganic hybrid and purely organic solids', *Advances in Colloid and Interface Science*, 189, pp. 21.

Rezaei, M., Alavi, S.M., Sahebdelfar, S. and Yan, Z.F. (2006) 'Syngas production by methane reforming with carbon dioxide on noble metal catalysts' *Journal of Natural Gas Chemistry*, 15(4), pp. 327.

Song, C.S. (2001) ‘Tri-reforming: A New Process for Reducing CO_2 Emissions’, *Chemical Innovation (formerly Chemtech, ACS)*, 31(1), pp. 21.

Song, C.S. (2002) ‘CO_2 Conversion and utilization: an overview’, *Energy and Fuels*, 16(5), pp. 1329.

Song, C.S., Pan, W., Srimat, S.T., Zheng, J., Li, Y. Wang, Y.H., Xu, B.Q., and Zhu, Q.M. (2004)’ Tri-reforming of Methane over Ni Catalysts for CO_2 Conversion to Syngas With Desired H_2/CO Ratios Using Flue Gas of Power Plants Without CO_2 Separation’, *Studies in Surface Science Catalysis*, 153, pp. 315.

Song, C.S. and Pan, W. (2004) ‘Tri-reforming of methane: a novel concept for catalytic production of industrially useful synthesis gas with desired H_2/CO ratios’, *Catalysis Today*, 98(4), pp.463.

Srivastava, R., Manju, M.D. and Ratnasamy, P., (2004) ‘ Phosgene-free synthesis of carbamates over zeolite-based catalysts’, *Catalysis Letters*, 97(1-2), pp. 41.

Srivastava, R., Srinivas, D. and Ratnasamy, P. (2005) ‘CO_2 activation and synthesis of cyclic carbonates and alkyl/aryl carbamates over adenine-modified Ti-SBA-15 solid catalysts’, *Journal of Catalysis*, 133(1), pp. 1.

Srivastava, R., Srinivas, D. and Ratnasamy, P. (2005) ‘Zeolite-based organic-inorganic hybrid catalysts for phosgene-free and solvent-free synthesis of cyclic carbonates and carbamates at mild conditions utilizing CO_2’, *Applied Catalysis A: General*, 289(2), pp. 128.

Srivastava, R., Srinivas, D. and Ratnasamy, P. (2006) ‘Syntheses of polycarbonate and polyurethane precursors utilizing CO_2 over highly efficient, solid as-synthesized MCM-41 catalyst’, *Tetrahedron Letters*, 47(25), pp. 4213.

Zangeneh, F.T., Sahebdelfar, S. and Ravanchi, M.T. (2011) ‘Conversion of carbon dioxide to valuable petrochemicals: An approach to clean development mechanism’, *Journal of Natural Gas Chemistry*, 20(3), pp. 219-231.

Chapter 3

MCM-41 Synthesis and Characterisation

3.1 Synthesis

MCM-41 samples in this research work have been prepared by the sol-gel method using the synthesis procedure of Cai *et al.* (1999).

3.1.1 Materials and Chemicals

- CTAB (cetyltrimethylammonium bromide) obtained from Sigma Aldrich ≥ 98%
- TEOS (tetraethyl orthosilicate) obtained from Sigma Aldrich 98%
- NH_4OH 35% obtained from Fischer Scientific
- Tetraalkylammonium bromide salts obtained Sigma Aldrich 99%

3.2 Characterization

3.2.1 X-Ray Diffraction

The XRD equipment used was a Siemens D500 diffractometer of Bragg Brentano geometry, using nickel-filtered Cu-Kα radiation of wavelength λ = 0.15406 nm. The equipment was operated at a tube voltage of 40 kV and 20 mA current. Low angle XRD experiments were performed between 2θ ranges of 1^0 – 10^0 at a scanning rate of 1°/min with a step size of 0.01 degrees. The step size of 0.01 degrees was used; therefore, the full width at half maximum (FWHM) occurred with high precision. The calculated values of d_{100} and a_0 were accurate to 0.0001 nm. The interplanar distance (d_{100}) is defined as the distance between the sets of

parallel planes formed by the individual cells in a lattice structure. The interplanar distance (d_{100}) depends on the radii of the atoms forming the structure. The cell parameter a_0 is the distance between the centres of two consecutive pores. The inter-planer distance d_{100} and the cell parameter a_0 were calculated using Bragg's law as follows:

$n\lambda$ = $2d\text{Sin}(\theta)$ or $d = \frac{n\lambda}{2Sin\theta}$

$a_0 = 2\sqrt{3}d$

3.2.2 Scanning Electron Microscopy (SEM)

The setup used for SEM was a Hitachi S-3400N scanning electron microscope operated at an accelerating voltage in the 15 – 20 kV range. Gold-coated MCM-41 samples were mounted on an adhesive carbon film pasted on an aluminium alloy stub located inside the scanning electron microscope.

3.2.3 Energy Dispersive X-Ray Spectroscopy (EDX)

SEM apparatus used above was used for the elemental analysis of the MCM-41 samples before gold sputtering.

3.2.4 Transmission Electron Microscopy (TEM)

TEM scanning was performed at Department of physics, Durham University. MCM-41 powder was homogeneously dispersed in IPA (*Isopropyl alcohol*) using ultrasonic bath before depositing on a holey carbon grid. Samples were examined in a JEOL 2100F FEG TEM at 80 kV. Images were acquired on a Gatan Orius CCD camera.

3.2.5 Nitrogen physisorption analysis

Nitrogen physisorption data was acquired on a Quantachrome Autosorb iQ Model 6 equipment. The degassing of the MCM-41 was carried out at 300^0C for 3 hours. The physisorption experiments were performed using liquid nitrogen at -196.15^0C (77K).

3.3 Synthesis of MCM-41

176 ml NH_4OH was mixed with 200 ml of de-ionised water at 35^0C. 2 g of cetyltrimethylammonium bromide was dissolved until a clear solution was observed. 10 ml of tetraethyl orthosilicate was added to this solution. The solution remained under vigorous stirring before and after the TEOS addition. A white slurry was observed after a few minutes which was allowed to age for 2 hours under the same conditions.

The synthesis was carried out at 35^0C because cetyltrimethylammonium bromide forms micelles above 30^0C. A few attempts were made to carry out the synthesis at room temperature, but the surfactant did not wholly dissolve even after two hours of vigorous stirring. The sample prepared at 35^0C used as a standard sample was prepared only once and compared with all the other samples prepared at different conditions.

Post-synthesis Treatment: The gel was filtered and washed three times with de-ionised water, followed by drying in air at room temperature for 24 hours. The dried as-synthesised MCM-41 thus prepared was calcined at 550^0C for 6 hours at the rate of 1^0C/minute to remove the template.

Cai *et al.* (1999) have claimed that the method is capable of custom tuning MCM-41 with a very high degree of order within nanometre-scale periodicity and micrometre scale defined morphology. Several MCM-41 samples were

synthesised by varying temperature, pH, ageing time and amount of water to understand the effect of these factors on the long-range order of MCM-41. The samples were characterised using powder X-Ray diffraction, scanning electron microscopy and energy-dispersive X-ray spectroscopy (EDX) to establish the basis for an improved recipe to prepare samples with characteristics of long-range order, improved stability, narrow pore-size distribution, and larger pore diameter.

3.4 Effect of temperature variations on MCM-41 synthesis and characterisation

3.4.1 Temperature variation pH not maintained

Three MCM-41 samples were prepared at 35^0C, 65^0C, 70^0C and 80^0C. The temperatures intended for studying the effect of temperature on MCM-41 synthesis were 60^0C, 70^0C and 80^0C. However, due to the instrument problem temperature of 60^0C could not be maintained; therefore, the sample was prepared at 65^0C instead. Brinker and Scherer (1989) suggested that the quality of MCM-41 starts to deteriorate above 80^0C. Therefore no synthesis was done above 80^0C. The samples were labelled as “MCM-41” followed by the synthesis temperature, as shown below:

MCM-41-T ^{0}C

Where, T= 35^0C, 65^0C, 70^0C and 80^0C

The pH measured at the end of the experiments was 11.8. During these syntheses, the gel pH was not controlled. However, the ample amount of NH_4OH kept the solution pH above 11 throughout the synthesis.

3.4.2 Temperature variation pH maintained

Numerous experiments were performed under strictly maintained pH to study the effect of pH on MCM-41 synthesis. The experiments performed below pH 7 did not lead to the formation of gel at all; the experiments carried out between pH 7 to 10 formed hard crystalline materials which did not withstand the high calcination temperature. Only the samples prepared between pH 11- 11.2 produced highly ordered MCM-41. The samples prepared at pH above 11.8 showed a decline in the degree of order of MCM-41. The above observations showed that the pH had played a crucial role in the chemistry of sol-gel synthesis. Therefore, five samples were prepared at pH 11 at 35^0C, 65^0 C, 70^0 C, and 80^0C to investigate the relationship between temperature and pH further. The samples were labelled as follows:

MCM-41-T^{0}C pH

"T" =35^0C, 65^0 C, 70^0 C, and 80^0C and "pH" denotes the pH was maintained during the synthesis. The pH was maintained by the addition of NH_4OH before and after the addition of TEOS (pH falls drastically after the addition of TEOS).

3.4.3 Results

3.4.3.1 X-Ray Diffraction

Temperature variation pH not maintained

Powder X-ray diffraction analysis confirmed the presence of the characteristic hexagonal structure of MCM-41. The Inter-planar distance d_{100} and the cell parameter a_0 were calculated using Bragg's Law. XRD scans in Figure 3.1 confirm the presence of four distinct XRD reflection peaks for (100), (110), (200) and (210) planes confirming the unique fingerprint of highly ordered hexagonal MCM-41 structure.

Figure 3.1 XRD comparison temperature variation pH not maintained

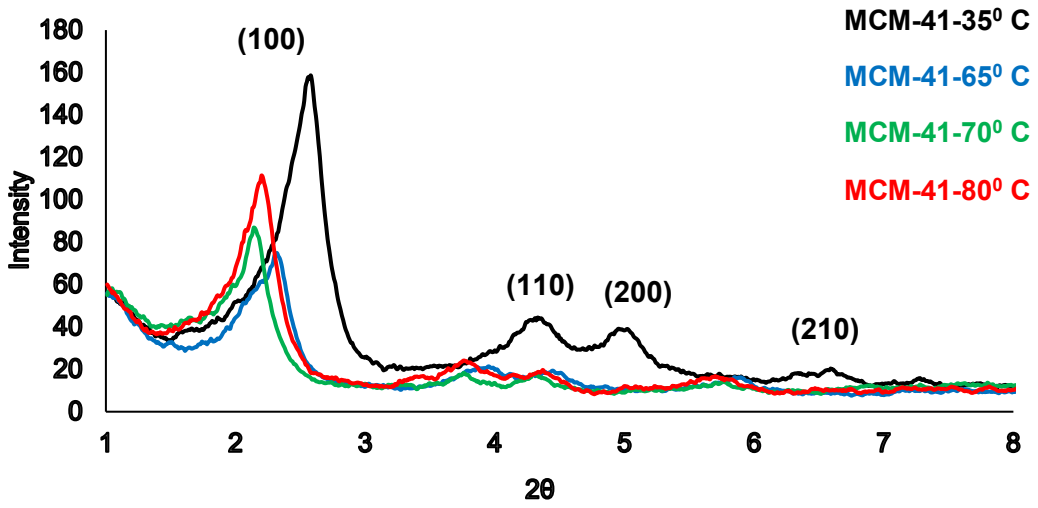

Sample MCM-41-65^{0}C deviated from the trend followed by other samples in the temperature variation. Therefore, this sample was disregarded for comparison. The nitrogen physisorption experiments described on page 54 show that this sample exhibits a unique pore network structure which cannot be compared to other samples. Therefore, ignoring MCM-41-65^{0}C, the cell parameter a_0 and interplanar distance d_{100} increased with increasing the synthesis temperature from 35^{0}C to 80^{0}C, as shown in Table 3.1. The highly intense (100) plane XRD reflections at high temperatures mean the long-range order in MCM-41 samples was improved with increasing temperature. The steady increase in the values of a_0 and d_{100} indicated that increasing the synthesis temperature had caused MCM-41 unit cell expansion.

Table 3.1 Effect of temperature on the structure of MCM-41					
Sample Identification	**Temperature ^{0}C**	**d_{100} (nm)**		**a_0 (nm)**	
		pH not maintained	pH maintained	pH not maintained	pH maintained
MCM-41-35^0 C	35	3.4	3.9	4.0	4.4
MCM-41-65^0 C	65	3.7	3.7	4.3	4.3
MCM-41-70^0 C	70	3.6	3.6	4.1	4.1
MCM-41-80^0 C	80	3.7	4.0	4.3	4.7

Temperature variation pH maintained

A pH value of 11 was maintained before and after the TEOS addition. It was observed that the pH of the solution drastically decreased after the TEOS addition. High pH fluctuations were observed in the first five minutes of the TEOS addition. To avoid the pH fluctuations, NH_4OH was continuously added after the TEOS addition to maintain the pH between 11 and 11.3. Figure 3.2 shows the comparison of XRD scans of samples prepared at gel pH maintained between 11 and 11.3. Based on the intensity of the XRD reflection peaks for (100) plane, the optimum temperature for MCM-41 synthesis was 70^{0}C, after which the long-range order started to decline. The reflection of (100) plane of MCM-41-80^{0}C pH was less intense than the rest of the samples (excluding MCM-41-65^{0}C pH). MCM-41-65^{0}C again showed a unique behaviour in pH maintained syntheses.

Figure 3.2 XRD comparison temperature variation pH maintained

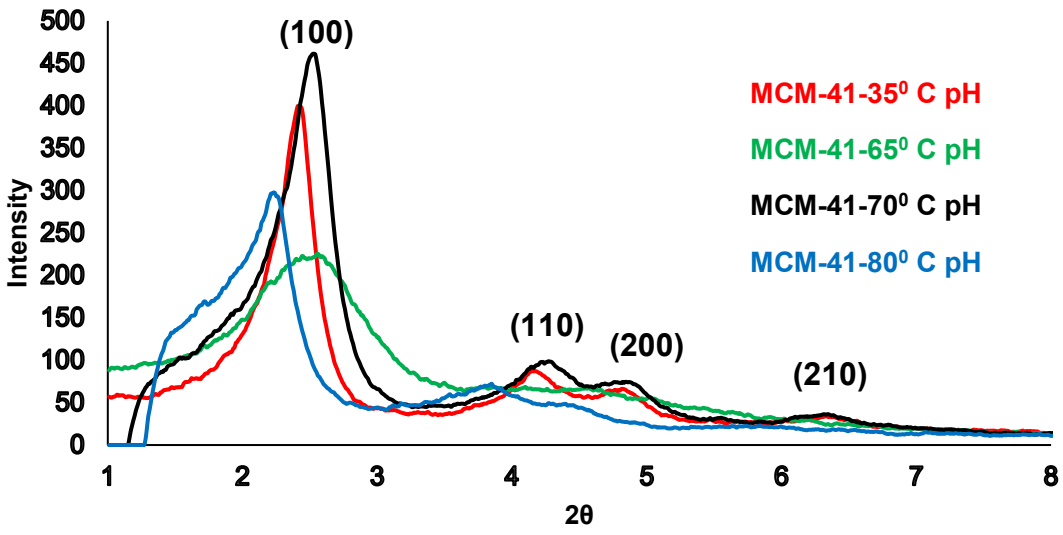

It is important to note that the XRD reflection peak for (100) plane shifted more towards the left for MCM-41-80^{0}C pH, which shows an expansion in the unit cell size at 80^{0}C. Figure 3.3 shows the XRD reflection peaks for the MCM-41 samples prepared at maintained pH exhibited narrower, and higher XRD reflection peaks than those of the corresponding MCM-41 samples synthesised at the same temperature without maintaining the pH. The sample MCM-41-65^0 C pH has shown different behaviour than the rest of the samples in both cases. When the pH was maintained at 65^{0}C, the XRD reflection peak for (100) plane became broader, as shown in Figure 3.3 (d). The characteristic XRD reflection peak of MCM-41-65^0 C pH is also not as sharp as those of MCM-41-70^0 C pH and MCM-41-80^0 C pH.

Figure 3.3 XRD comparison of samples prepared at maintained pH versus pH not maintained

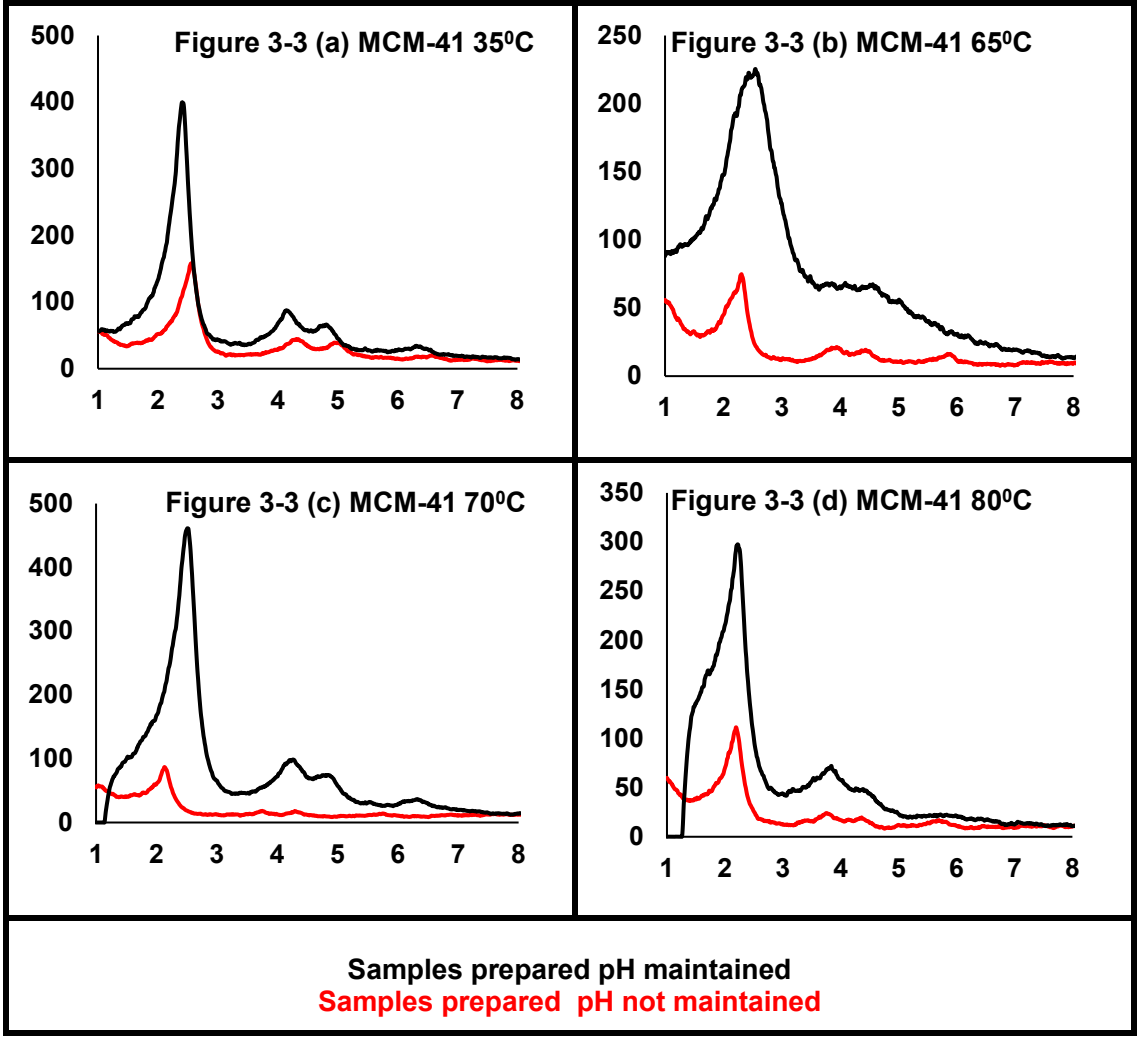

Table 3.1 (Page 50) shows that under controlled pH condition, the values of a_0 and d_{100} increased significantly for MCM-41-35^{0}C pH as compared to MCM-41-35^{0}C (pH not maintained). The interplanar distance d_{100} and the cell parameter a_0 did not change regardless of the pH conditions at 70^{0}C. The values of d_{100} and a_0 increased with maintaining the pH at 80^{0}C. Figure 3.3 shows that the (100) plane XRD reflection peak of MCM-41-70^{0}C pH is more intense than that of MCM-41-70^{0}C. However, in the case of MCM-41-65^{0}C pH, the (100) reflection became broader than the (100) reflection for MCM-41-65^{0}C, which shows that the MCM-41-65^{0}C pH suffered a loss in the long-range order due to pH control.

The XRD reflection peaks for MCM-41-70^{0}C pH maintained did not show a shift in the position of the (100) plane XRD reflection from that of MCM-41-70^{0}C. Therefore the pH control did not affect the size of the MCM-41-70^{0}C unit cell (the values of a_0 and d_{100} did not change at &70^{0}C regardless of pH conditions). The XRD reflection peaks for all the samples prepared at a maintained pH are significantly higher than the corresponding peaks of the samples prepared without maintaining pH, showing an improvement in the long-range order due to pH control. An expansion in the unit cell size was observed when the pH was maintained at 80^{0}C (Table 3.1); however, the XRD scans of MCM-41-80^0 C pH in Figure 3.2 had shown a decrease in the intensity of XRD reflection peaks. Increase in the unit cell size, along with a decrease in the long-range order (lower XRD peak intensity) represents the dissolution of pore walls due to silica hydrolysis at high temperature (Brinker and Scherer, 1989). It is necessary to mention here that it was challenging to maintain the pH at 70^{0}C and 80^{0}C. The pH value dropped abruptly at 80^{0}C; therefore, a large amount of NH_4OH was added to keep the pH constant. The large amount of NH_4OH at higher temperature causes the dissolution of pore walls (silica hydrolysis) resulting in a decline in the long-range order of MCM-41 structure (along with a pretence of unit cell expansion). The sample MCM-41-80^0 C (pH not maintained), showed better (100) reflection than the MCM-41-70^{0}C (pH not maintained).

On the other hand, MCM-41-80^{0}C pH exhibited less number of XRD reflection peaks to MCM-41-80^0 C (pH not maintained) and MCM-41-70^{0}C pH. A lesser number of XRD reflection peaks represent an inferior degree of long-range order to a low intensity (100) plane reflection peak with more number of peaks This temperature dependence of pH shows that although increasing the

pH was beneficial; it worked counterproductive after an optimum temperature which in this case, is 70^0C. Figure 3.4 shows a comparison between scanning electron micrographs of MCM-41 samples at different temperature.

Figure 3.4 SEM image of samples prepared without maintaining pH

Figure 3.4(a)
MCM-41-35^0C
20.0KV 6.6mm x20.0K SE 2.00µm

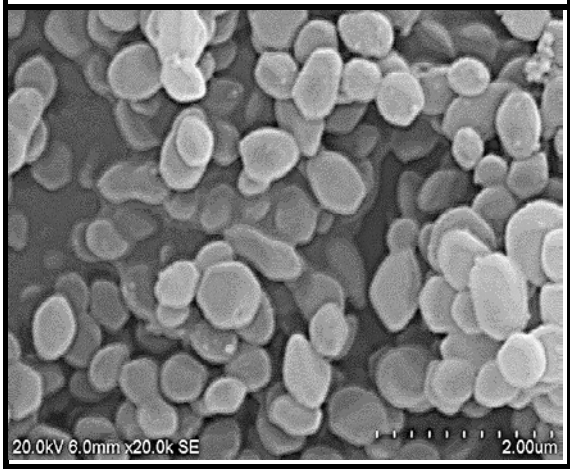

Figure 3.4(b)
MCM-41-65^0C
20.0KV 6.6mm x20.0K SE 2.00µm

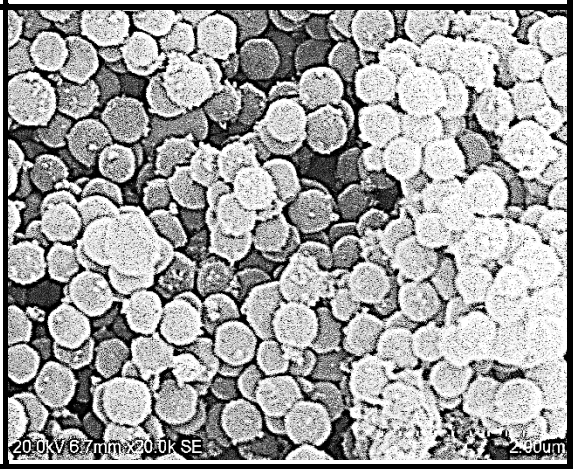

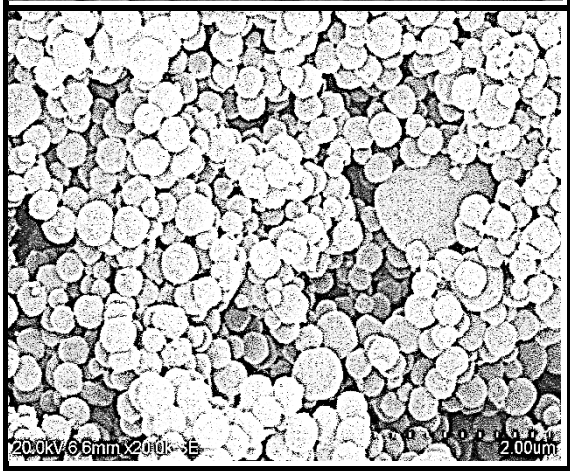

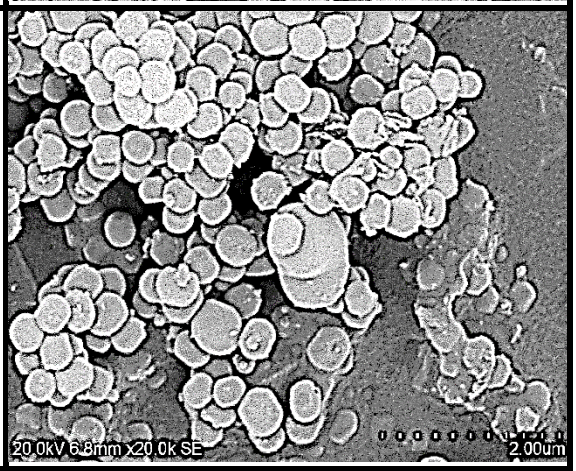

Figure 3.4(c)
MCM-41-70^0C
20.0KV 6.6mm x20.0K SE 2.00µm

Figure 3.4(d)
MCM-41-80^0C
20.0KV 6.6mm x20.0K SE 2.00µm

3.4.3.2 Nitrogen adsorption-desorption isotherms

Nitrogen physisorption analysis was done for the samples prepared at a maintained pH at 35^0C, 65^0C, 70^0C and 80^0C. N_2 physisorption results in Table 3.2 show that the sample MCM-41-65^0C pH exhibited the highest surface area. However, sample MCM-41-65^0C pH should again be disregarded for comparison

until the adsorption and desorption behaviour of this sample is fully understood in Figures 3.5 and Figure 3.6. The surface area of MCM-41 decreased with increasing the synthesis temperature from 35^0C to 70^0C (ignoring MCM-41-65^0CpH).

Table 3.2 Nitrogen physisorption analysis

Sample ID	Specific surface Area	Average pore diameter	Pore volume	Cell parameter	Pore wall thickness
	S_g	d_{Pore}	v_{Pore}	a_0	$t = (d_{Pore} - a_0)$
	m^2g^{-1}	nm	cm^3g^{-1}	nm	nm
MCM-41-30^0CpH	1640	2.5	1.2	4.4	1.9
MCM-41-65^0CpH	1857	2.7	1.6	4.3	1.6
MCM-41-70^0pH	1395	2.6	1.8	4.1	1.5
MCM-41-80^0 pH	1433	2.7	1.2	4.7	2

The average pore diameter, however slightly increased from 2.5 nm for 35^0C to 2.6 nm for 70^0C and 80^0C. The odd behaviour of MCM-41-65^0C can be understood by analysing the hysteresis loop and the pore size distribution shown in Figure 3.5 and Figure 3.6 . The hysteresis loop of MCM-41-65^0CpH is a combination of two types of hysteresis H1 and H2 (b) which show the material has a wide range of pore size distributions.

Figure 3.5 Hysteresis loop MCM-41-65^0C pH

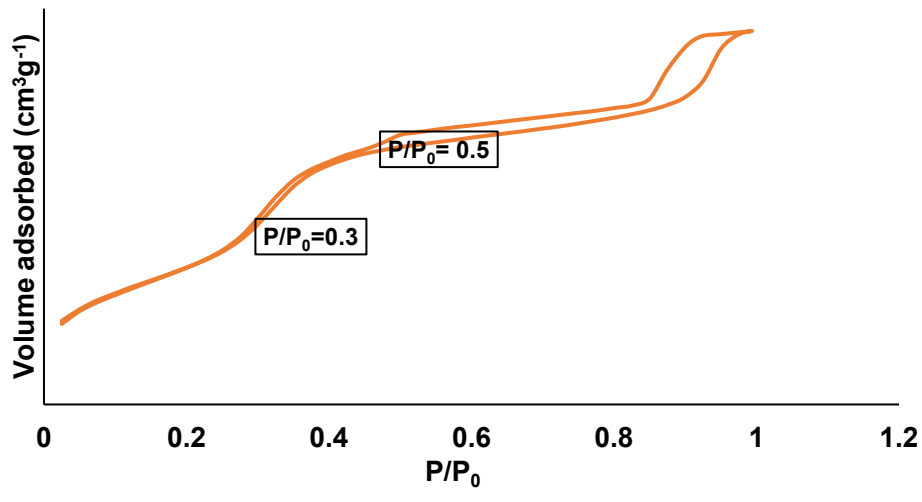

Figure 3.6 Pore size distribution of MCM-41-65^{0}C pH

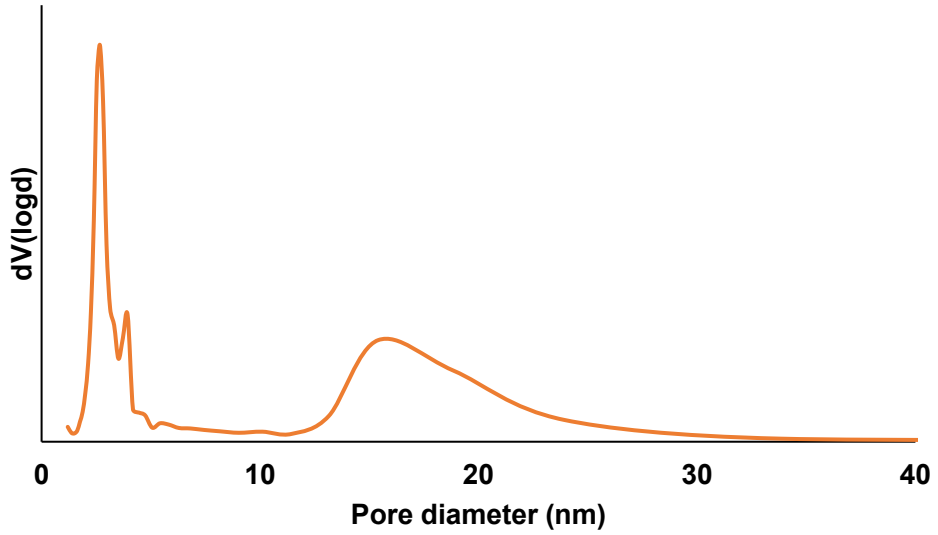

The H1 part of the hysteresis between P/P_0 = 0.3-0.5 represents mesopores with uniform connectivity. The H2 (b) type hysteresis at high values of P/P_0 = 0.8 show the pore-blocking effect, due to the presence of a pore size distribution of pores having neck widths much larger than those of the pores on the H1 part of the hysteresis. The pore size distribution of pore diameters ranging between 13 nm to 25 nm in Figure 3.6 represents the H2 part of the hysteresis. The sample MCM-41-80^{0}C pH has shown a hysteresis loop identical to the sample MCM-41-100^{0}C Post-calcination, which will be discussed in Chapter 5. The adsorption branch on the isotherm of MCM-41-80^{0}C pH showed a steady increase in adsorption occurring between P/P_0 = 0.5.-0.9 due to pores having larger dimensions than the pores at P/P_0 < 0.5, as shown in Figure 3.7.

Figure 3.7 Hysteresis loop MCM-41-80^{0}C pH

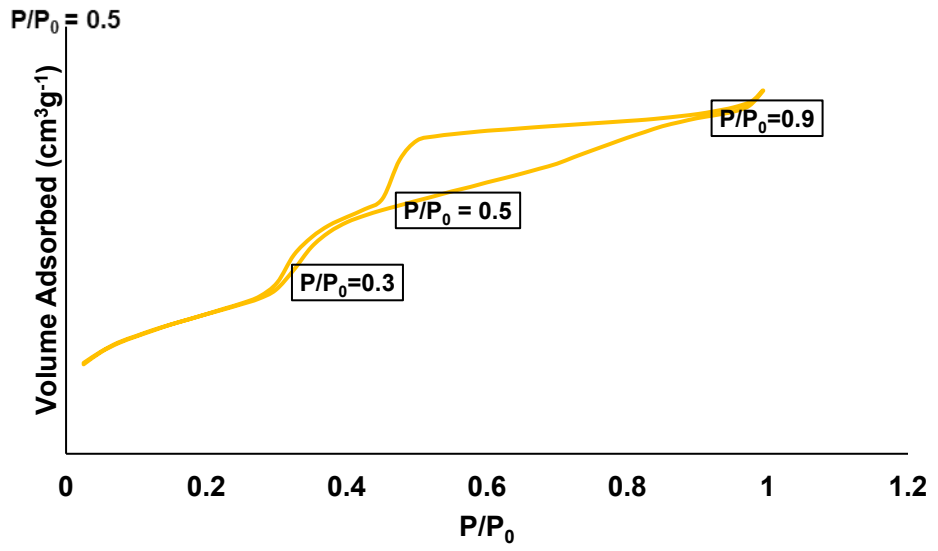

The triangular hysteresis in Figure 3.7 occurred due to the slow desorption that happened between P/P_0 =1 and P/P_0 = 0.5, followed by rapid desorption below P/P_0 =0.5. This behaviour was due to the pore- blocking in a narrow range of pore necks or cavitation induced evaporation. The adsorption-desorption paths and the triangular hysteresis also suggested that the sample MCM-41-80^{0}C pH had two distinct pore size distributions which lead to pore connectivity problems (pore-blocking) causing restricted adsorption above P/P_0= 0.5 and delayed capillary evaporation causing a triangular hysteresis. Figure 3.8 confirms the presence of the bimodal pore size distribution with the smaller range peak value of 2.7 nm and the larger peak pore size of 3.7 nm.

Figure 3.8 Pore size distribution of MCM-41-80^{0}C pH

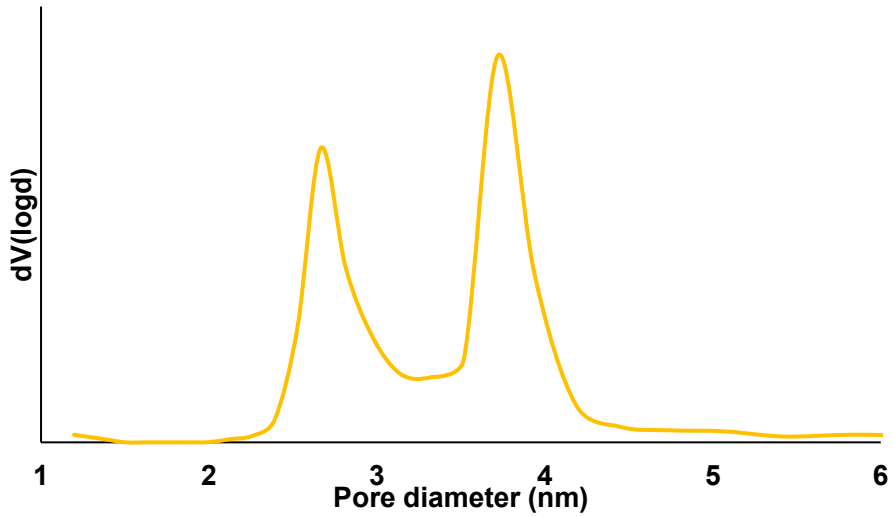

Figure 3.9 shows the comparison of the hysteresis loops of the sample; MCM-41 35^{0}C and MCM-41-70^{0}C.

Figure 3.9 Hysteresis loops MCM-41-35^{0}C pH and MCM-41 70^{0}CpH

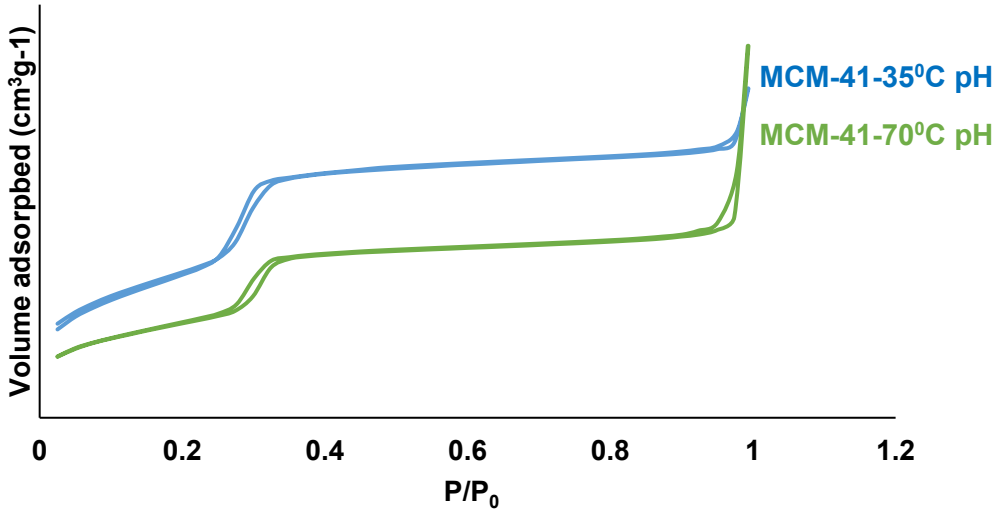

It is evident from the figure that both samples showed very narrow hysteresis loops of type H1 on type IV isotherms; hence, the samples had highly uniform cylindrical pores with facile pore connectivity.

Figure 3.10 Pore size distributions of samples MCM-41-35^{0}C pH

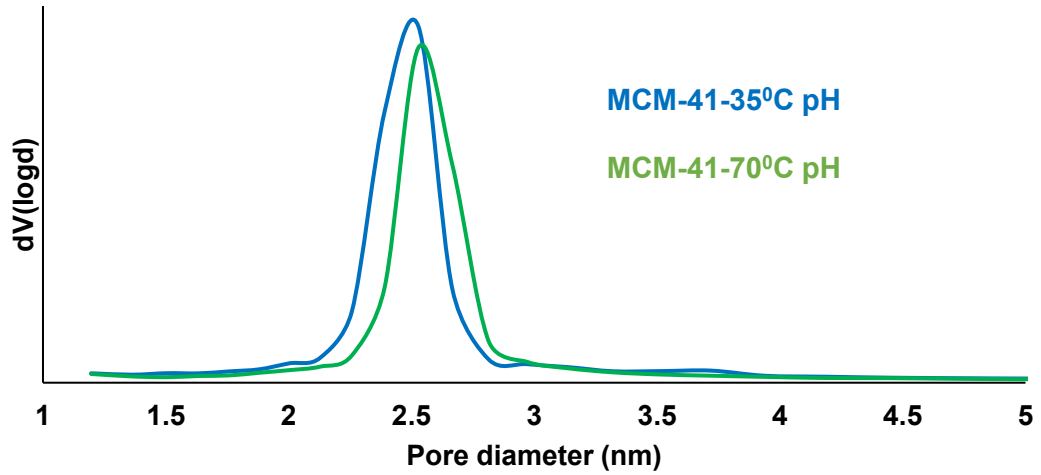

The pore size distributions for the samples MCM-41-35^{0}C and MCM-41-70^{0}C shown in Figure 3.10 confirm that both the samples possessed very narrow pore size distributions.

3.4.3.3 Discussion

Effect of temperature variation on MCM-41 characterisation

The long-range order in the MCM-41 structure improved with increasing the synthesis temperature and controlling the pH; however, it started to decline at 80^{0}C. Literature also confirms that synthesising MCM-41 above 80^{0}C causes a sharp decline in the quality of MCM-41. At high temperatures, such as above 80^{0}C, the pH of the synthesis gel decreases abruptly due to rapid evaporation of NH_4OH. When the pH falls, rapid condensation occurs with a slow rate of hydrolysis, causing a decline in the long-range order of MCM-41 (Brinker, and Scherer (1989). Also adding NH_4OH to increase the pH will result in the

dissolution of the pore walls due to silica hydrolysis. It is interesting to note that the samples MCM-41-65^0 C and MCM-41-65^0 C pH have shown a structural degradation irrespective of the pH control, which shows that at 65^{0}C the role of temperature was more significant in the formation of the long-range order in MCM-41 structure than the role of pH. Controlling pH has improved the long-range order at 35^{0}C and 70^{0}C; however, at 65^0 C (irrespective of the pH control) and 80^{0}C (controlled pH), the long-range order of MCM-41 suffered a decline. EDX results in Table 3.3 show equal wt. % of silicon in samples prepared at 65^{0}C and 80^{0}C. The XRD results of both the samples MCM-41-65^{0}C (pH not maintained) and MCM-41-80^{0}C (pH not maintained) showed inferior XRD peaks than "MCM-41-70^0 C (pH not maintained) which exhibited 7% more silicon than the other two samples. The EDX was done to confirm that all the carbon was removed by calcination. Some of the EDX results in the following sections do not show theoretically consistent results due to the large percentage of carbon present even after calcination.

Table 3.3 EDX results for MCM-41 temperature variation pH not maintained

Sample	Silicon wt. %	Oxygen wt. %
MCM-41-65^0 C	**51**	**49**
MCM-41-70^0 C	**58**	**42**
MCM-41-80^0 C	**51**	**49**

Table 3.1 (Page 50) shows the unit cell expansion with an increase in the synthesis temperature from 35^{0}C to 65^{0}C. The unit cell expansion occurred because at high-temperature water penetrates inside the pores and cause the pore walls to expand; interplanar distance d_{100} and cell parameter a_0, therefore, increases (Khushalani *et al*., 1995 and Kruk *et al.,*1999).

Effect of pH on MCM-41 Characterization

Sajjadi *et al.* (2016) investigated the effects of various factors on the synthesis and characterisation of MCM-41. Describing the effect of NH_4OH/H_2O ratio on MCM-41 characterisation, they concluded that a low concentration of NH_4OH (low pH) inhibited the development of the long-range order in MCM-41. Low pH favours slower hydrolysis and faster condensation, which decreases the degree of long-range order in MCM-41. A high concentration of NH_4OH, therefore, slows down the condensation and enhances the hydrolysis of silica. Higher silica hydrolysis generates more monomers which readily form dimers, trimers and tetramers. These smaller molecules readily join each other or relatively larger molecules (silicates) establishing a highly ordered polysilicate network. The increase in the monomer population prevents the larger silicates or polysilicates from joining together (preventing rapid condensation). The slower condensation rate enhances the formation of desired Si-O-Si (siloxane) bonds over the Si-OH (silanol) bonds, which are the main reason behind the low hydrothermal stability of MCM-41. Alothman (2012) and Brinker and Scherer (1989) have explained the same fact with a slightly different perspective by stating that the solubility and dissolution of silica are high at pH ≥ 7, and the ionization of silica particles ("point of zero charge and isoelectric point" for silica lie between pH 1 and 3) is high enough to cause the particle growth without gelation or aggregation. At pH below 7, the condensation occurs only between more highly condensed particles and less highly condensed particles hence the rate of dimerisation is low, once the dimers are formed they react with monomers to form trimers and tetramers. This “ripening” results in a sharp decline in monomer population resulting in cyclisation which poses a reduced Si-O-Si bond angle, the resulting strain causes the products to be less stable under acidic conditions (pH 2-7).

Hence, pH and temperature are intertwined factors which govern the development of the highly ordered structure of MCM-41.

Explaining the odd behaviour of MCM-41-650C pH

The odd behaviour of MCM-41-65^{0}C pH and MCM-41-65^{0}C can better be explained after considering the nitrogen physisorption results discussed in Section 3.4.3.2 (Page 54). The wider pore size distribution for sample MCM-41-65^{0}C pH shows that the temperature of 65^{0}C was not high enough for comprehensive silica restructuring of MCM-41 to happen. The XRD scan of MCM-41-65^{0}C pH and MCM-41-65^{0}C have also shown a decline in the long-range order, which is in agreement with the broader and uneven pore size distributions at the synthesis temperature of 65^{0}C. At the synthesis temperature of 70^{0}C, under controlled pH, the long-range order was re-established as shown by the comparison of (100) XRD reflection peaks in Figure 3.2 (Page 51). The re-establishment of the long-range order at 70^{0}C shows that the silica restructuring leads to completion at the synthesis temperature of 70^{0}C. At the synthesis temperature of 80^{0}C, under controlled pH, the bi-modal pore size distribution observed in Figure 3.8 (Page 58) represents pore size expansion due to high synthesis temperature. The thicker pore-wall and larger pore diameter of sample MCM-41-80^{0}C show extensive hydrothermal restructuring happening at 80^{0}C. It is interesting to note that a silica restructuring leading to completion has already been inferred for MCM-41-70^{0}C and MCM-41-70^{0}C pH; therefore, the inference of extensive hydrothermal restructuring for MCM-41-80^{0}C seems a contradiction. However, this is not a contradiction the extent of hydrothermal restructuring is different for both the samples. The hydrothermal restructuring is

closely related to the pH and the hydrothermal temperature of the synthesis gel, as discussed in Chapter 5.

3.5 Effect of water on the characterisation of MCM-41

Three samples were prepared using the procedure as described in Section 3.3 (Page 46) except the amount of water used was 20 ml, 50ml and 100 ml. The samples were labelled as follows:

MCM-41-35^{0}C (amount of water in ml)

3.5.1 Results

3.5.1.1 X-Ray Diffraction

Figure 3.11 shows the X-Ray diffraction scans comparison of the MCM-41 samples prepared with varying the amount of water.

Figure 3.11 XRD comparison Si: H_2O

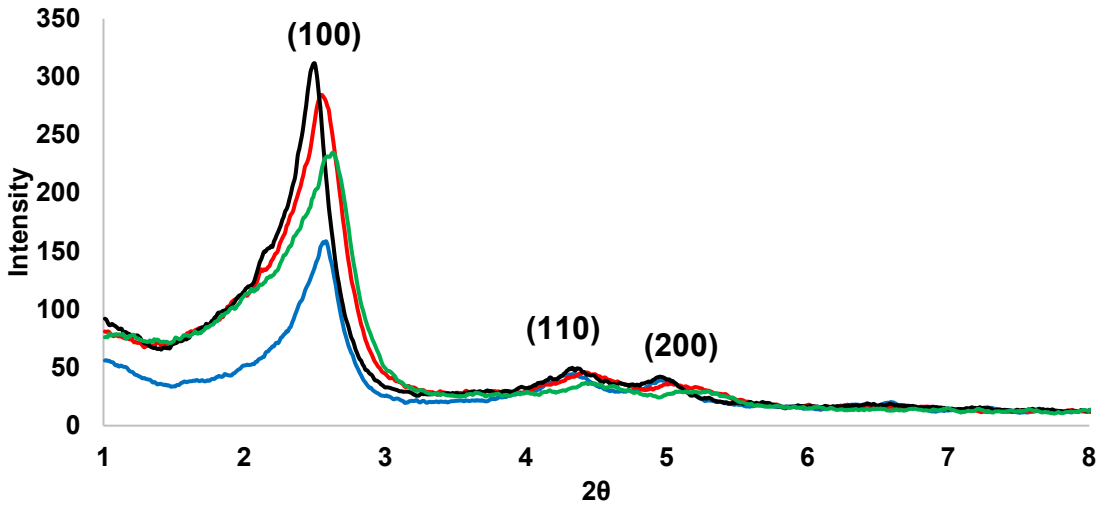

Table 3.4 shows the comparison of the d_{100} and the cell parameter a_0. The intensity of the XRD reflection peaks increased when the amount of de-ionised water was lowered than the amount of de-ionised water used in the

synthesis of MCM-41-35^{0}C standard. MCM-41-35^{0}C (100ml) shows the (100) reflection peak shifting towards the left-hand side, which implies the unit cell size increased the most for this sample. The d_{100} value is the highest for MCM-41-35^{0}C (100ml). The change in the d_{100}, in this case, is not as significant as it was in case of temperature and pH variations (Table 3.1, Page 50) due to the direct effect of pH and temperature on the chemistry of silica formation which governs the whole process of sol-gel.

Table 3.4 Effect of the amount of water on d_{100} and a_0 MCM-41 samples

Sample	d_{100} (nm)	a_0 (nm)
MCM-41-35^{0}C standard	3.4	4
MCM-41-35^{0}C (20ml)	3.5	4
MCM-41-35^{0}C(50ml)	3.4	4
MCM-41-35^{0}C(100ml)	3.6	4

Figure 3.12 Effects of the amount of water on long-range order in MCM-41 versus standard MCM-41 sample

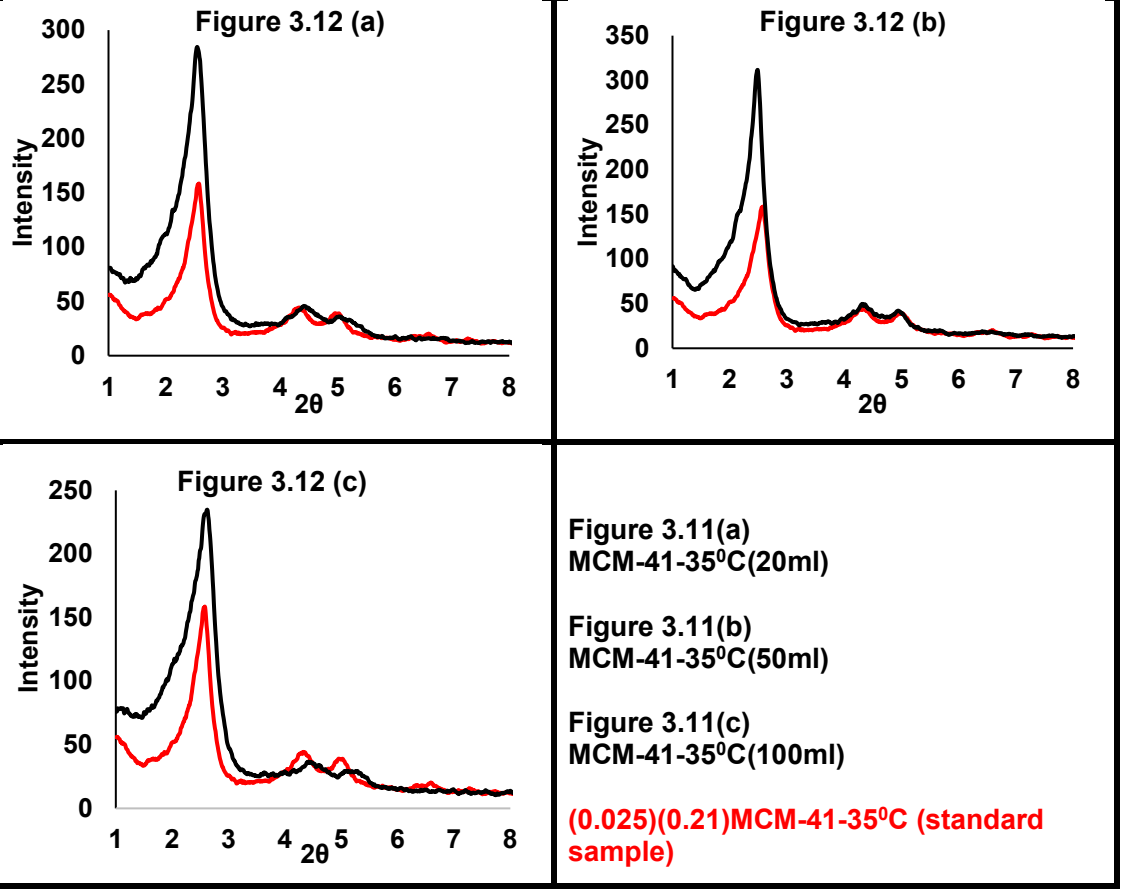

Figure 3.12 shows the comparison of individual samples prepared with different amounts of water. It can be seen that reducing the amount of water the (100) XRD reflection peak was intensified.

Table 3.5 Effect of the amount of water on the composition of MCM-41 samples (EDX)

Sample	Silicon wt. %	Oxygen wt. %	Carbon wt. %
(20ml) MCM-41-35^{0}C	10	36	54
(50ml) MCM-41-35^{0}C	20	42	36
(100ml) MCM-41-35^{0}C	55	45	0

Table 3.5 shows the EDX analysis of the samples shows a significant wt. % of the carbon present in the structure even after calcination. The high amount of unexplained carbon appearing in the EDX results of (20ml) MCM-41-35^{0}C and

(50ml) MCM-41-35^{0}C, shows the samples were not pure siliceous MCM-41. It is necessary to emphasise here that the samples were pulverised before calcination; however, at the end of calcination, they were found in the form of small hard solid lumps. A large amount of carbon present in the EDX results cannot be explained; the synthesis and calcination methods were repeated a few times, but carbon was still present in the EDX results. A possible explanation could be the abnormal growth of silica due to inhibition in the silica hydrolysis caused by a low amount of water.

Figure 3.13 Effect of the amount of water on the MCM-41 morphology

Figure 3.13 (a)
(20ml MCM-41) -35^{0}C
20.0KV 6.4mm x20.0K SE 2.0µm

Figure 3.13 (b)
(50ml) MCM-41-35^{0}C
20.0KV 6.1mm x20.0K SE 2.00µm

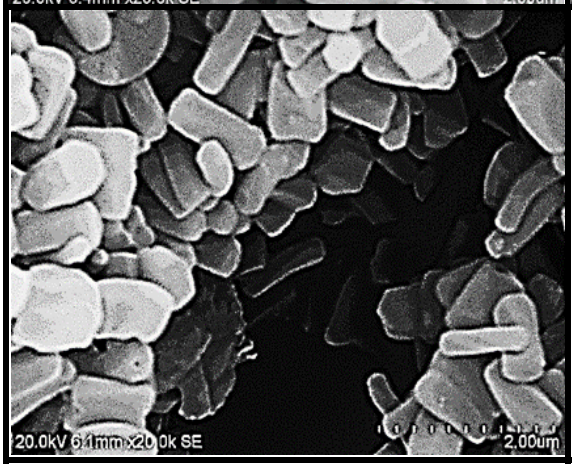

Figure 3.13 (c)
(100ml) MCM-41-35^{0}C
20.0KV 6.8mm x20.0K SE 2.00µm

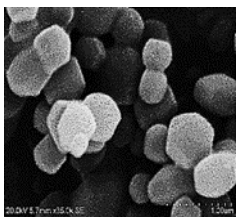

Figure 3.13 (d)
MCM-41-350C (standard)
20.0KV 5.7mm x35.0K SE 1.00µm

Figure 3.13 (a), (b) and (c) show the SEM micrographs of the samples (20ml) MCM-41-35^0 C, (50ml) MCM-41-35^{0}Cand (100ml) MCM-41-35^{0}C. Figure 3.13 (a) shows that the minimum amount of water (20ml) lead to form elongated particles whereas. Figure 3.13 (b) shows worm-like particles where the amount of water used is 50 ml. On further dilution with 100ml of water, the particle morphology changes to the solid rod-like structure in Figure 3.13 (c). Whereas in the case of the standard sample, particles with hexagonal shape are visible in Figure 3.13 (d). The SEM micrograph in (d) is not on the same scale as for the rest of the SEM micrograph due to some trouble with the focus of the microscope, which was later fixed by the lab technicians. From the above SEM micrographs comparison, it is evident that the amount of water has significantly affected the morphology of MCM-41. However, morphology is not the objective of this research.

3.5.1.2 Discussion

Experimental data in this section is limited to explain the behaviour mentioned above definitively. Comparing the SEM scans shown in Figure 3.13 (a) with Figure 3.13 (b) the particle morphology shifted from elongated particles to a thinner worm-like morphology with an increase in the amount of water. Comparing all the SEM micrographs, it is clear that the MCM-41 particles size increased with increasing the amount of water. Low amount of water means the rate of silica growth (silica polycondensation) will be less. Table 3.5 shows a large amount of carbon in the EDX results even after calcination at 550^{0}C for 6 hours such a high amount of carbon is due to the improper distribution of growth rate of silica. Less amount of water causes the concentration of surfactant to increases (as a result the micelle size increases); on the other hand, less amount of water

inhibits silica hydrolysis, which in turn inhibits the condensation of silica into polysilicates. Hence, the distribution of silica growth rate may not be uniform over the assemblies of surfactant micelles (perturbation of the balance between the hydrolysis and polycondensation). EDX results show sample (20ml) MCM-41-35^{0}C exhibits the highest weight % of carbon, even after calcination, due to the least amount of water used in the preparation. Similarly, the sample prepared with the highest amount of water, MCM-41-35^{0}C standard, has the highest amount of silica, and no carbon present at all. The size of the unit cell remained unaffected in these experiments.

3.6 Effect of Aging time

Three samples were prepared as the standard procedure described earlier except the ageing time was altered for; 2hrs, 3hrs, 21 hrs, and 24 hrs. The samples were labelled as follows:

(Ageing time in hours) MCM-41-35^{0}C.

Ageing time did not show a significant effect on the unit cell size and morphology of the material because the precipitation (of solid MCM-41 from the synthesis mixture) is usually complete in the first 2 hours of the synthesis. Further ageing of the solution results in silica restructuring, which translates into an increase in the degree of order (as shown by an increase in the XRD reflection peaks intensities in Figure 3.15 and Figure 3.16. This silica restructuring during ageing is analogous to the restructuring that occurs during the hydrothermal treatment of MCM-41. However, the extent of silica restructuring during hydrothermal treatment is higher than that of ageing, as discussed in Chapter 5. The presence of lumps of the carbonaceous material is visible in the SEM scans in Figure 3.14 (b) and (c). The calcination technique was revised to understand any flaws during

calcination. The samples were finely grounded before subjecting them to calcination still few samples formed tiny aggregates again as described in the previous section. Formation of aggregates shows that some sintering may have occurred during the calcination process.

Figure 3.14 Effect of ageing time on the morphology of MCM-41

Figure 3.14 (a)
(2hrs)MCM-41-35^{0}C
20.0KV 6.6mm x20.0K SE 2.00µm

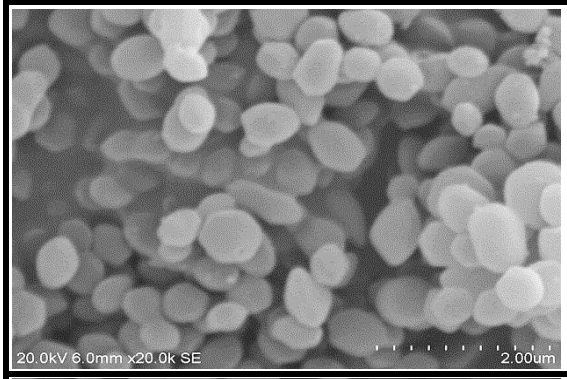

Figure 3.14 (b)
(3hrs)MCM-41-35^{0}C
20.0KV 6.2mm x20.0K SE 2.00µm

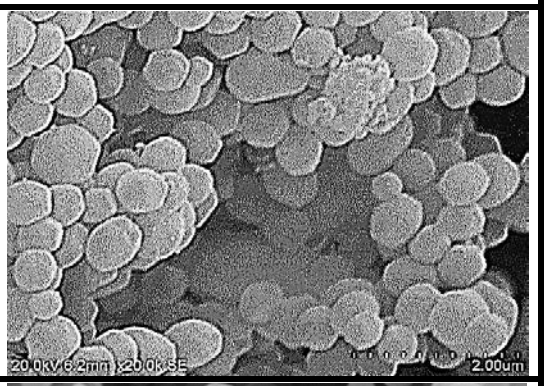

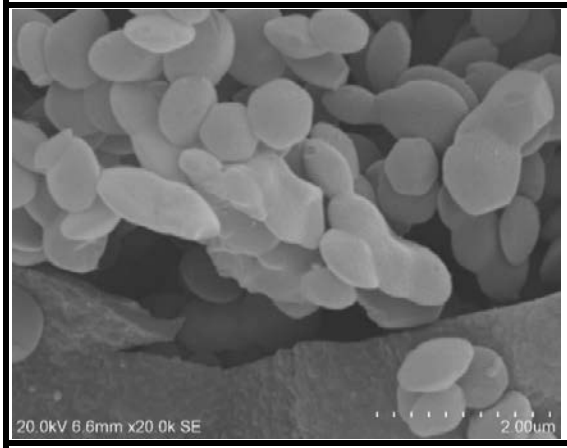

Figure 3.14 (c)
(21hrs)MCM-41-35^{0}C
20.0KV 6.6mm x20.0K SE 2.00µm

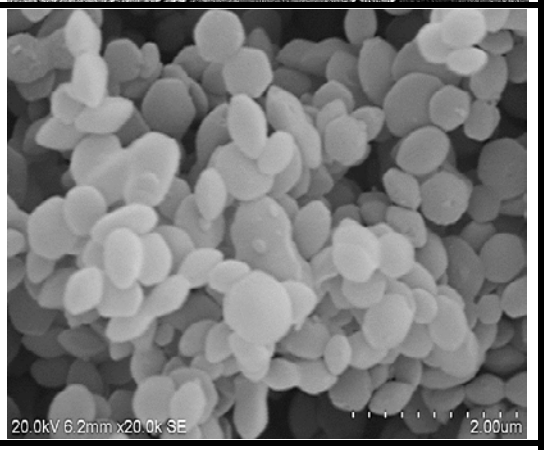

Figure 3.14 (d)
(24hrs)MCM-41-35^{0}C
20.0KV 6.2mm x20.0K SE 2.00µm

3.6.1 Ageing Time Results

3.6.1.1 X-Ray Diffraction

Figure 3.15 shows X-Ray diffraction scans with very narrow and intense XRD reflection peaks which confirms the presence of long-range order in all the samples. Sample (21hrs) MCM-41-35^0 C exhibits the narrowest and steepest peak. Figure 3.16 (a), (b) and (c) show that the (100) peak reflections of the samples prepared wit lower amount of water intensified and shifted further towards the left-hand from the(100) peak reflection of MCM-41-35^{0}C standard.

Figure 3.15 XRD Effect of ageing time on MCM-41 long-range order

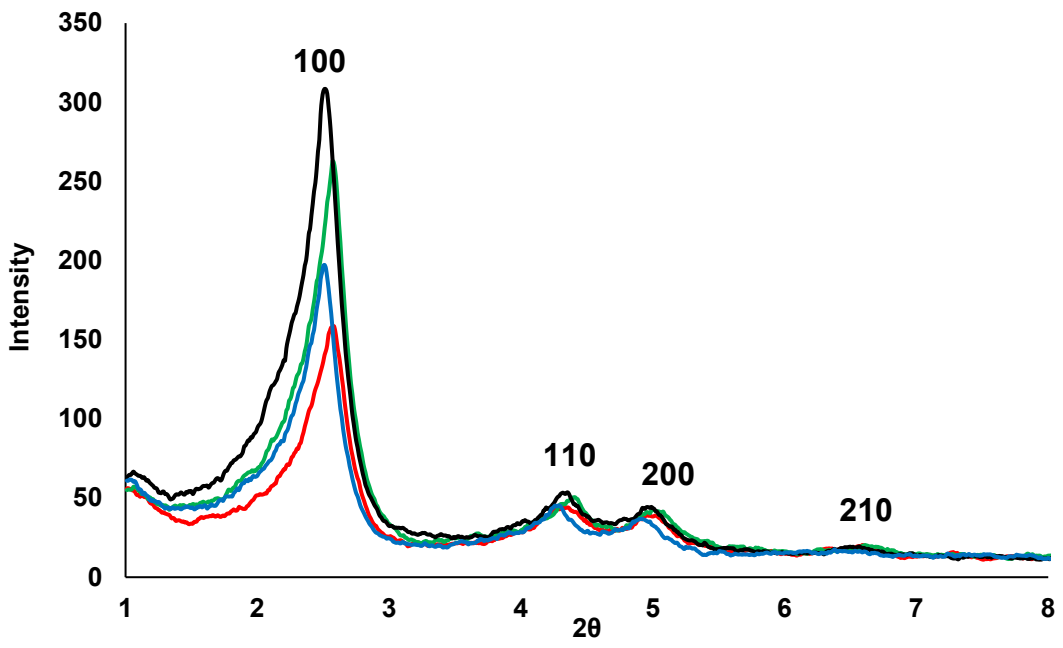

Figure 3.16 Effect of ageing time on the long-rang order studied against standard MCM-41 long-range order.

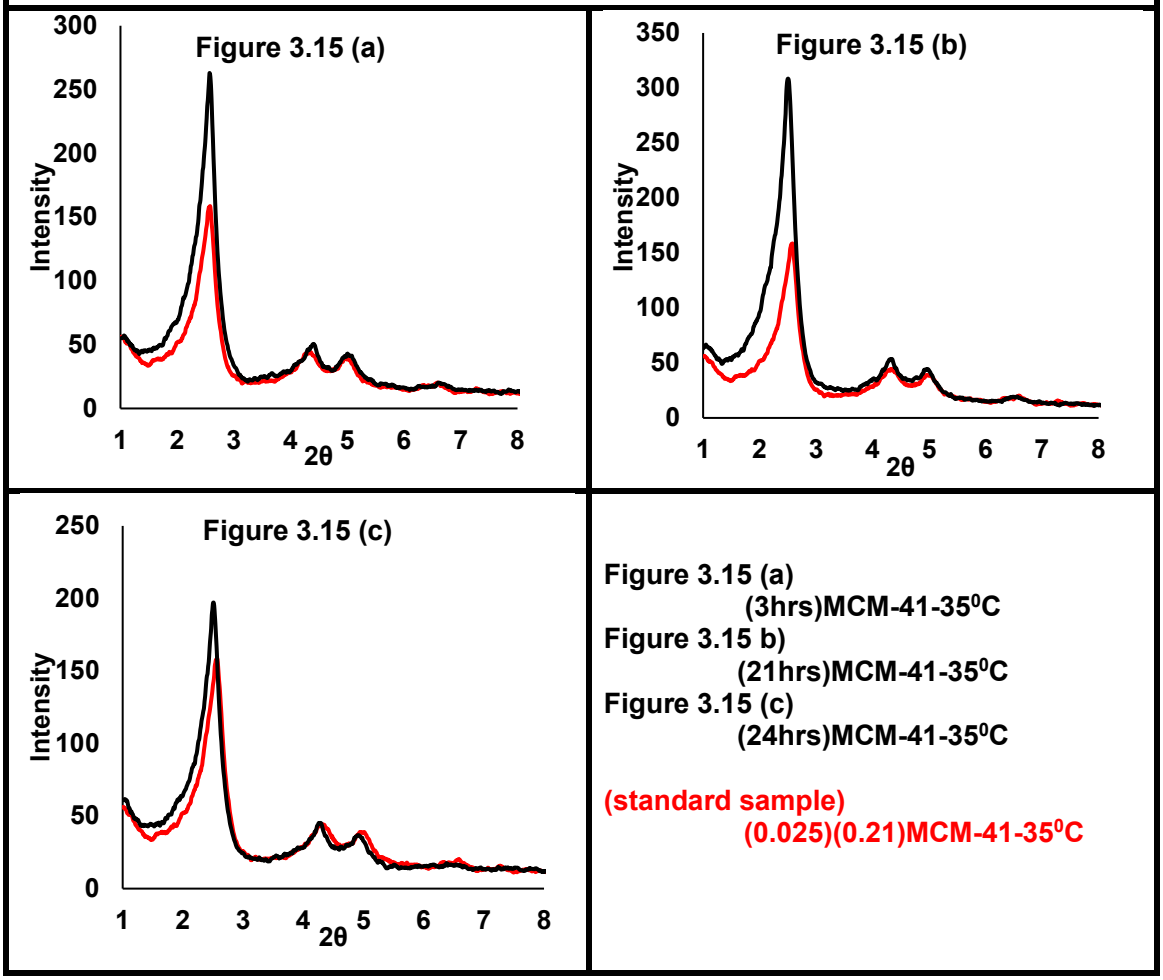

3.6.1.2 Discussion:

Table 3.6 shows a meagre increase in the values of d_{100} *and* a_0 on increasing the ageing times to 21 hours. EDX results in Table 3.7 show that the highest weight % of silicon and oxygen is present in (24 hrs) MCM-41-35^0 C.

Table 3.6 Effects of ageing time on the MCM-41 unit cell expansion

Sample identification	d_{100}	a_0
MCM-41-35^0 C standard	3.4	3.9
(3hrs)MCM-41-35^0 C	3.4	3.9
(21hrs)MCM-41-35^0 C	3.5	4.1
(24hrs)MCM-41-35^0 C	3.5	4.1

Silica form the hexagonal mesoporous order within a short time of 2 hours. However, once the hexagonal mesoporous assembly is formed, increasing the ageing time allows further restructuring of silica to form thicker tube walls (Sajjadi *et al*. 2016).

Table 3.7 Effect of ageing time on the composition of MCM-41

Sample identification	wt. %Silicon	Wt. % Oxygen	Wt. % Carbon
(3hrs)MCM-41-35^0 C	48	42	0
(21hrs)MCM-41-35^0 C	51	48	0
(24hrs)MCM-41-35^0 C	63	37	0

The EDX results shown in Table 3.7 show the wt. % of silica increased an increase in the ageing time. The percentage of silica in the samples, (21hrs) MCM-41-35^0 C and (24hrs) MCM-41-35^0 C is more than the theoretical percentage of Si in SiO_2, which is 47%. The results have been reported as observed. There is a possibility of some instrument error because, during the EDX analysis, 6 to 12 % of C was present in most of the samples which were removed from the spectra by the technician. The technician suggested that the carbon film used on the aluminium alloy stub during the analysis was responsible for 5 to 12% C in the atomic spectra. Removal of this C from the atomic spectra post analysis is also a possible cause of nonstoichiometric percentages of Si and O shown in Table 3.7.

References

Alothman, Z.A. (2012) ‘A Review: Fundamental Aspect of Silicate Mesoporous Materials’, *Materials*, 5(12), pp. 2874.

Brinker, C.J. and Scherer, G.W. (1989) 'Hydrolysis and condensation: Silicates’, *Sol-Gel Science*, U.S. : Academic Press, INC an imprint of Elsevier Science, pp. 97.

Cai, Q., Lin, W.Y., Xiao, F.S., Pang, W,Q., Chen, X.H., Zou, B.S. (1999) ‘The preparation of highly ordered MCM-41 with extremely low surfactant concentration’, *Microporous and Mesoporous Materials*, 32(1-2), pp. 1.

Khushalani, D., Kuperman, A., Ozin, G.A., Tanaka, K., Garces, J., Olken, M.M., and Coombs, N. (1995) ‘Metamorphic Material: Restructuring Siliceous Mesoporous Materials’, *Advanced Materials*, 7(10), pp. 842.

Kruk, M., Sayari A. and Jaroniec, M. (1999) ‘Influence of hydrothermal restructuring conditions on structural properties of mesoporous molecular sieves’, *Microporous and Mesoporous Materials*, 27(2), pp. 217.

Kruk, M., Sayri, A. and Jaroniec, M. (1999) 'A unified interpretation of high-temperature pore size expansion processes in MCM-41 mesoporous silicas', *The Journal of Physical Chemistry*, 103(22), pp. 4590.

Sajjadi, S.A., Izadbakhsh, A. and Niknam, K. (2016) 'Effect of Synthesis Conditions on Textural Properties of Silica MCM-41', *Journal of Oil, Gas and Petrochemical Technology,* 3(1), pp. 59.

Chapter 4

MCM-41 synthesis using tetraalkylammonium bromide salts

4.1 Salt assisted synthesis:

Six trial samples were prepared and characterised using the techniques; XRD, TEM and BET. The samples showed an increase in the long-range order and very high surface areas, as shown in Section 4.2.3 (Page. 90). More samples were prepared using salts ranging from tetramethylammonium bromide to tetraheptylammonium bromide with salt to surfactant ratios from 0.1 to 1.7. Section 4.1.1 describes the synthesis details of the trial samples. The synthesis procedure for standard salt assisted samples is described in 5.1.2. It is noteworthy to mention here that the standard samples were not washed before drying; however, the trial samples were washed three times with de-ionised water before drying in the air (details on Page 76).

4.1.1 Trial salt assisted MCM-41 synthesis

In a typical preparation a particular amount of salt, depending on the salt to surfactant ratio, was dissolved in de-ionised water and heated to the desired temperature (35^0C and 70^0C). The pH was raised to 11 by adding NH_4OH. NH_4OH was also added frequently during the synthesis to keep the pH constant. The amount of NH_4OH used to maintain the pH varied with temperature; therefore, its total amount was omitted in Table 4.1. CTAB was added while vigorously stirring the mixture until a clear solution was observed.

At this point, TEOS was added, and the reaction mixture was aged for 2 hours under vigorous stirring at a constant pH (maintained by the frequent addition of NH_4OH during the synthesis) and temperature. After ageing, the product was washed three times with de-ionised water and then dried in air for 24 hours. Preparation details are tabulated in Table 4.1.

The samples were labelled as follows:

salt name abbreviation $(salt/surfactant)_t$ synthesis temperature

Where,

"t" means trial sample

salt names are abbreviated as follow:

TMABr Tetmethylammonium bromide

TEABr Tetraethylammonium bromide

TPABr Tetrapropylammonium bromide

TBABr Tetrabutylammonuim bromide

Table 4.1 Salt assisted trial samples synthesis

Sample ID	Chemicals					Temperature
Tetraethylammonium bromide						
	H_2O (ml)	CTAB (g)	TEABr (g)	TEOS (ml)	NH_4OH (ml)	(^0C)
$TEABr(0.8)_t70^0C$	270	2	1.0	10	Added during synthesis as required	70
$TEABr(0.6_t)70^0c$			0.7			70
$TEABr(0.6)_t35^0c$			0.7			35
Tetrapropylammonium bromide						
$TPABr(0.8)_t70^0C$	270	2	1.2	10	Added during synthesis as required	70
$TPABr(0.6_t)70^0C$			0.9			70
$TPABr(0.6)_t35^0C$			0.7			35

4.1.2 Standard salt assisted MCM-41 synthesis

The samples prepared in this section are a scaled-up synthesis, as described in Section 4.1.1 (Page 74); to obtain a higher amount of product for hydrothermal treatment. In a typical synthesis, NH_4OH was slowly added in discrete amounts to 710 ml of de-ionised water to adjust pH between 11.3 to 11.5 at 35^0C with continuous stirring. A fixed quantity of tetraalkylammonium bromide salt was dissolved in the solution followed by the addition of 6 g of CTAB under vigorous stirring until a clear solution is formed. The pH of the solution was again adjusted by slowly adding measured amounts NH_4OH. 30 ml of TEOS was added to the mixture. The resulting gel was stirred vigorously for 3 hours, at a maintained pH of 11, then filtered and air-dried for 24 hours. The samples prepared with tetraalkylammonium bromide salts were purposely not washed with de-ionised water before drying in the air because washing would have removed the salt present inside the as-synthesised MCM-41 structure. Hydrothermal treatment of MCM-41 is generally carried out in the mother liquor for optimum pore size expansion (details in Chapter 5), however, carrying hydrothermal treatment in the mother liquor under high autogenous process was deemed hazardous by the university laboratory technicians claiming that NH_4OH liberates NH_3 at high hydrothermal treatment temperature, generating a dangerously high-pressure build-up inside the autoclave. For the same reason, technicians also discouraged the addition of NH_4OH to de-ionised water for pH stabilisation during hydrothermal treatment.

The samples were calcined at 550^0C at the rate of 1^0C/min for 6 hours then cooled to the ambient temperature at the rate of 10^0C/min.

The standard samples were labelled with the same scheme as shown above, except the suffix “t” was removed. The sample subjected to hydrothermal treatment was labelled as MCM-41-TEABr-(0.8) to distinguish it from the other samples.

4.2 Salt assisted MCM-41 samples (trial samples and standard) results:

4.2.1 X-Ray Diffraction

4.2.1.1 Trial salt assisted MCM-41 samples XRD results

Table 4.2 Effects of salts on the unit cell size of MCM-41		
Tetraethylammonium bromide		
Sample ID	d_{100} (nm)	a_0 (nm)
TEABr(0.8) $_t$ 70^{0}C	3.6	4.2
TEABr(0.6) $_t$ 70^{0}C	3.4	4.0
TEABr(0.6) $_t$ 35^{0}C	3.7	4.2
Tetrapropylammonium bromide		
TPABr(0.8) $_t$ 70^{0}C	3.4	4.0
TPABr(0.6) $_t$ 70^{0}C	3.5	4.0
TPABr(0.6) $_t$ 35^{0}C	3.7	4.2

Figure 4.1 (a) and (b) show the comparison of the XRD peaks of the samples prepared with tetraethylammonium bromide and tetrapropylammonium bromide, respectively. It can be seen in the figures that all the samples exhibited four distinct characteristic XRD reflection peaks of MCM-41. The figures clearly show that the samples prepared at 35^{0}C exhibited the most prominent and intensified (100) reflection peaks for both salts. The standard salt assisted syntheses were, therefore, carried out at 35^0 C. Table 4.2 shows the d_{100} and a_0 values of both sets of the trial samples. The highest values of d_{100} and a_0 were shown by samples prepared at 35^{0}C at salt to surfactant ratio of 0.6.

Figure 4.1(a) Comparison of long-range order among tetraethylammonium bromide assisted trial samples

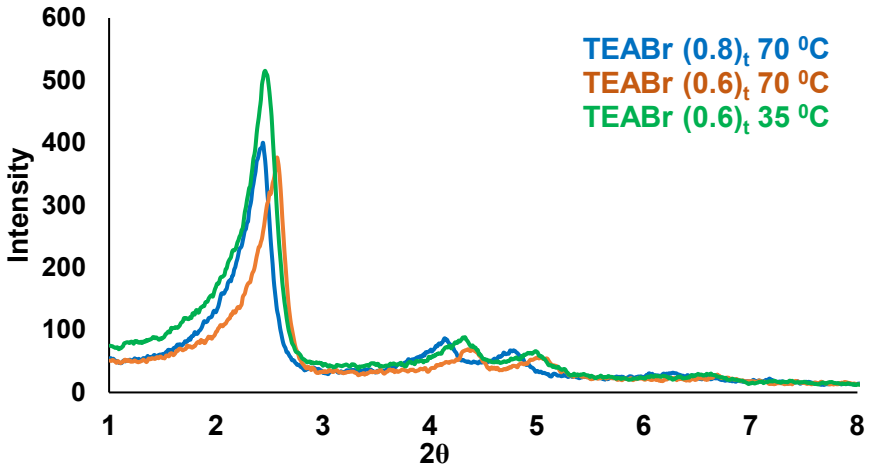

Figure 4.1 (b) Comparison of long-range order among tetrapropylammonium bromide assisted trial samples

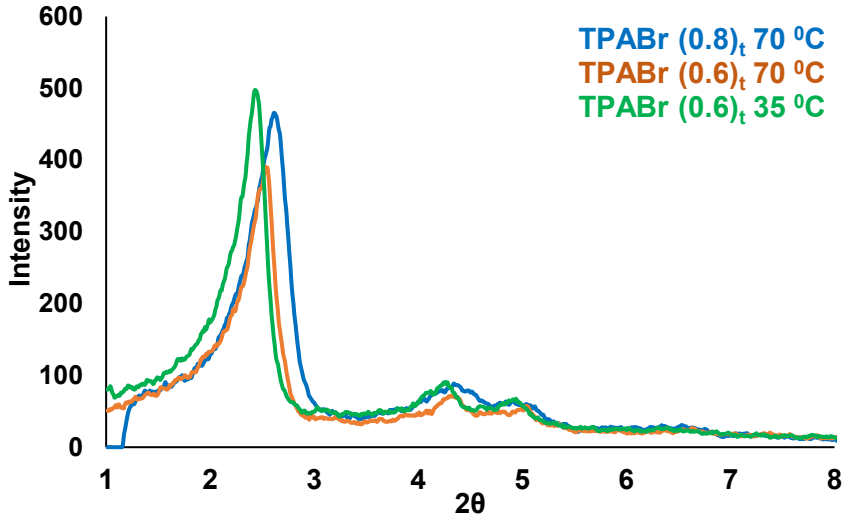

4.2.1.2 *Standard salt assisted MCM-41 samples XRD results*

The comparison of the heights of the XRD reflection peaks shows the extent of the degree of long-range order in each sample. Figure 4.2 to Figure 4.5 show a comparison of the most intense XRD reflections from each salt. It can be seen that all the samples were highly ordered and exhibited four distinct characteristics XRD reflection peaks at (100)(110)(200) and (210) planes. Figure 4.2 to Figure 4.5 show that the intensity of the XRD peak was affected by the salt to surfactant ratio. Hence, the characteristics of the salt assisted MCM-41 depended on the salts as well as on the salt to surfactant ratio.

Figure 4.2 Comparison of long-range order in tetramethylammonium Bromide salts/Surfactant=0.1 to 1.7

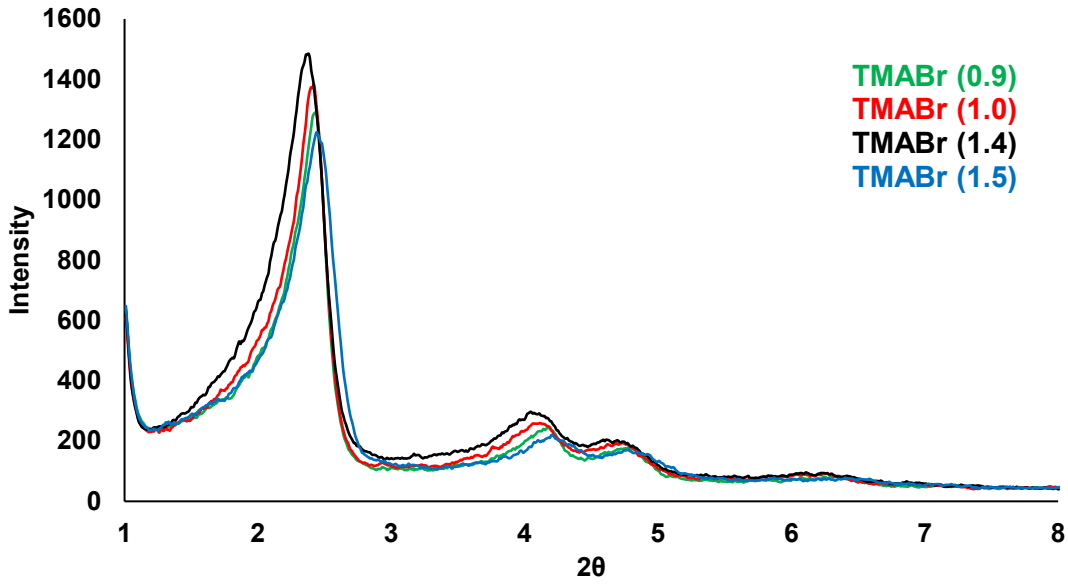

The significance of the salt assisted MCM-41 synthesis is also confirmed by the nitrogen physisorption analysis discussed on Page 86. The sample prepared with tetraethylammonium bromide to CTAB ratio of 0.8 exhibited an exceptionally high surface area not reported earlier in the literature.

Figure 4.3 Comparison of long-range order in tetraethylammonium bromide salt/surfactant= 0.1 to 1.6

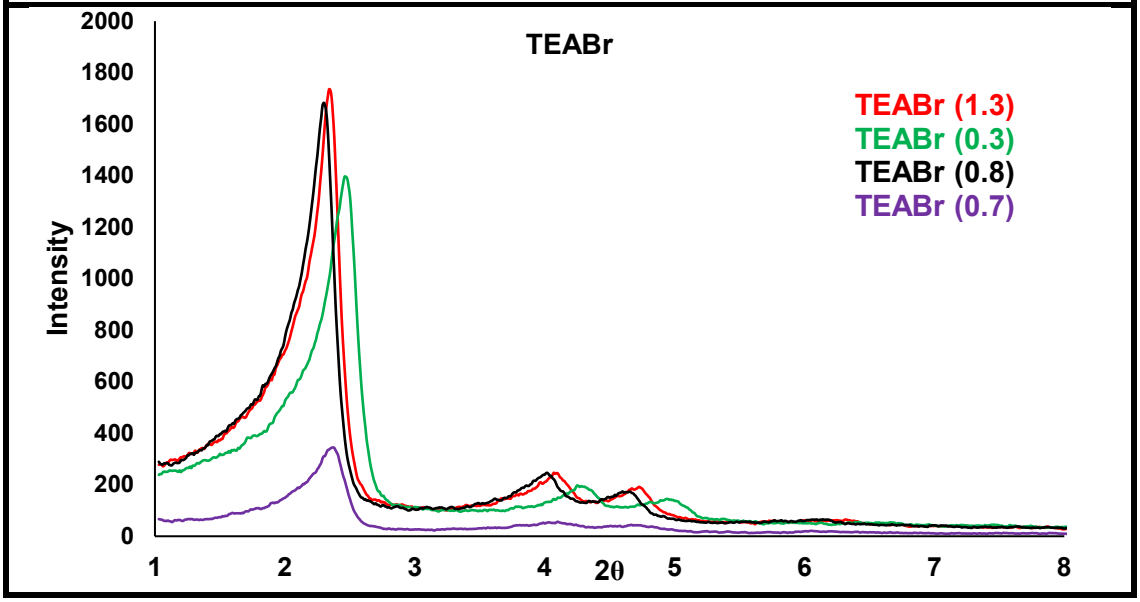

Figure 4.4 Comparison of long-range order in tetrapropylammonium Bromide salt/surfactant= 0.1 to 1.7

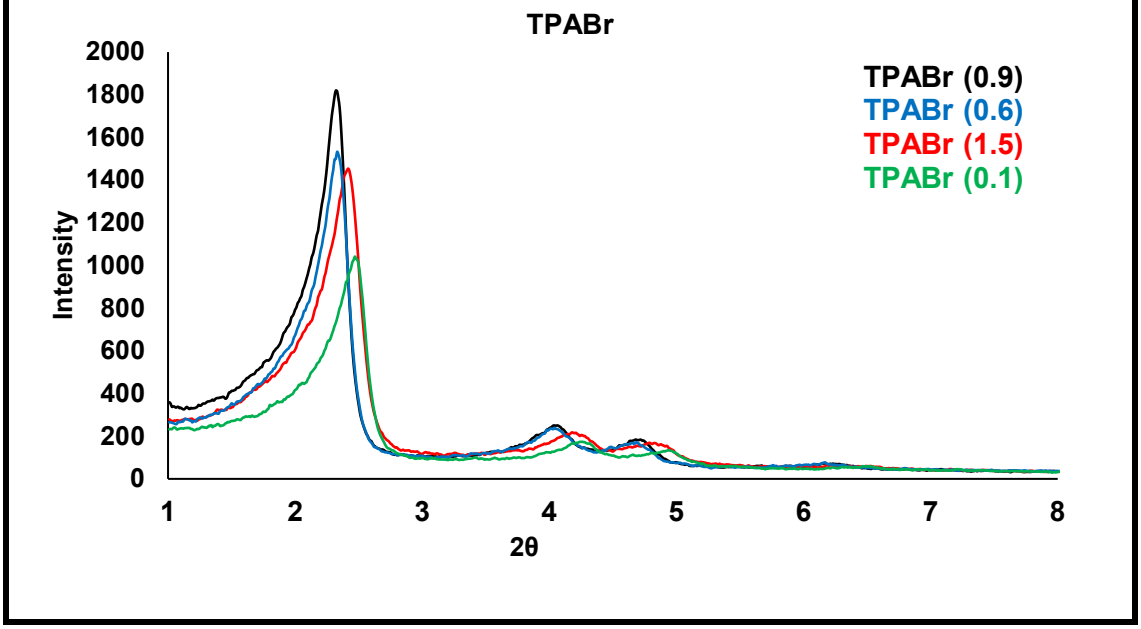

Figure 4.5 Comparison of long-range order in tetrabutylammonium Bromide salt/surfactant= 0.1 to 1.7

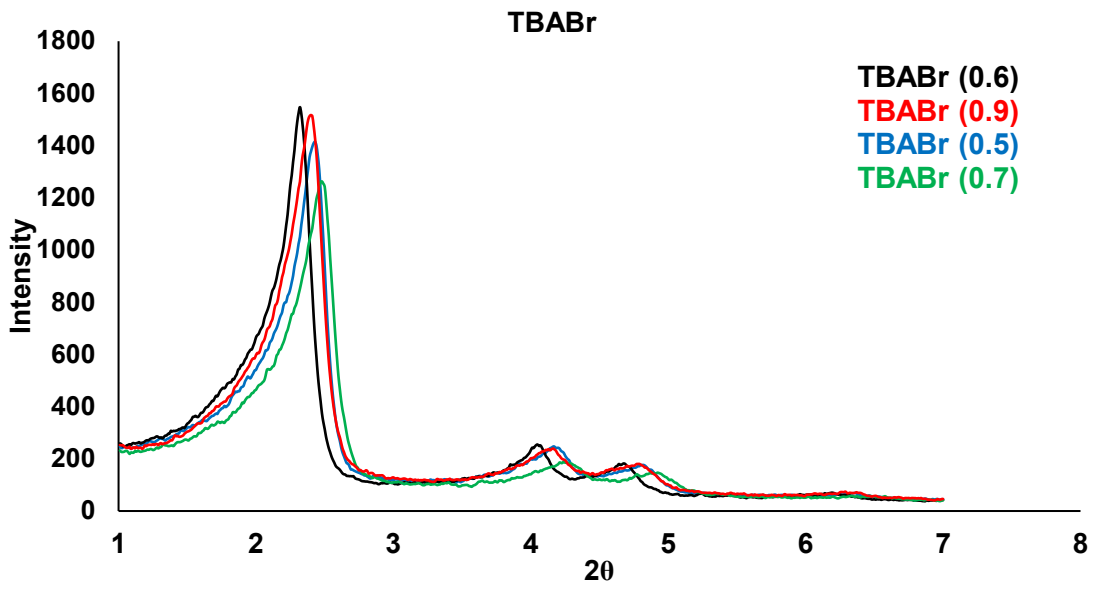

Based on the intensity of the XRD reflection, one sample from each salt was selected for the comparison shown in Figure 4.6 (a) and (b). It was observed that the highest XRD reflection peak was exhibited by the sample TPABr (0.9). Based on the intensity of the XRD reflection peak, this sample was considered the most highly ordered MCM-41 among the other salt assisted MCM-41 samples. The XRD reflection peaks alone, however, cannot be a criterion to predict the characteristics of a material.

The lowest peak, on the other hand, was exhibited by TMABr(1.4). In Figure 4.6 (b) the height of the XRD reflection peaks, for sample TMABr (1.4), at (100), (110), (200) and (210) reflections are much higher than the corresponding XRD reflections of the standard sample (0.025)(0.21)MCM-41-35^0 C showing the long-range order tremendously improved with salt addition (even for the sample with the lowest XRD reflection peak intensity).

Figure 4.6 (a) Comparison of the most highly ordered sample from each salt assisted MCM-41

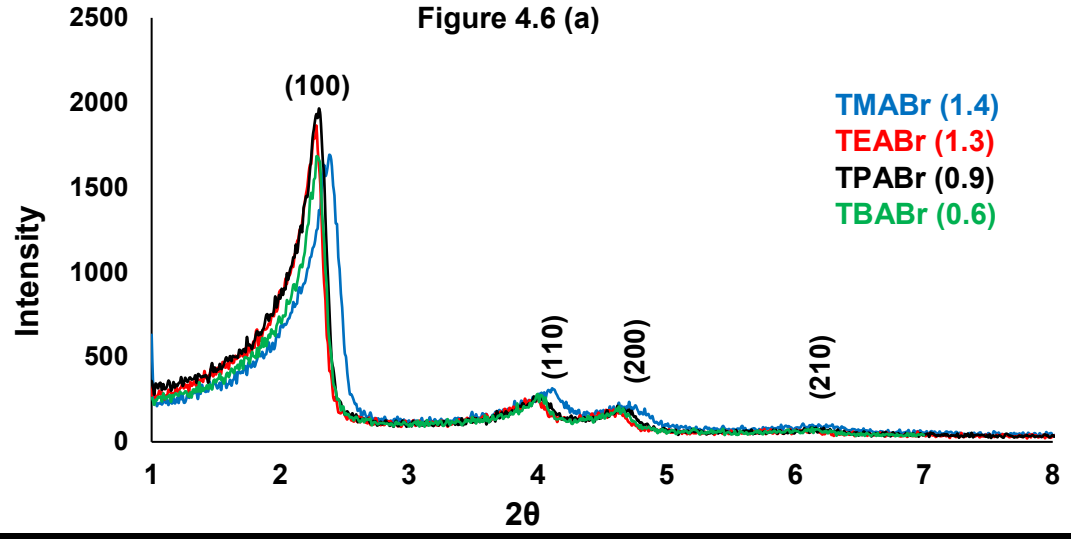

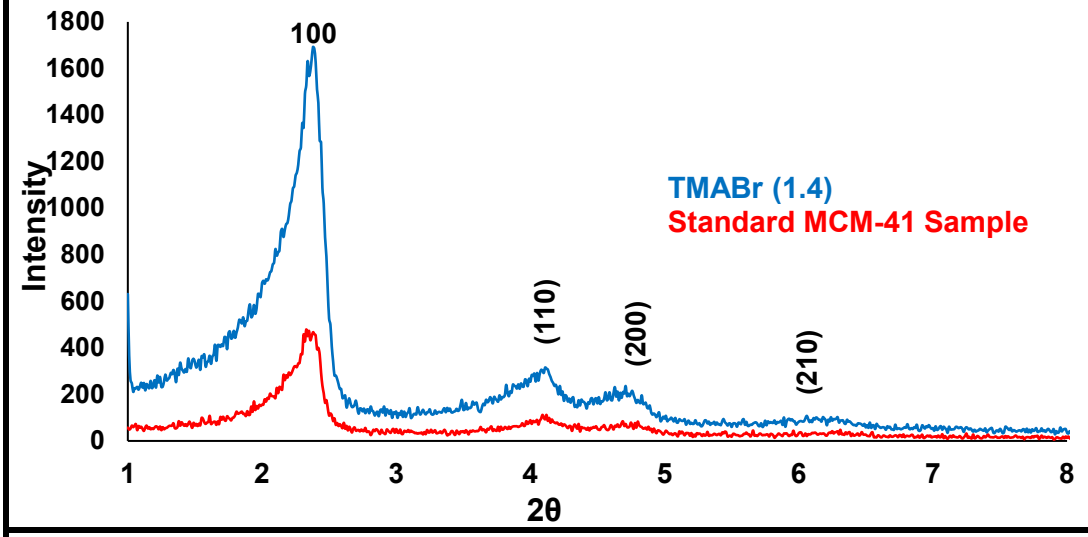

4.6 (b) Comparison of the range order between TMABr (1.4) and standard MCM41 sample

Table 4.3 d_{100} and a_0 of salt assisted samples at different salt to surfactant ratios								
Salt / Surfactant	TMABr		TEABr		TPABr		TBABr	
	d_{100}	a_0	d_{100}	a_0	d_{100}	a_0	d_{100}	a_0
0.1	3.5	4.1	3.5	4.1	3.6	4.2	3.6	4.2
0.2	3.5	4.1	3.5	4.1	3.7	4.3	3.5	4.1
0.3	3.7	4.3	3.5	4.1	3.7	4.2	3.6	4.1
0.4	3.5	4.1	3. 7	4.3	3.7	4.2	3.6	4.1
0.5	3.5	4.1	3. 7	4.3	3.7	4.3	3.7	4.3
0.6	3.5	4.1	3.8	4.4	3.7	4.2	3.9	4.5
0.7	3.5	4.1	3. 7	4.3	3.7	4.3	3.6	4.2
0.8	3.7	4.3	3.8	4.4	3.7	4.3	3.7	4.3
0.9	3.7	4.3	3. 7	4.3	3.8	4.4	3.7	4.3
1.0	3.7	4.3	3.5	4.1	3.7	4.3	3.7	4.2
1.1	3.5	4.1	3. 7	4.3	3.7	4.3	3.7	4.3
1.2	3.4	4	3. 7	4.3	3.8	4.3	3.7	4.3
1.3	3.7	4.3	3.8	4.4	3.8	4.4	3.7	4.2
1.4	3.7	4.3	3.8	4.4	3.7	4.3	3.8	4.4
1.5	3.7	4.3	3.8	4.4	3.7	4.3	3.6	4.1
1.6	3.7	4.3	3.8	4.4	3.8	4.4	3.7	4.2
1.7	3.5	4.1					3.8	4.4

Table 4.3 shows the d_{100} and a_0 did not change significantly with a change in the salt to surfactant ratios. However, the height of the XRD reflection peak increased, as the salt to surfactant ratio decreased with an increase in the alkyl chain length.

For instance, Figure 4.2 to Figure 4.5 show that the samples exhibiting the highest XRD peaks among MCM-41 samples synthesised from tetramethylammonium bromide, tetraethyammonium bromide, tetrapropylammonium bromide and tetrabutylammonium bromide were at salt to surfactant ratio of 1.4, 1.3, 0.9, and 0.6 for respectively. The comparison of the XRD reflection peaks and d_{100} values confirmed that the effect of salts to surfactant ratio on the improvement of MCM-41 long-range order is crucial. Comparison of (100) XRD reflection peaks is a handy tool in establishing the degree of order of a given MCM-41 sample. However, other characterisation techniques such as; surface area, pore size, pore volume and pore wall thickness are also essential to establish the superiority of a sample. BET results of the sample TEABr-MCM-41(0.6) $_{trial}$ 35^0C are described in Section 4.2.3.1 (Page 86). The sample has a very high surface area of 1380 m^2g^{-1}.

4.2.2 Transmission Electron Microscopy (TEM) Results (Trial salt assisted MCM-41 only)

Figure 4.7 TEM Images of the trial sample TEABr-MCM-41(0.6)$_{trial}$ 35^{0}C

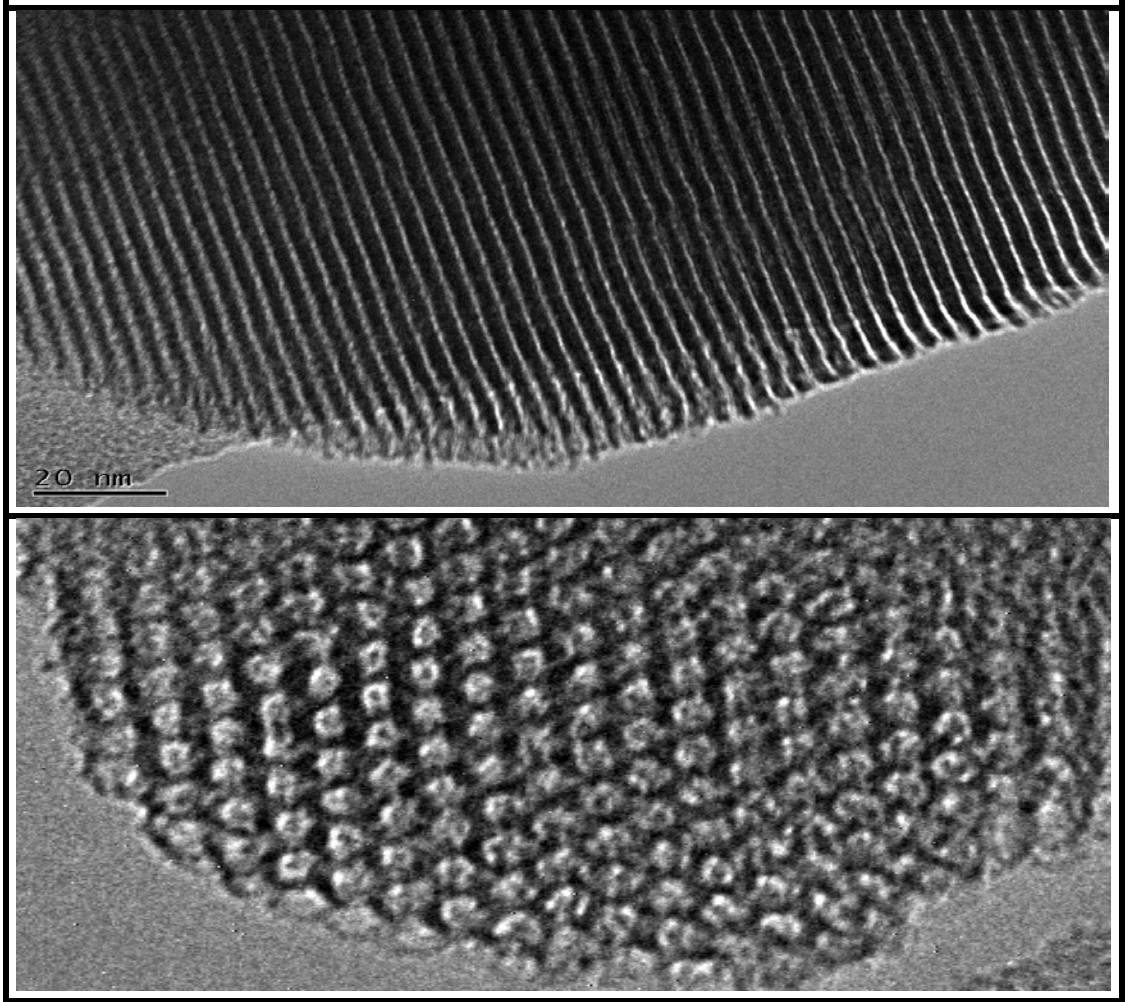

Figure 4.7 shows the TEM images of the sample TEABr-MCM-41(0.6) $_{trial}$ 35^{0}C. The sample exhibited a hexagonal honeycomb structure. The XRD and TEM results have confirmed that the sample was highly ordered; therefore, TEM images were used to calculate the pore diameter and the pore wall thickness of the samples. The interplanar distance d_{100} measured from TEM images was compared with the d_{100} calculated from XRD results. The values of d_{100} measured

from TEM images were not close to the d_{100} values calculated from XRD analysis, as shown in Table 4.4.

Table 4.4 TEM and XRD results comparison

Samples	TEM Results (nm)				XRD Results (nm)			
	d_{100}	a_0	d * pore	t **	d_{100}	a_0	d* pore	t **
TEABr(0.8)$_{trial}$ 70^0 C	3.5	4	3	1	4.1	4.7	3	1.7
TPABr(0.8)$_{trial}$ 70^0 C	3.5	4	2.6	1.4	3.6	4.2	2.6	1.6
TEABr(0.6) $_{trial}$ 35^{0}C	3.2	3.7	2.3	1.4	4	4.6	2.6	2.0
*d pore is the average pore diameter was calculated from the TEM images **t is the pore wall thickness calculated as t = (a_0 – d_{pore})								

Pore wall thickness was calculated by subtracting the pore width from the cell parameter values (from XRD and TEM). The TEM images for other samples tabulated in Table 4.4 are identical to TEABr (0.6) $_{trial}$ 35^{0}C; therefore, not presented here. The pore wall thickness for samples, TEABr (0.6) $_{trial}$ 70^{0}C and TEABr (0.6) $_{trial}$ 35^{0}C; calculated by TEM and XRD do not match because the pore wall thickness depends upon the value of a_0, which was different in both cases. The values for the XRD results were considered more reliable than those measured from the TEM images because the TEM values were estimated using the transmission electron micrographs using a ruler or a software.

4.2.3 Nitrogen physisorption analysis

4.2.3.1 Nitrogen physisorption analysis of trial salt assisted MCM-41 samples

Sample, TEABr (0.6) $_{trial}$ 35^{0}C, was selected from trial samples for nitrogen physisorption analysis at Lucite International. The sample TEABr (0.6) $_{trial}$ 35^{0}C showed an exceptional surface area of 1384m^{2}g^{-1} with a very narrow pore size

distribution between 2.1 to 3.0 nm, as shown in Figure 4.8. Sample TEABr (0.6) $_{trial}$ 35^0C exhibited the thickest pore wall among the trial samples.

When the salt to surfactant ratio was increased in the synthesis of the standard samples; TEABr (1.3) showed a pore wall of 3.2 nm thicker than the pore wall of the trial sample TEABr (0.6) $_{trial}$ 35^0C; however, sample TEABr (1.3) had microporosity, as discussed in Section 4.2.3.2 (Page 90). The comparison of the pore wall thickness is important as the hydrothermal stability of MCM-41 depends upon the thickness of the pore wall.

Figure 4.8 Hysteresis loop and pore size distribution of trial sample TEABr-MCM-41- (0.6) $_{trial}$ 35^{0}C

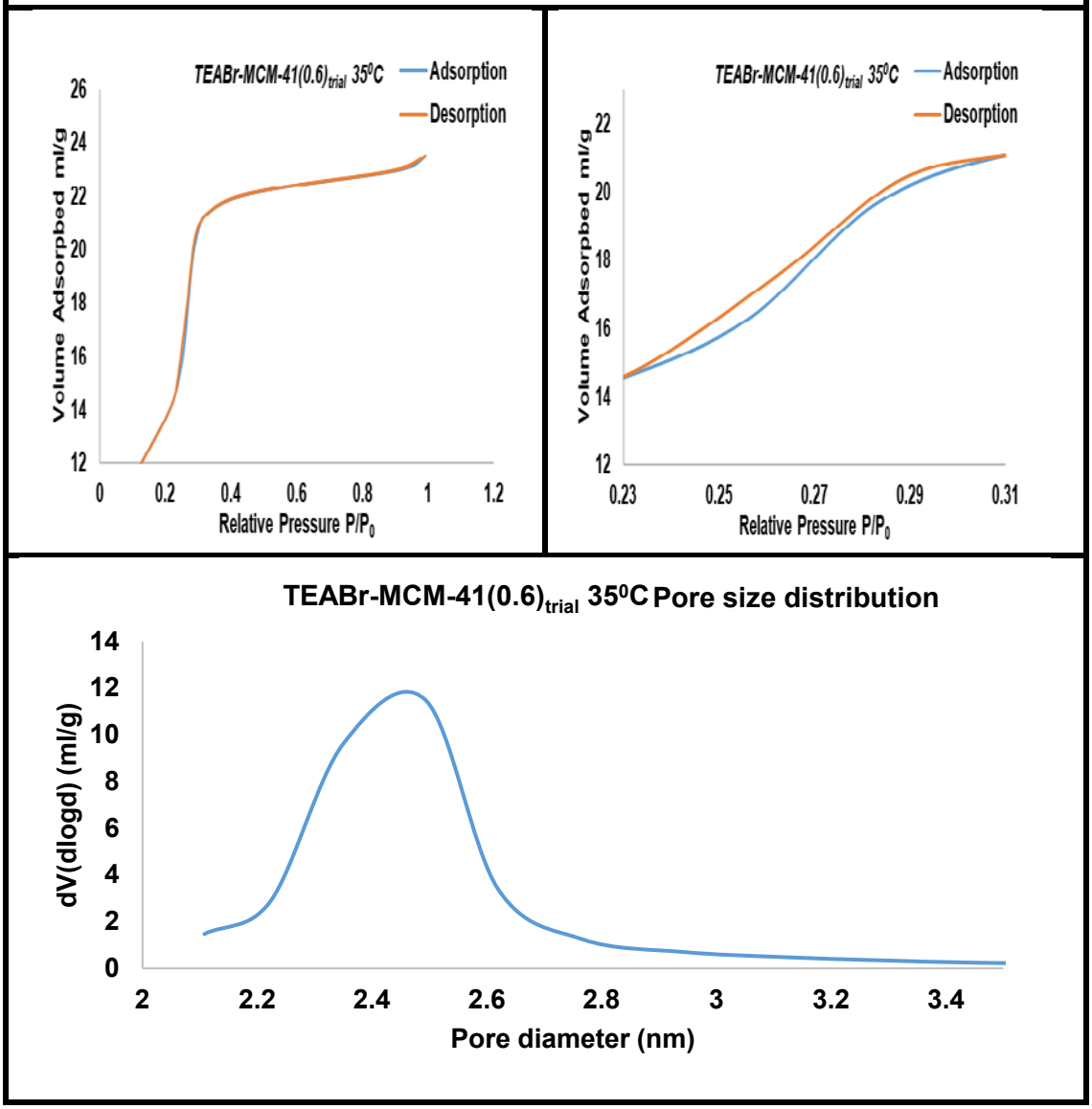

The hysteresis loop of trial sample:

Figure 4.8 shows a type IV isotherm with an H1 type hysteresis loop according to the IUPAC classification of adsorption-desorption isotherms (Thommes, 2010 and Thommes *et al.*, 2015). The hysteresis loop in Figure 4.8 is very narrow, with a lower closure point at P/P_0 value of 0.023 and an upper closure point at a P/P_0 value of 0.31. During the first phase of physisorption between P/P_0 range of 0.01 to 0.2, the micropores are filled. The adsorption-desorption in micropores

depends solely on the interaction between N_2 molecules and the pore walls. Since the width of micropores is in the order of one or two molecular dimensions; therefore, the adsorption potential of the opposite walls is overlapping. Hence, the filling of the pores takes place as a continuous process, and no phase transition takes place.

On the other hand, the adsorption in mesopores involves not only the interaction between the pore walls and N_2 molecule but also the interaction among the N_2 molecules; this results in multilayer adsorption of N_2 followed by capillary condensation. At $P/P_0 > 0.2$, the pore walls are covered with multilayer adsorption film, as the adsorption film thickness increases, the interactions among the N_2 molecules start overcoming the adsorption potential of the pore walls. As a result, the pore wall to N_2 molecules interaction reduces. After a certain critical multilayer thickness, the intermolecular interactions among the fluid molecules completely overcome the adsorption potential of the pore walls. At this stage, the multilayer film becomes metastable, leading to the formation of nucleated liquid bridges by capillary condensation (precisely called pore condensation) inside the cores of pores. The nucleated liquid bridges are a liquid-like phase in which the partial pressure of the gas/vapour is less than the saturation pressure in the bulk fluid.

From the above explanation, it is understood that the metastabilities associated with the nucleated liquid bridges, formed during adsorption in mesopores, delay the condensation. Once the liquid-like condensate fills all the pores at the end of adsorption, the liquid-vapour interface is established, and desorption can take place via receding meniscus. This delayed condensation in the mesopores due to the metastabilities associated with the nucleation of liquid bridges during adsorption give rise to the hysteresis loop of type H1 (Sing and Williams 2005;

Thommes, 2010; Monson 2012; Nguyen and Nicholson, 2013; Sun *et al.*, 2017; Zeng *et al.*, 2017).

Pore size distribution in the trial sample:

Figure 4.8 shows a pore size distribution between 2.1 to 3 nm for the trial sample TEABr-MCM-41(0.6)$_{trial}$ 35^0C. The pore size distribution is very narrow, showing the sample comprised of highly ordered pore network with facile pore connectivity.

4.2.3.2 Nitrogen physisorption analysis of standard salt assisted MCM-41 samples

The BET results for samples TMABr (1.4), TEABr (1.3), TEABr-MCM-41-(0.8), TEABr (0.6), TPABr (0.9) and TBABr (0.6) are tabulated in Table 4.5. The sample TEABr-MCM-41-(0.8) exhibited the highest surface area of 3140 m^2g^{-1} which has not been reported for MCM-41 before in the literature. It is interesting to note that the surface area increased from 1384 m^2g^{-1} to 3140m^2g^{-1} (rounded off to 3000 m^2g^{-1} in the rest of the thesis) with a meagre increase in the salt to surfactant ratio from 0.6 to 0.8. The pore diameter and pore wall thickness estimated using TEM images and XRD calculations in Table 4.4 (Page 86) for sample TEABr (0.6) are closer to those calculated from BET surface area measurements (Table 4.5, Page 91). Table 4.5 also shows that the samples prepared with tetraethylammonium bromide exhibited a decline in the characteristics at salt to surfactant ratios higher than 0.8. For TEABr (1.3), which exhibited the highest XRD reflection peaks among TEABr based preparations , the pore diameter was 1.2 nm which showed the sample was not even mesoporous. The pore wall thickness of TEABr(1.3) was 3.2 nm which was the thickest among all the samples analysed, as shown in Table 4.5.

Table 4.5 Nitrogen physisorption analysis of standard salt assisted samples				
Sample ID	Surface Area ($m^2g^{-1)}$	Average pore diameter d_{pore} (nm)	Pore Volume (cm^3g^{-1})	Pore wall thickness $t=(a_0-d_p)$ (nm)
TMABr (1.4)	1375	2.6	0.9	1.6
TEABr (1.3)	728	1.2	0.4	3.2
TEABr-MCM-41-(0.8)	3140	2.5	2	1.9
TEABr (0.6)	1384	2.4	0.8	2.2
TPABr (0.9)	1022	2.6	0.6	1.8
TBBr (0.9)	1129	2.6	0.8	1.9

Nitrogen physisorption isotherms have also been studied to understand the pore size distribution and pore connectivities of MCM-41 salt assisted samples. The samples TMABr (1.4), TEABr (1.3), TPABr (0.9) and TBABr (0.6) were selected from the respective salts due to their most intensified XRD peaks. Figure 4.9 shows the comparison of the adsorption/desorption isotherms of the samples TMABr (1.4), TEABr (1.3), TPABr (0.9) and TBABr (0.6) and their BET analysis.

Hysteresis Loop:

Figure 4.9 shows the plot of relative partial (P/P_0) pressure against dv(logd). The adsorption isotherms are of type IV with type H1 hysteresis. According to the IUPAC classification of adsorption isotherms, type IV (a) isotherm represents mesoporous material, and the H1 type of hysteresis loop shows a very narrow range of highly ordered cylindrical pores with face to face pore connectivity. Figure 4.9 confirmed the presence of an extremely close range of ordered cylindrical pores with rigorous facile pore connectivity in all the samples except TEABr 1.3. The isotherm for TEABr (1.3) belongs to the isotherms type I (a) representing microporous materials (Thommes *et al.*, 2015). The average pore

diameters listed in Table 4.5 (Page91), confirm that the sample TEABr (1.3) is microporous with 1.2 nm average pore diameter.

Figure 4.9 Hysteresis loop comparison of salt assisted standard MCM-41 samples

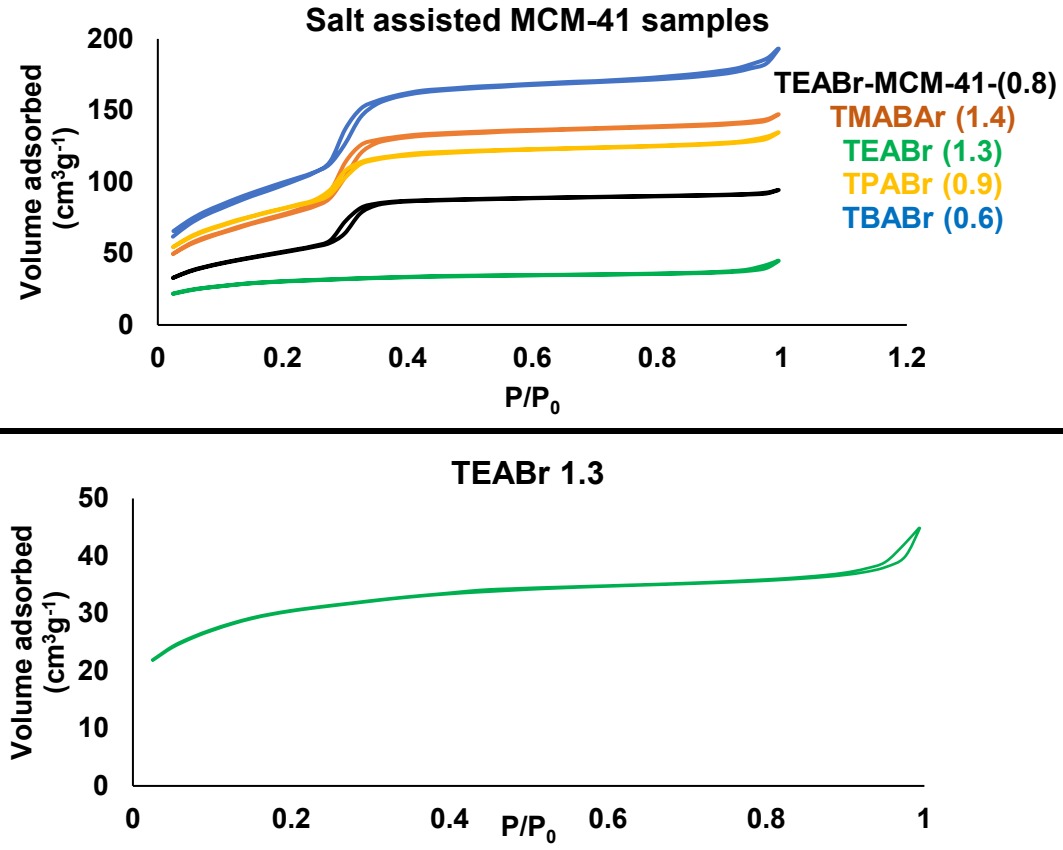

Hysteresis loop of TEABr (1.3)

Figure 4.9 shows that the adsorption started at low relative pressure value of 0.025 for all the samples. The volume of N_2 adsorbed at the low-pressure stage of P/P_0 = 0.025 ranged between 22 to 62 cm^3g^{-1}. The high volume of N_2 adsorption at a low relative pressure confirmed the presence of highly uniformed mesoporous structure having cylindrical pores with facile pore connectivity (Sun *et al.*, 2017). The adsorption increased steadily during the low-pressure zone and then exhibited an exponential curve at a relative pressure of 0.25 (lower closure point) the volume adsorbed at this point ranged 57 to 112 ml/g. This sharp increase in the volume of N_2 adsorbed was due to multilayers adsorption,

indicating the presence of mesopores. The sharp increase in the volume of N_2 adsorbed was only short-lived and became steady again when it reached a relative pressure value of 0.38 and then increased again in the high-pressure region P/P_0 =1. The desorption curve was steady until P/P_0= 0.38, then showed a sharp decline in the volume adsorbed due to the emptying of the mesopores.

Pore size distribution

According to Figure 4.10, the majority of the pores were between a narrow pore diameter range of 2.3 to 3.2 nm. It is noteworthy to mention that the pore size distribution for sample TEABr (1.3) was flat as compared to the rest of the sample. TEABr (1.3) was microporous; hence, its pore size distribution was not prominent. It is also interesting to note that the pore size distribution peak was the highest for TEABr 0.8, which exhibited an ultra-high surface area of 3000m^2g^{-1}not reported before.

Figure 4.10 Pore size distribution comparison of salt assisted MCM-41 samples.

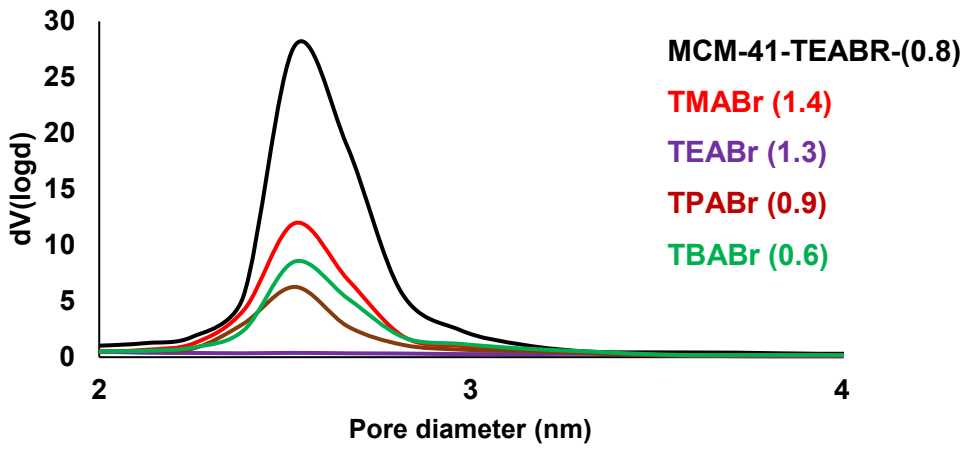

4.3 Overall discussion for salt assisted MCM-41 synthesis

Several researchers have prepared salt incorporated MCM-41 samples using different methods to improve the characteristics of MCM-41. The way how salts affect the characterisation of MCM-41 depends on the chemistry of the salt as well as on how it is incorporated in the synthesis. Varade *et al.* (2005) studied the effect of inorganic salts (NaCl and NaBr) on the micellization of cetylpyridinium chloride. They observed an increase in the micelle size of MCM-41 on increasing the concentration of NaBr and NaCl above a threshold value and Br^- having a more pronounced impact on the micellisation of cetylpyridinium chloride than the Cl^-. Their research concludes that the addition of salts increases the size of micelles; the effect of the salts on the surface area, pore diameter and other surface properties of MCM-41 have not been discussed. Inorganic salts have not been used in the current research to avoid the risk of intrusion of Na ions into the MCM-41 lattice. It has been already mentioned that the presence of Na ions in the MCM-41 lattice can be detrimental to the hydrothermal stability of MCM-41. Kim *et al*. (2002) have mentioned another way of using organic and inorganic salts to improve the hydrothermal stability of MCM-41. They added different salts after the gel formation and the resulting materials were hydrothermally stable for 12 hours when boiled in water under reflux conditions. The samples prepared by the addition of salt to the surfactant solution before the addition of silica precursor lead to disordered materials. In the current research, the salts were added before the addition of silica precursor to attain the maximum effect of salts on the micellisation as reported by Varade *et al.* (2005) as well as utilising them for stability improvement. In the current study, no structure deteriorating effects were observed on the MCM-41 samples due to salt addition before gel formation.

On the contrary, the MCM-41 prepared in this research by salt addition before tetraethylorthosilicate addition were highly ordered.

some researchers have used tetramethylammonium hydroxide as a base. Tetramethylammonium hydroxide not only controls the silanol condensation by stabilising the pH but also the tetramethylammonium group improves the hydrothermal stability.

Das *et al*. (2000) also discussed the effect of various tetraalkylammonium bromide salts on the hydrothermal stability of MCM-41. They mentioned that the improvement in the hydrothermal stability of MCM-41 was due to tetraalkylammonium ion, which altered the electrostatic interactions between the cationic surfactant and the anionic silicate species surrounding the surfactant micelles. Tetraalkylammonium ion in aqueous silicate solutions enhances the abundance of symmetric cage-like polysilicate anions and also inhibits the hydrolysis of anions by forming a protective hydrophobic shell. The highly ordered structure of the samples prepared in this research was also due to these symmetric cage-like polysilicate anions. Das *et al*. (2000) reported that the tetrapropylammonium bromide based MCM-41 was highly ordered and had shown high hydrothermal stability at an optimum salt/surfactant ratio = 1.4.

XRD reflection peaks for TPABr (1.4), prepared in this research, **(**Figure 4.4, Page 80) agrees with Das *et al*. (2000) work. The pore wall thickness reported by them is 1.9 nm, and that for TPABr (1.4) prepared in this research was 1.8 nm. They also worked with tetramethylammonium and tetraethylammonium ions, which lead to improvement of hydrothermal stability attributed to an increase in the pore wall thickness.

In this thesis, the samples prepared at TEABr/CTAB = 0.8 exhibited an ultra-high surface area above 3000 m^2g^{-1} with a pore diameter of 2.6 nm and pore wall thickness of 1.7 nm. MCM-41 is a mesoporous material which characteristically exhibits a very high surface area ranging between 800 to 1000 m^2g^{-1}. It is not unusual for MCM-41 to have a surface area above this range; however, the long-range order is compromised at surface areas significantly higher than 1000m^2g^{-1}. The surface area reported by Das *et al*. (2000) for TEA (tetraethylammonium) ion-based MCM-41 is 1010 m^2g^{-1} with a peak pore diameter of 2.7nm and a wall thickness of 1.8nm. Qu and Gu (2014) prepared hierarchical MCM-41 spheres (HS) by sol-gel method using cetyltrimethylammonium chloride surfactant and sodium metasilicate as the silica source. They used a small amount of ethanol to tailor the morphology of their particles. The highest surface area they have reported is 2280 m^2g^{-1} with an average pore diameter of 5.6μm, showing a significant percentage of macropores. Their samples exhibited only one XRD reflection peak at (100) plane; the N_2 sorption isotherms were also transitional between type I and IV. The XRD patterns and physisorption behaviour of their samples had shown the lack of long-range order. The high surface area in their samples was attributed to the hierarchical structure of MCM-41 spheres. Thanabodekij *et al*., 2006 synthesised MCM-41 using tetraethylammonium bromide by varying temperature and pH during the synthesis. They achieved four distinct XRD reflection peaks for (100), (110), (200) and (210) planes confirming the presence of a well ordered hexagonal MCM-41 pore network. The highest surface area achieved was 2400m^2g^{-1} at tetraethylammonium bromide to surfactant ratio of 0.6 at 60^0C. The average pore diameter and pore-volume were 2.2 nm and 1.3 cm^3g^{-1},

respectively. The sample TEABr-MCM-41-(0.8) in this research is superior to all the samples mentioned above because it is prepared at low temperature and affords a surface area of 3000m^2g^{-1} not hitherto reported. The pore volume and pore diameter of TEABr-MCM-41(0.8) is also superior to the catalysts mentioned above.

Table 4.6 Highest reported surface areas versus MCM-41-TEABr-(0.8)

Sample	Surface area (m^2g^{-1})	Average pore diameter (nm)	Pore Volume (cm^3g^{-1})	Pore wall thickness (nm)
Das *et al*., (2000)	1000	2.7	0.8	1.8
Qu and Gu (2014)	2280	5600 (macroporosity)	1.15	n/a
Thanabodeekij *et al*. (2006)	2400	1.3	2.2	n/a
TEABr-MCM-41-(0.8)	3140	2.6	2	1.7

Table 4.6 shows a comparison of samples of reported with exceptionally high surface area against TEABr-MCM-41-(0.8). The above discussion concludes that MCM-41 samples with superior geometrical properties can be prepared by carefully choosing the salt to surfactant ratios. The optimum salt to surfactant ratio for tetraethylammonium bromide found in this research was 0.8. The sample TEABr-MCM-41-(0.8) afforded a surface area of 3000 m^2g^{-1}. XRD results showed that, in case of tetra alkyl ammonium bromide, changing the ratio of salt to surfactant does not significantly change the unit cell size; however, it has an essential effect on the degree of order and surface properties of MCM-41.

References

Alothman, Z.A. (2012) ‘A Review: Fundamental Aspect of Silicate Mesoporous Materials’, *Materials*, 5(12), pp. 2874.

Das, D., Tsai, C.M., and Cheng, S. (2000) ‘Improvement of hydrothermal stability of Mesoporous Molecular Sieves of MCM-41 type’, *Studies in Surface Science and catalysis*, 129, pp. 85

Monsoon, P.A. (2012) ‘ Understanding adsorption/desorption hysteresis for fluids in mesoporous materials using simple molecular models and classical density functional theory’, *Microporous and Mesoporous Materials*, 160, pp.47.

Nguyen, P. T. M., Do, D. D. and Nicholson, D. (2013) ‘Pore connectivity and hysteresis in gas adsorption: A simple three-pore model’, *Colloids and Surfaces A: Physicochemical and Engineering Aspects*, 437, pp. 56.

Kim, J.M., M, Jun, S. and Ryoo, R. (2002) ‘ Improvement of Hydrothermal Stability of Mesoporous Silica Using Salts: Reinvestigation for Time-Dependent Effects’, *The Journal of Physical Chemistry B*, 103(30), pp. 6200.

Khushalani, D., Kuperman, A., Ozin, G.A., Tanaka, K., Garces, J., Olken, M.K. and Coombs,N. (1995) ‘Metamorphic Material: Restructuring Siliceous Mesoporous Materials’, *Advanced Materials*, 7(10), pp. 842.

Kruk, M., Sayari A. and Jaroniec, M. (1999) ‘Influence of hydrothermal restructuring conditions on structural properties of mesoporous molecular sieves’, *Microporous and Mesoporous Materials*, 27(2), pp. 217.

Qu,Q. and Gu, Z. (2014) ‘Facile synthesis of hierarchical MCM-41 spheres with an ultra-high surface area and their application for removal of methylene blue from aqueous solutions’, *Analytical Methods*, 6(5), pp.1397.

Ryoo, R., Kim, J.M., Ko, C.H. (1998) ‘ Improvement of the structural integrity of mesoporous molecular sieves for practical applications’, *Mesoporous Molecular Sieves*, 117, pp. 151.

Sing, K. S. W. and Williams, R. T. (2005) ‘Physisorption Hysteresis Loops and the Characterization of Nanoporous Materials’, *Adsorption Science & Technology*, 22(10), pp. 773.

Sun, S., Liang, F., Tang, L., Wu, J. and Ma. C. (2017) ‘ Microstructural investigation of gas shale in Longmaxi Formation, Lower Silurian, NE Sichuan Basin, China’, *Energy Exploration and Exploitation*, 35(4), pp. 406.

Thanabodeekij, N., Sadthayanon, S., Gulari, E. and Wongkasemjit, S. (2006) ‘Extremely high surface area of ordered mesoporous MCM-41 by atrane route’, *Materials Chemistry and Physics*, 98(1), pp. 131.

Thommes, M. (2010) ‘Physical adsorption characterization of nanoporous materials’, *Chemie-Ingenieur-Technik*, 82(7), pp. 1059.

Thommes, M., Kaneko, K., Neimark, A.V., Olivier, J.P., Rodriguez-R, F., Rouquerol, J. and Sing, K.S.W. (2015) 'Physisorption of gases, with special reference to the evaluation of the surface area and pore size distribution (IUPAC Technical Report)', *Pure and Applied Chemistry*, 87(9–10), pp. 1051.

Varade, D., Joshi, T., Aswal., V.K., Goyal, P.S., Hassan, P.A. and Bahadur, P. (2005) ' Effects of salt on the micelles of cetyl pyridinium chloride', *Colloids and Surfaces*, 259(1-3), pp. 95.

Zeng, Y., Prasetyo, L., Tan, S.J., Fan, C., Do.D.D and Nicholoson, D. (2017) 'On the hysteresis of adsorption and desorption of simple gases in open-end and closed-end pores', *Chemical Engineering Science*, 158 (November2016), pp. 462.

Chapter 5

Hydrothermal Treatment

5.1 Hydrothermal treatment procedure

The sample MCM-41- TEABr-(0.8) was subjected to post-synthesis hydrothermal treatment. The sample was chosen because of its ultra-high surface area of 3000 m^2g^{-1}. Hydrothermal treatment was carried out by two methods, as mentioned below.

5.1.1 Hydrothermal treatment post-calcination of MCM-41

Sample MCM-41-TEABr-(0.8) was calcined at 550^0C at the rate of 1^0C/min for 6 hours. One gram of sample was mixed with 50ml of de-ionised water and transferred into a Teflon-lined PTFE container inside a "Parr Autoclave". The autoclave was heated at 80^0 C for 24 hours in an electric oven. The sample was labelled as MCM-41-80^0C Post-calcination. Another sample was prepared using the same procedure at 100^0C for 24 hours; the sample was labelled as MCM-41-100^0C Post-calcination. Hydrothermal treatment was also carried out at 120^0C, but the hexagonal structure of MCM-41 was lost; therefore, no further hydrothermal treatment was carried out at a higher temperature in the post-calcination hydrothermal treatment.

5.1.2 Hydrothermal treatment pre-calcination of MCM-41

Sample MCM-41-TEABr-(0.8) was subjected to hydrothermal treatment following the same procedure as described above in as-synthesised form at 80^0C, 100^0C,

120^{0}C, 140^{0}C and 160^{0}C. The samples were calcined after hydrothermal treatment under the same conditions as described above.

5.2 Results

The hydrothermally treated samples were characterised using XRD and nitrogen physisorption analysis to study the effects of post-synthesis hydrothermal treatment on the average pore diameter and pore wall thickness of MCM-41, which affect the hydrothermal stability of MCM-41.

5.2.1 Hydrothermal thermal treatment post-calcination

5.2.1.1 Powder X-ray Diffraction

Comparison of the XRD scans of samples; MCM-41-80^{0}C Post-calcination, MCM-41-100^{0}C Post-calcination and MCM-41-TEABr-(0.8) in Figure 5.1 shows the degree of long-range order in MCM-41 structure declined with post-calcination hydrothermal treatment. In the case of MCM-41-80^{0}C Post-calcination, three XRD reflection peaks were visible at (100), (110) and (200) reflection. The (100) reflection peak was small as compared to the sample MCM-1-TEABr-(0.8) whereas (110) and (200) reflection peaks were flattened and vague. The sample MCM-41-100^{0}C Post-calcination showed a further decline in the degree of long-range order than MCM-41-80^{0}C Post-calcination by exhibiting only one short XRD reflection peak at (100). The values of the interplanar distance d_{100} and the cell parameter a_0 in Table 5.1 show that the unit cell size decreased on hydrothermal treatment. The interplanar distance d_{100} and cell parameter a_0, however, remained the same for both MCM-41-80^{0}C Post-calcination and MCM-41-100^{0}C Post-calcination.

Table 5.1 Comparison of d_{100} and a_0 after hydrothermal treatment post-calcination samples		
Sample ID	**Interplanar distance d_{100} (nm)**	**Cell Parameter a_0 (nm)**
TEABr(0.8)	3.8	4.4
MCM-41 80	3.4	4
MCM-41 100	3.4	4

Figure 5.1 Comparison of XRD hydrothermal treatment post-calcination samples versus MCM-41-TEABr-(0.8)

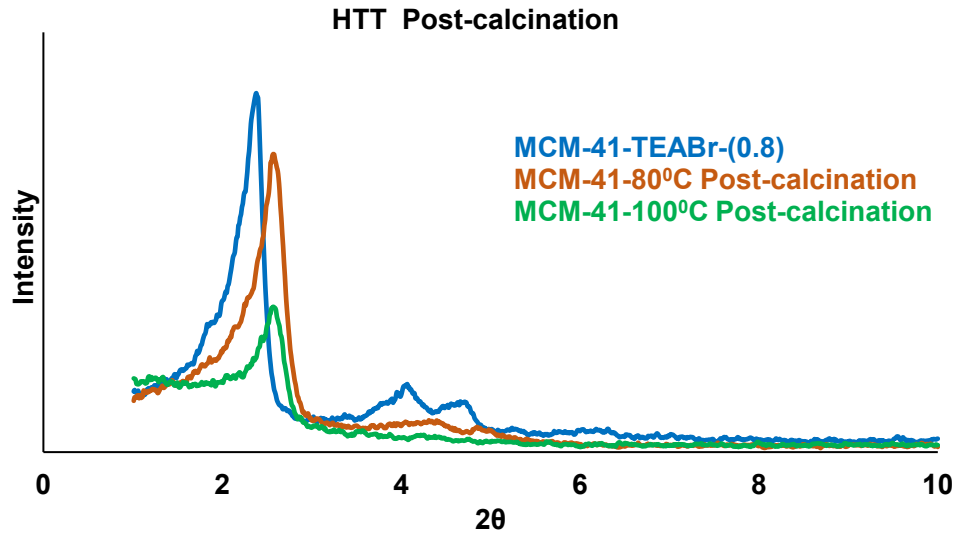

5.2.1.2 N2 physisorption studies:

Table 5.2 shows the comparison of nitrogen physisorption analysis results for MCM-41-80^0 C Post-calcination and MCM-41-100^{0}C-Post and the untreated sample MCM-41-TEABr-(0.8). The surface area significantly reduced from 3000m^{2}g^{-1} to 1434 m^{2}g^{-1} and 1185 m^{2}g^{-1} on hydrothermal treatment at 80^{0}C and 100^{0}C, respectively. The hydrothermal treatment at 80^{0}C resulted in a slight decrease in the pore wall thickness and the pore diameter of MCM-41-80^{0}C Post-calcination.

Table 5.2 Nitrogen physisorption analysis hydrothermal treatment post-calcination samples

Sample ID	Surface area (m^2g^{-1})	Pore volume (cm^3g^{-1})	Pore diameter P_d (nm)	Cell parameter a_0 (nm)	Pore wall thickness t = (a_0-P_d) (nm)
TEABr 0.8	3000	2.0	2.5	4.4	1.8
80	1434	0.9	2.3	4	1.7
100	1185	0.9	3.5	4	0.5

Since the unit cell size decreased after the hydrothermal treatment at 80^{0}C hence the shrinkage in the pore wall and pore diameter means silica restructuring occurred during hydrothermal treatment. MCM-41-100^{0}C Post-calcination exhibited a significant increase in the pore diameter along with a substantial loss in the pore wall thickness. Since the pore size expansion and the thinning of the pore wall occurred without expansion in the unit cell (constant d_{100} and a_0), it is inferred that the pore walls suffered silica dissolution (hydrolysis) during the hydrothermal treatment at 100^{0}C giving a false pretence of pore size expansion.

The hysteresis loops of the samples MCM-41-TEABr-(0.8), MCM-41-80^{0}C Post-calcination and MCM-41-100^{0}C Post-calcination are shown in Figure 5.2. The isotherms for the samples MCM-41-TEABr-(0.8) and

MCM-41-80^{0}C Post-calcination were of the type IV (a), and the hysteresis loops were of the type H1 representing highly ordered cylindrical mesopores with facile pore connectivity.

Figure 5.2 Hysteresis comparison post-calcination samples

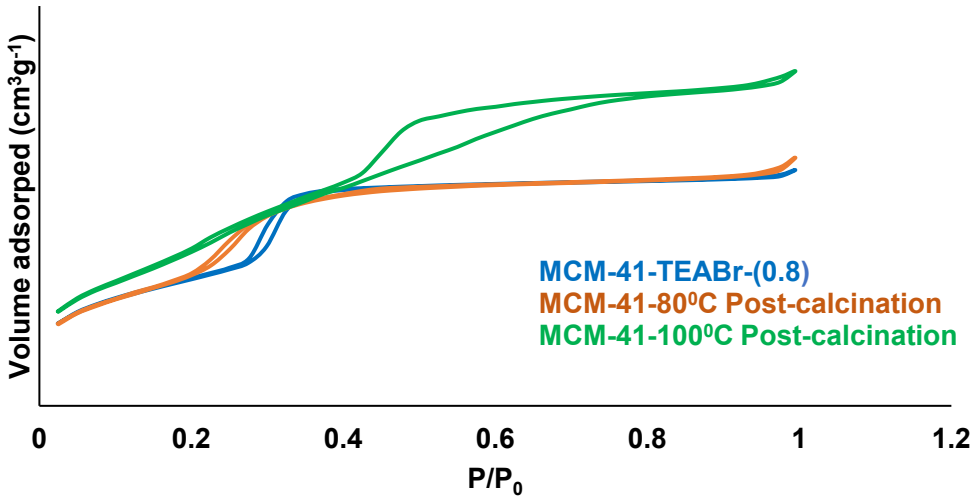

The isotherm of MCM-41-80^{0}C Post-calcination was flattened in comparison to the untreated sample MCM-41-TEABr-(0.8) due to a smaller average pore diameter than the untreated sample MCM-41-TEABr-(0.8). The sample MCM-41-100^{0}C Post-calcination exhibited a unique isotherm, on the adsorption branch it showed a steady increase in the volume adsorbed from the low P/P_0 to high P/P_0, unlike a standard type IV(a) isotherms which shows a sharp increase in volume adsorbed in the mesoporous region (P/P_0=0.2-0.4). The desorption branch followed a triangular path composite of the types H1 and H2 hysteresis loops indicating pore blocking in a narrow range of pore necks or cavitation induced evaporation. The adsorption and desorption paths and the triangular hysteresis suggests the sample MCM-41-100^{0}C Post-calcination has a bimodal pore size distribution, as shown in Figure 5.3 (b). The figure shows a bimodal pore size distributions with the smaller average pore diameter of 2.1 nm closer to

micropores and the average mesoporous diameter of 3.5-3.7 nm. The broad range of pore size distribution leads to pore connectivity problems (pore-blocking effect), causing restricted adsorption and delayed capillary evaporation forming a triangular hysteresis in Figure 5.2.

Figure 5.3 (a) Pore size distributions hydrothermal treatments post-calcination samples

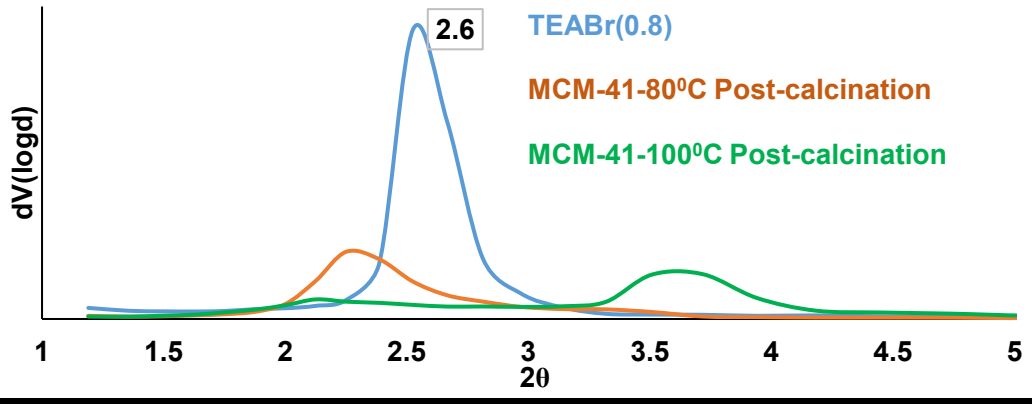

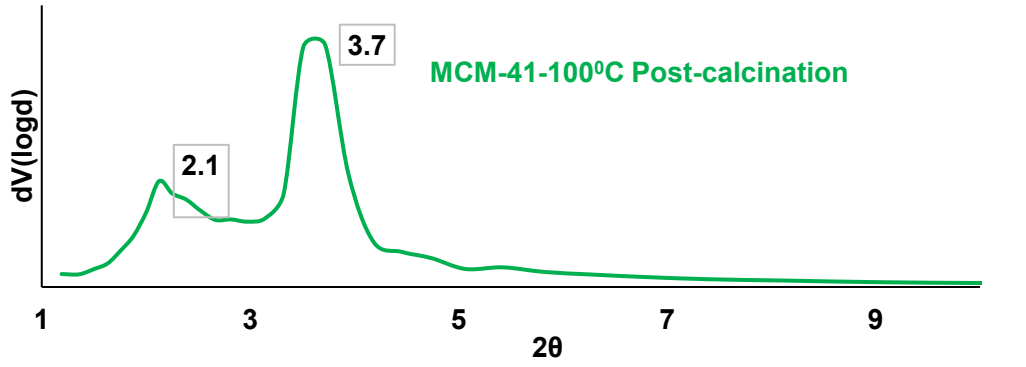

Figure 5.3 (b) Pore size distribution MCM-41-100⁰C post-calcination samples

5.2.2 Hydrothermal thermal treatment pre-calcination

5.2.2.1 Powder X-Ray Diffraction

Figure 5.4 (a) XRD comparison MCM-41 hydrothermal treatment pre-calcination.

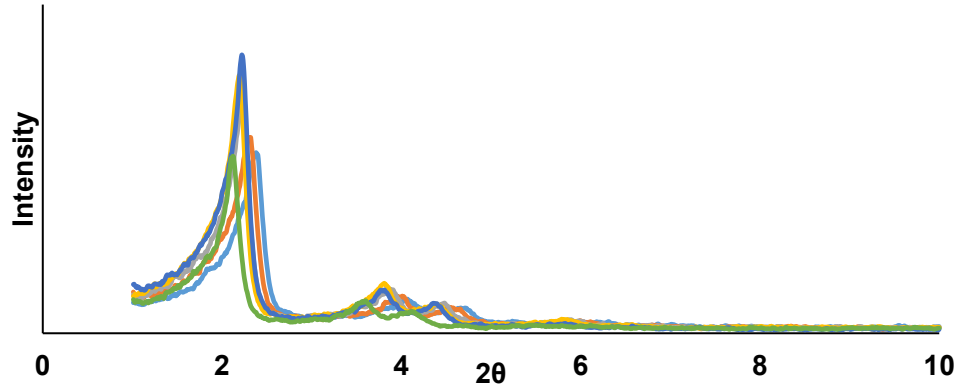

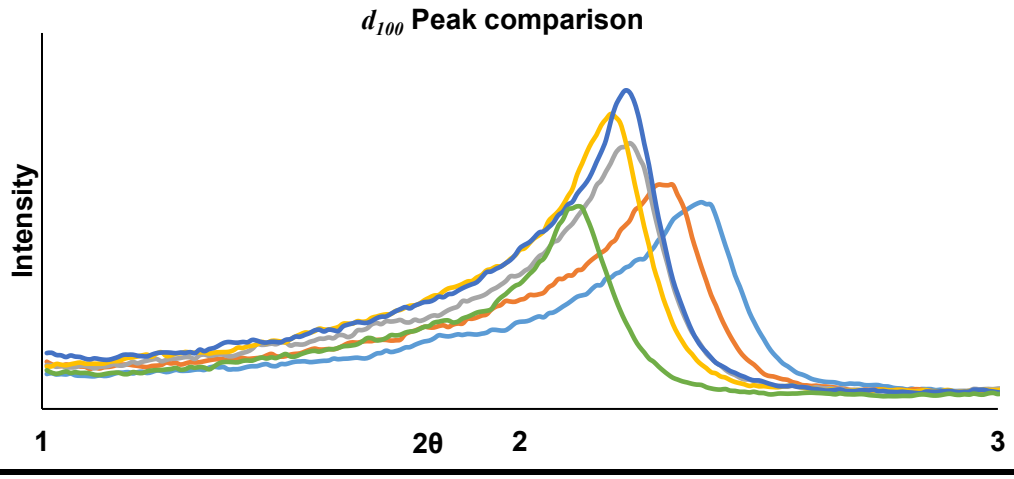

Figure 5-4 (b) XRD comparison of d_{100} peaks comparison MCM-41 hydrothermal treatment pre-calcination

TEABr(0.8)
MCM-41-80^{0}C Pre-calcined
MCM-41-100^{0}C Pre-calcined
MCM-41-120^{0}C Pre-calcined
MCM-41-140^{0}C Pre-calcined
MCM-41-160^{0}C Pre-calcined

The comparison of the XRD scans of pre-calcination hydrothermally treated samples in Figure 5.4 (a) and (b) exhibited four distinct XRD reflection peaks for the hydrothermal treatment temperatures of 80^{0}C, 100^{0}C, 120^{0}C, 140^{0}C and

160^0C. Hence, the pre-calcination hydrothermally treated samples endured high hydrothermal treatment temperatures.

MCM-41-140^0C Pre-calcination exhibited the most intensified (100) XRD reflection peak. Table 5.3 shows the interplanar distance $d_{100,}$ and cell parameter a_0 increased with increasing the hydrothermal temperature, showing an expansion in the unit cell increased with an increase in the hydrothermal treatment temperature.

Table 5.3 d_{100} and a_0 comparison of MCM-41 hydrothermal treatment pre-calcination

Sample ID	Interplanar distance d_{100} (nm)	Cell parameter a_0 (nm)
Batch 1 TEABr 0.8	3.8	4.4
80	3.9	4.5
100	4	4.7
120	4.1	4.7
140	4	4.7
160	4.4	5.1

5.2.2.2 *Nitrogen physisorption results:*

Nitrogen physisorption hysteresis loops in Figure 5.5 show all the isotherms are type IV (a) with H1 type hysteresis loops showing highly ordered cylindrical mesopores with facile connectivity.

Figure 5.5 Hysteresis comparison of MCM-41 hydrothermal treatment pre-calcination

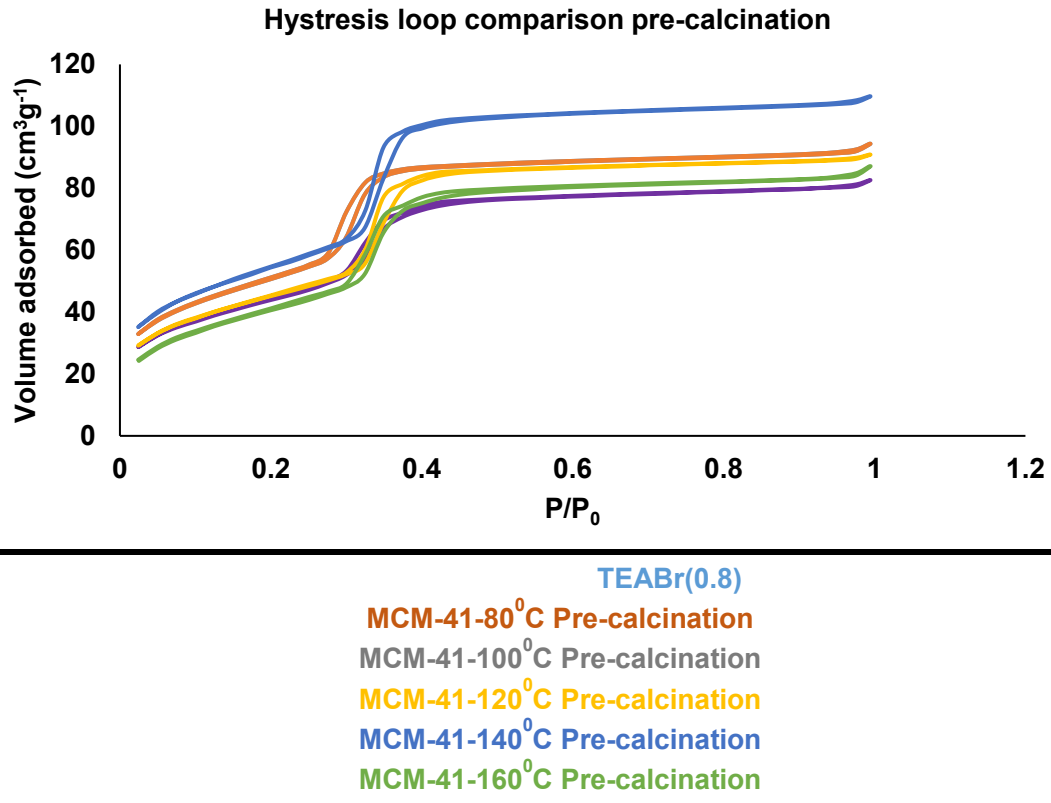

The N_2 physisorption data in Table 5.4 shows a substantial silica condensation occurred at a hydrothermal temperature of 80^0C by showing a 94% increase in the pore wall thickness of MCM-41- 80^0C-Pre-calcination . The average pore diameter, however, shrunk into the microporous range of 1.3 nm. The adsorption-desorption isotherms of MCM-41-80^0C Pre-calcination were, however, those of a typical mesoporous MCM-41, which means the sample had a majority of small size mesopores. Figure 5.6 shows a flat pore size distribution curve for MCM-41-80^0C Pre-calcination, suggesting the hydrothermal treatment time and the temperature was not enough for silica restructuring. The pore diameter

expansion was observed at hydrothermal temperatures of 100^0C and 120^0C. The results in Table 5.4 shows the hydrothermal temperature of 120^0 C, afford an optimum combination of the pore wall thickness, pore diameter and surface area. Hydrothermal temperatures above 120^0C have shown a decline in the surface area as well as the pore volume.

Table 5.4 N_2 physisorption analysis MCM-41 hydrothermal treatment pre-calcination

Sample ID	Surface area (m^2g^{-1})	Pore volume (cm^3g^{-1})	Pore diameter P_d (nm)	Cell parameter a_0 (nm)	Pore wall thickness t = (a_0-P_d) (nm)
TEABr 0.8	3140	2.6	2.5	4.4	1.9
80	734	0.4	1.2	4.5	3.3
100	1556	1	2.7	4.7	2.0
120	1821	1.23	2.8	4.7	1.9
140	1182	0.8	2.8	5.1	1.9
160	1151	0.8	2.8	4.4	1.6

Figure 5.6 shows the comparison of the pore size distribution of the hydrothermally treated MCM-41 samples. All samples showed very narrow pore size distribution except the sample MCM-41-80^0C pre-calcination, which had shown a very irregular pore size distribution ranging from 1 nm to 10 nm. Hence, the hydrothermal temperature of 80^0C was not sufficient for the optimum silica restructuring.

Figure 5.6 Pore size distribution MCM-41 hydrothermal treatment pre-calcination

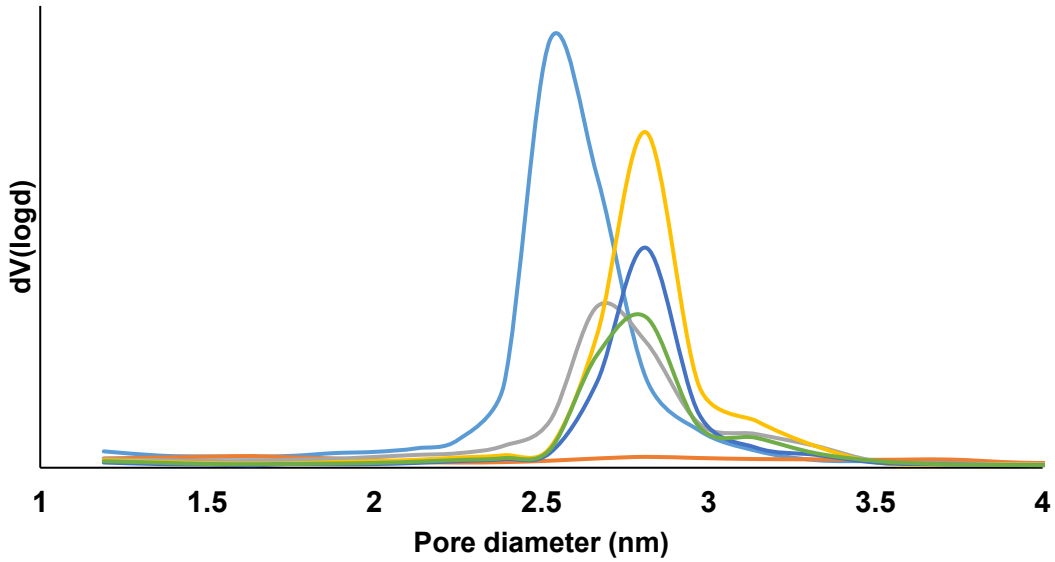

TEABr(0.8)
MCM-41-80^{0}C Pre-calcined
MCM-41-100^{0}C Pre-calcined
MCM-41-120^{0}C Pre-calcined
MCM-41-140^{0}C Pre-calcined
MCM-41-160^{0}C Pre-calcined

5.3 Hydrothermal stability test

Three samples; MCM-41-120^{0}C Pre-calcination MCM-41-140^{0}C Pre-calcination and MCM-41-160^{0}C Pre-calcination were tested for the hydrothermal stability. The hydrothermal stability test involved boiling the samples in water for 48 hours under reflux condition. Figure 5.7 shows the samples MCM-41-140^{0}C Pre-calcination and MCM-41-160^{0}C Pre-calcination exhibited only one XRD reflection peak at (100) plane, showing the MCM-41 hexagonal pore structure was deteriorated to some extent but not completely lost.

Figure 5.7 XRD comparison of hydrothermal stability

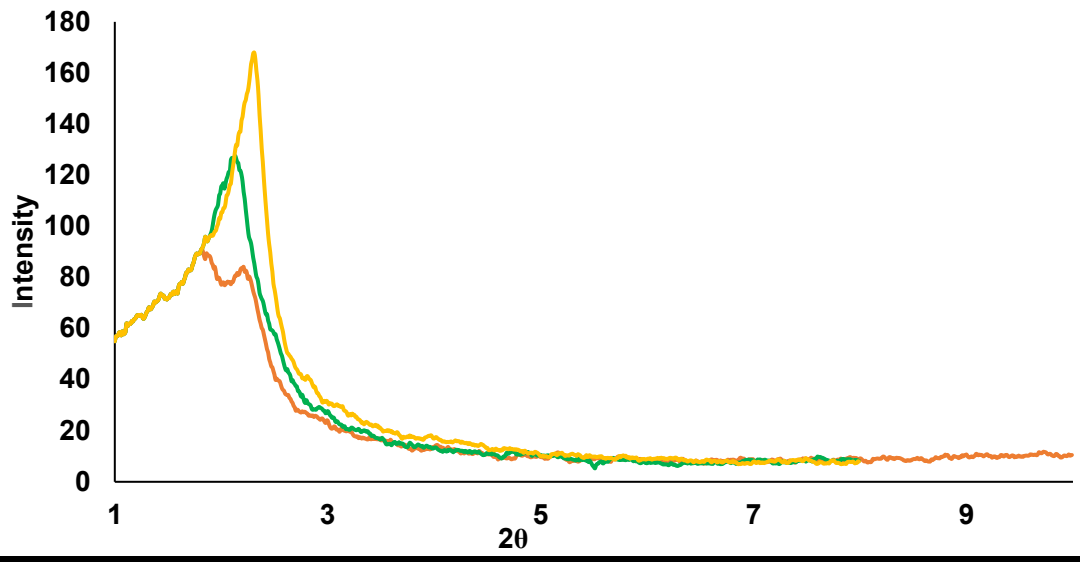

MCM-41-120^{0}C-Pre-calcination
MCM-41-140^{0}C-Pre-calcination
MCM-41-160^{0}C-Pre-calcination

5.4 Discussion

One of the prime features of MCM-41 is its high tendency for pore size engineering. MCM-41 samples with pore diameters as big as 10 nm have been reported in the literature. The stability of such materials is, however, in question (Beck *et al*., 1992). The art of pore size engineering involves careful management of several parameters, e.g. temperature, surfactant chain length, co-surfactants, post-synthesis hydrothermal treatment and additives. Literature shows MCM-41 samples with pore diameters as big as 4.5 nm have been synthesised by selecting an appropriate surfactant chain length. Pore diameters above 4.5 nm are highly desirable because catalysts and supports with bigger pore diameters and are capable of providing a confined environment to reactant molecules (where immobilised enzymes and chemically active colloids are involved) and catalytic activity enhancement (where modified/impregnated catalysts are

involved). Catalytic activity is believed to enhance in larger pore size mesoporous materials due to less extent of pore blockage after the deposition of species impregnated during the modification process. Supports/catalysts with larger pore diameters are also useful where larger molecules are involved in the chemical reactions (Kruk *et al.* (1999)). Besides larger pore size, another much desirable feature of a catalyst is its stability under extreme conditions of temperature and pressure. MCM-41 is reported to withstand temperature as high as 850^0C under dry conditions. It is also stable in a flow of 100% steam at 500^0C. However, it shows poor stability when it comes in contact with water and aqueous solutions (Das *et al*., 2000). Several attempts have been made to improve the hydrothermal stability of MCM-41 these include salt assisted MCM-41 synthesis by Das *et al*. (2000) as well as the present research discussed in detail with results in Chapter 4. Khushalani *et al.* (1995) carried out hydrothermal treatment of MCM-41 in the mother liquor (the synthesis gel) to improve the hydrothermal stability of MCM-41. The primary method used by Khushalini *et al*. (1995) has been adopted by many researchers to further study the hydrothermal stability, pore size expansion and N_2 physisorption behaviour. Table 5.5 shows a detailed comparison of the merits and demerits of each approach. The method termed as direct hydrothermal synthesis is just a standard MCM-41 preparation at higher temperature as described in Chapter 4. Post-synthesis hydrothermal treatment involves the method used by Khushalani *et al.*, 1995 and its further exploration by Kruk *et al*., $1999_{(a)}$; Kruk *et al*., $1999_{(b)}$ and Kruk *et al*., 2000 and Sayari *et al*.,1997; Sayari *et al*., 1998 and Sayari *et al*., 1999).

Table 5.5 Comparison of hydrothermal treatment techniques (khushalani *et al.*, 1995; Das *et al.*, 2000 ; Kruk *et al.*, 1999(a); Kruk *et al.*, 1999(b); 2000 and Sayari *et al.*, 1997; Sayari *et al.*, 1998 and Sayari *et al.*, 1999)			
Characteristics	**Direct hydrothermal Synthesis**	**Post-synthesis Hydrothermal Treatment in mother liquor**	**Salt Incorporation**
Pore Size	Enlargement obse-rved	Enlargement observed above 100%	Larger but inferior to hydrothermally Treated samples
Pore Size Distri-bution	Narrow	Narrow	Very narrow
Pore wall thickness	Decreases	Decreases due to degradation of the pore wall	Increases due to silica restructuring
Stability	Improved	Improved	Improved
Mesoporosity	Declines with time	Declines with time	Stable
Microporosity	Develops with time	Develops with time	Not observed
Structural Order	Improves then deteriorates	Deteriorates for extended periods	Very high
BET Surface Area	n/a	Significantly de-creases	Very high surface area
Unit Cell	Expands	Expands	Conserved
Control of Para-meters	pH and Temperature	pH, time and temperature	Salt/surfactant ratio and temperature

Hydrothermal stability enhancement is the key to improve the recyclability of MCM-41, which is very useful for its industrial-scale application. In the present study, it was observed in the N_2 physisorption results that the pore size expansion occurred with an increase in the pore wall thickness and unit cell size. The increase in the pore wall thickness and pore diameter along with the unit cell expansion confirmed silica restructuring occurred at 100^0C and 120^0C. Two theories are proposed in the literature regarding the pore size expansion by post-synthesis hydrothermal treatment. One theory suggests that water penetrates inside the MCM-41 channels and causes expansion of unit cells as well as the pore diameter. This theory maintains that water is the only expander which

causes pore expansion (Khushalani *et al.*, 1995). The second theory proposed by Sayari and Yang (1999) suggests; at high temperature during hydrothermal treatment CTMA (cetyltrimethylammonium) ion, present inside MCM-41 as a template decomposes into hexadecyldimethyl amine (HDMA). HDMA acts as a natural expander at high hydrothermal temperatures and causes the pore size and unit cell expansion in MCM-41. Both theories postulate that pore size expansion co-occurs with silica restructuring of the pore walls. It is also important to mention here that the silica restructuring is facilitated under basic conditions; therefore, hydrothermal treatment is usually carried out in the mother liquor (synthesis gel).

The high pH in the mother liquor inhibits the rapid condensation during silica restructuring, which gives rise to the weaker silanol bonds (Si-O-H) prone to hydrolysis. However, over extended periods of times, after completion of silica restructuring, basic pH promotes hydrolysis and pore walls start to dissolve in the hydrothermal solution, and the mesoporous structure is collapsed. Another vital role high pH plays is the decomposition of the surfactant into HDMA thus causing expansion in the pore diameter (Sayari and Liu 1997; Kruk *et al*., $1999_{(a)}$; Kruk *et al*., $1999_{(b)}$; Sayari and Yang, 1999 and Das *et al.*, 2000).

In the current study, it was observed that the sample MCM-41-160^0C Pre-calcination showed a minimal decrease in the pore wall thickness after hydrothermal treatment; the pore diameter, however, remained unaffected. A significant reduction in the surface area was also observed. It is interesting to know that even though the sample MCM-41-160^0C Pre-calcination exhibited a slight decrease in the pore wall thickness due to hydrothermal treatment, it exhibited the highest hydrothermal stability of all the sample. The

sample MCM-41-160^{0}C Pre-calcination withstood for 48 hours in boiling water under reflux. Exhibition of such hydrothermal stability suggests that during the hydrothermal treatment, the slight shrinkage in the pore wall thickness was further silica restructuring to its maximum.

However, when the hydrothermal treatment was performed at a higher temperature of 180^{0}C for four days, the whole structure was lost. Very high temperature and prolonged periods of hydrothermal treatment cause rapid silica restructuring and pore size expansion, thus damaging the structural integrity of the unit cell. Careful management of hydrothermal treatment temperature and time is crucial to avoid the undesirable consequences of hydrothermal treatment (Kruk *et al*., 1999$_{(a)}$; Kruk *et al*., 1999$_{(b)}$ and Sayari and Liu, 1997).

This study is a unique approach towards the improvement of the hydrothermal stability of MCM-41 using salt and hydrothermal treatment together, the samples thus prepared, exhibited high hydrothermal stabilities, narrow pore size distributions and very high surface areas. The hydrothermal treatment methods described in the literature were carried out in the mother liquor rather than the de-ionised water. In the current research, the samples were purposely not washed after filtration, to retain the same ingredients as there would have been in the mother liquor, i.e. the presence of tetraalkylammonium ions inside the micellar core to provide the hydrophobic cage-like silicate structures as discussed in Chapter 4 (page 94).

References:

Beck, J.S., Vartuli, J.C., Roth, W.J., Leonowicz, M.E., Kresge, C.T., Schmitt, K.D., Chu, C.T.W., Olson, D.H., Sheppard, E.D., McCullen, S.B., Higgins, J.B., and Schlenker, J.L. (1992) 'A new family of mesoporous molecular sieves prepared with liquid crystal templates', *Journal of the American Chemical Society*, 114(27), pp.10834.

Das, D., Tsai, C.M., and Cheng, S. (2000) 'Improvement of hydrothermal stability of Mesoporous Molecular Sieves of MCM-41 type', *Studies in Surface Science and catalysis*, 129, pp. 85.

Kruk, M., Jaroniec, M. and Sayari, A. (1998) 'Influence of hydrothermal restructuring on structural properties of mesoporous molecular sieves', *Microporous and Mesoporous Materials*, 27, pp. 217.

Kruk, M., Sayari, A. and Jaroniec,M. (1999) 'A unified interpretation of high-temperature pore size expansion processes in MCM-41 mesoporous silicas', *The Journal of Physical Chemistry* 103(22), pp. 4590.

Sayari, A. and Yang, Y. (1999) 'Expanding the pore size of MCM-41 silicas: use of amines as expanders indirect synthesis and post-synthesis procedures', *The Journal of Physical Chemistry*, 103(18), pp. 3651.

Sayari, A. and Liu, P. (1997) 'Characterization of Large-pore MCM-41 Molecular Sieves Obtained via Hydrothermal Restructuring', *Chemistry of Materials*, 9

Chapter 6

Conclusion and Future Work

6.1 Conclusion

This study was aimed at developing a very high surface area and hydrothermally stable MCM-41 material. MCM-41 material with an unprecedented high surface area of 3000 m^2g^{-1} was prepared by employing tetraalkylammonium bromide salts. These salts massively increased the surface area and degree of order of MCM-41 by enhancing the process of micellisation. Besides, tetraalkylammonium bromide salts instil a hydrophobic character inside the MCM-41 pore network by forming symmetric cage-like silicates structure around the silanol bonds (Si-OH). These cage-like silicates thus instil a hydrophobic character inside the MCM-41 structure, preventing the hydrolysis of silanol bonds (Si-OH) in MCM-41 structure during hydrothermal treatment. Another essential objective of this research was to expand the pore diameter of MCM-41 without compromising the high degree of order of MCM-41 structure. Expanding the pore diameter of MCM-41 is crucial for its potential application in the field of CO_2 utilisation into useful chemicals. Larger pore diameters mean better incorporation (grafting and impregnation) of active species inside the pore network of MCM-41 (Peter *et al.*, 2006). In the present study, the highest average pore diameter achieved is 2.6 nm, with a pore wall thickness of 1.9 nm.

Post-synthesis hydrothermal treatment technique was successfully employed to improve the hydrothermal stability of MCM-41 and pore diameter expansion. The hydrothermal stability of MCM-41 was significantly improved; however, the

expansion in the average pore diameter was limited. The effects of post-synthesis hydrothermal treatment on the pore diameter of MCM-41 depends on the medium in which hydrothermal treatment is carried out. De-ionised water and mother liquor are used as hydrothermal treatment media. Hydrothermal treatment in de-ionised water results in a small expansion in the pore diameter of MCM-41 due to pH value significantly lower than 11.

On the other hand, hydrothermal treatments carried out in the mother liquor display a significant increase in the pore diameter of MCM-41. The mother liquor is having pH 11 or above promotes the decomposition of cetyltrimethylammonium bromide (surfactant template) into hexadecyldimethyl amine (HDMA). HDMA causes an expansion in the pore diameter of MCM-41 by acting as a pore expander (Khushalini *et al*. 1995; Sayari and Liu, 1997; Kruk *et al.* 1998; 1999 Sayari and Yang, 1999; Brinker and Scherer, 1989; Das *et al.* 2000).

6.2 Future Work

6.2.1 Future Work Based on Vanadium Impregnation of MCM-41

It has been discussed in Chapter 4 that MCM-41 internal structure plays an essential role in the conversion of CO_2 into carbamates, which have vast applications as intermediates for the synthesis of pesticides, insecticides and as the building blocks for polyurethane synthesis (Srivastava *et al*., 2006). As discussed in Section 2.3, Li *et al.* (2011) reported, vanadium oxide catalysts exhibited very high catalytic activity for the synthesis of carbamates. To combine the advantages of the highly ordered pore network structure of MCM-41 and high activity of vanadium oxides, the highly ordered MCM-41 material with a surface area of 3000 $m^2g^{-1}$was impregnated using vanadyl acetylacetonate as vanadium precursor.

6.2.1.1 X-Ray Diffraction Analysis of V-Imregnated Samples

The samples were characterised using low angle and wide-angle XRD and nitrogen physisorption analysis. Figure 6.1 Low-angle XRD Comparison shows the comparison of the V-impregnated MCM-41 samples against the MCM-41-TEABr-(0.8).

Figure 6.1 Low-angle XRD Comparison

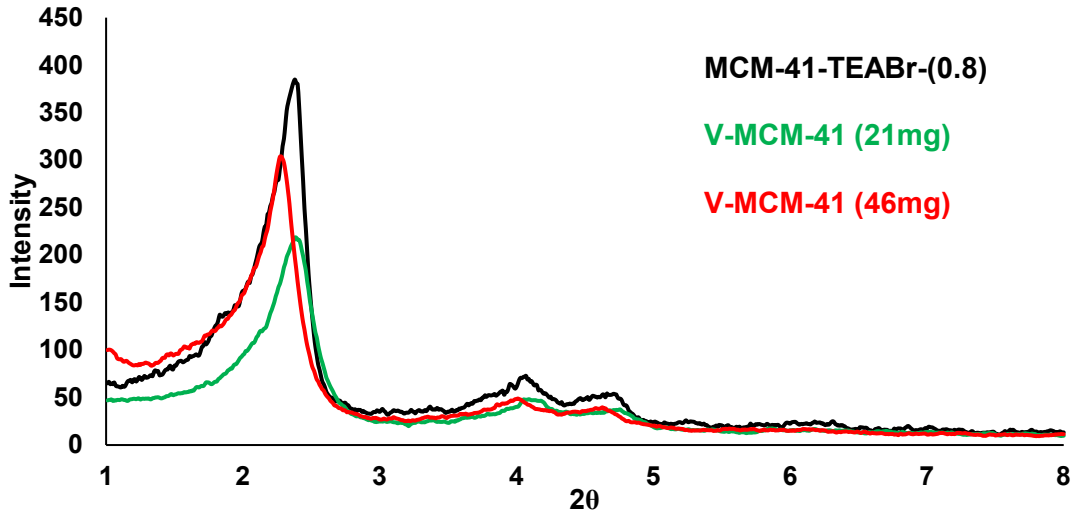

Table 6.1 d_{100} and a_0 comparison of V-impregnated samples versus MCM-41-TEABr-(0.8)

Sample ID	Interplanar distance d_{100}	Cell parameter a_0
MCM-41-TEABr-(0.8)	3.8	4.4
V-MCM-41 (21)	3.9	4.5
V-MCM-41 (46)	4.0	4.6

Three distinct XRD reflection peaks for (100), (110) and (200) planes reveal that the high degree of order of MCM-41 was preserved after the impregnation. Table 6.1 shows the values of the interplanar distance d_{100}, and the cell parameter a_0 increased slightly with increasing the amount of vanadium used in the

impregnation of MCM-41-TEABr-(0.8). Higher unit cell expansion indicates more vanadium oxide inside the silica framework.

The expansion in the unit cell is caused by the substitution of silicon (Si^{4+} ion radius, 0.114 nm) with vanadium (V^{5+} ion radius, 0.144 nm). The isomorphic substitution of vanadium ions into the silica framework is also evidenced by the absence of a crystalline phase of vanadium oxide in the XRD diffraction pattern within the 2θ range of 10^0 –80^o. Figure 6.2 shows the real wide-angle X-ray diffraction patterns of the two V impregnated samples. The absence of XRD reflection peak for vanadium species confirms that the dispersion of vanadium species over MCM-41 was highly uniform. Such a uniform dispersion of impregnated species is rarely observed. The exceptionally uniform dispersion of V species is due to the ultra-high surface area, extremely narrow pore size distribution and highly ordered structure of MCM-41-TEABr-(0.8).

Figure 6.2 Wide-angle XRD Comparison

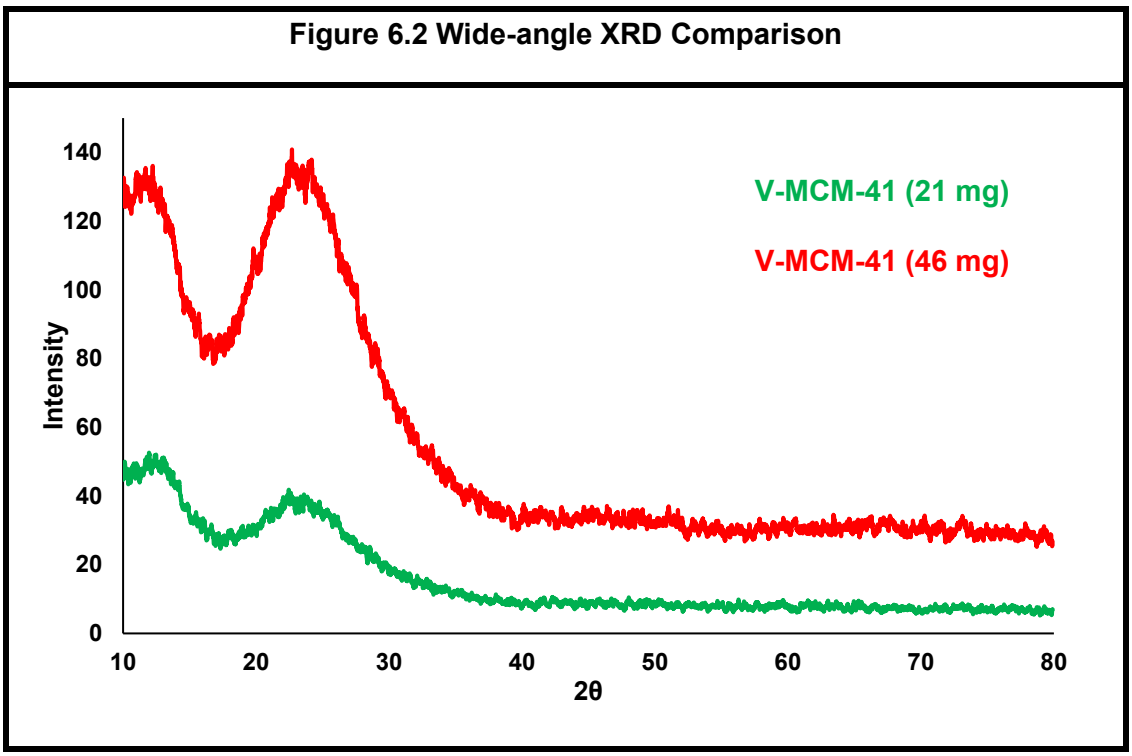

6.2.1.2 *Nitrogen physisorption analysis of the V- Impregnated samples*

Nitrogen physisorption analysis of the V impregnated MCM-41 samples revealed a very narrow H1 type hysteresis on a type IV isotherm, as shown in Figure 6.3. This type of isotherm represents a highly ordered mesoporous network with facile pore connectivity. It is interesting to note that the desorption branch of the isotherm intersected the adsorption branch below the lower closure point of the impregnated MCM-41. The gap between the adsorption and desorption branches below the lower closure point increased with increasing the amount of vanadyl acetylacetonate from 21 to 46 mg. It was observed that V-MCM-41 (46mg) showed a decrease of 5 cm^3g^{-1} in the volume desorbed at the end of desorption.

Figure 6.3 Adsorption desorption hysteresis comparison of MCM-41-TEABr-(0.8) and V-MCM-41 samples

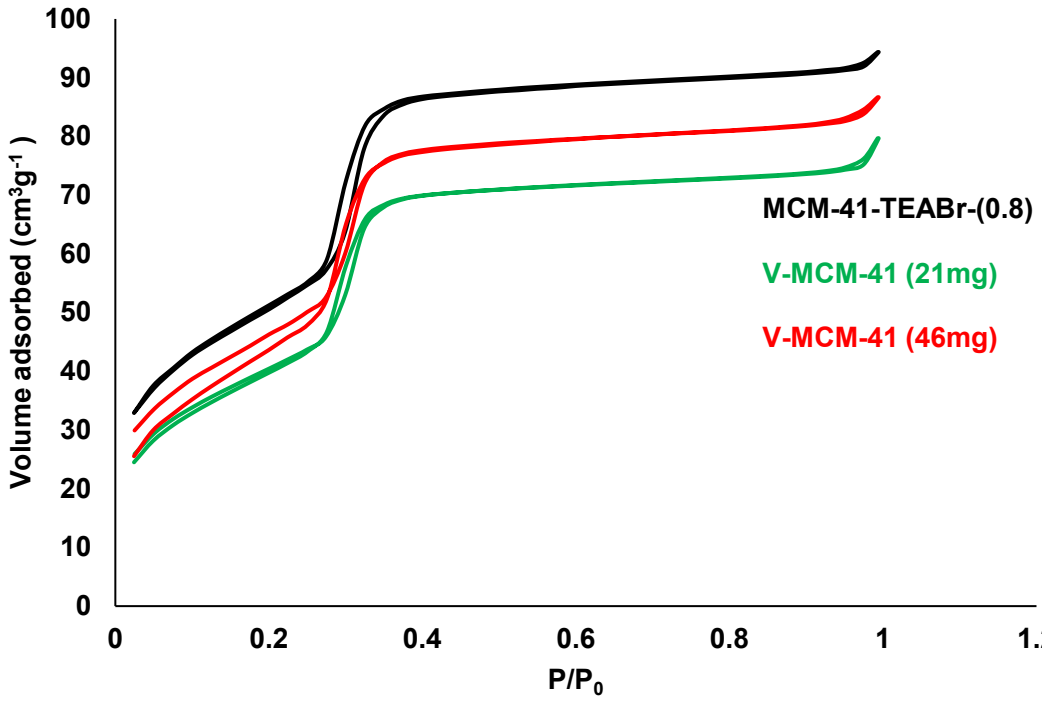

The decrease in the volume of nitrogen desorbed was due to the capillary condensation occurring inside mesopores during adsorption. Since the pore size was rather small, complete desorption was already tricky. The V species created a pore-blocking effect; therefore, complete desorption was not observed.

Figure 6.4 Pore size distribution comparison of MCM-41-TEABr-(0.8) and V-MCM-41 samples

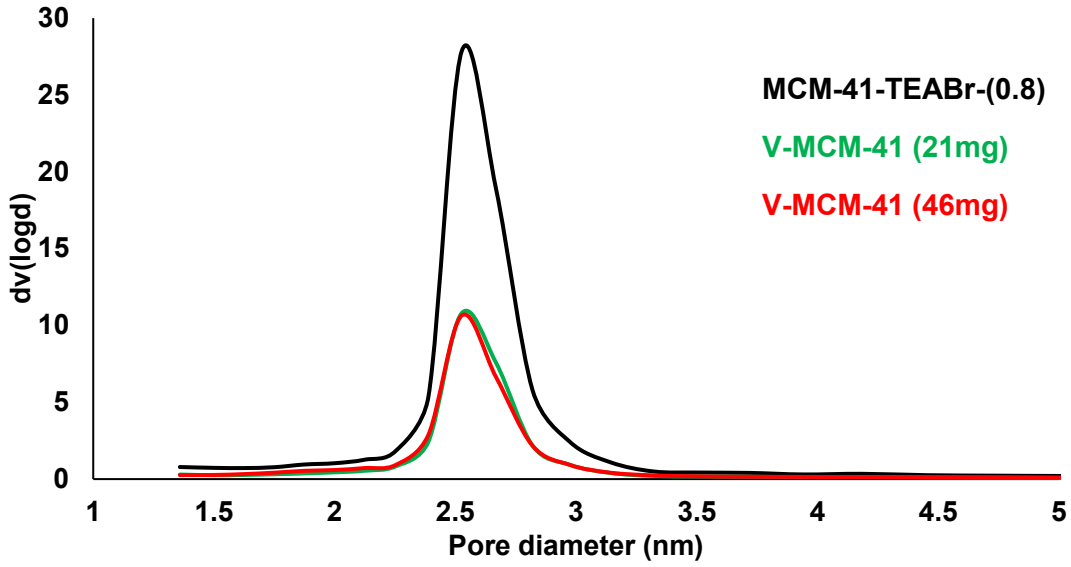

Figure 6.4 shows a comparison of the pore size distributions of the samples V-MCM-41(21mg) and V-MCM-41(46mg) against the MCM-41-TEABr-(0.8). The pore size distribution did not change significantly for the three samples. However, there was a slight shift towards smaller pores due to V impregnation.

Table 6.2 N_2 physisorption analysis

Sample ID	Surface area (m^2g^{-1})	Pore volume (cm^3g^{-1})	Average pore diameter P_d (nm)	Cell parameter a_0 (nm)	Pore wall thickness $t = (a_0-P_d)$ (nm)
TEABr 0.8	3000	2	2.5	4.4	1.9
V-MCM-41(21)	1240	0.8	2.5	4.5	2
V-MCM-41(46)	1270	0.8	2.5	4.6	2.1

N_2 physisorption data in Table 6.2 shows that the specific surface area and pore volume dropped significantly on the impregnation of MCM-41 with vanadium. However, no change was observed when the amount of vanadium precursor was increased, i.e. from 21mg to 46 mg. The significant decrease in the specific surface area and pore volume upon impregnation indicates a robust change on the surface and inside the pore network of MCM-41-TEABr-(0.8).

Linssen *et al*. (2003) discussed that after calcination vanadium is present as pseudo tetrahedral VO_x species linked together on the surface of MCM-41. Based on the findings of Li *et al.* (2011), these VO_x species can be used in CO_2 conversion into carbamates. In future, the V impregnated samples will be characterised by using X-ray photoelectron spectroscopy (XPS) to establish the oxidation state of the vanadium species present on the samples V-MCM-41 (21mg) and V-MCM-41 (46mg). The oxidation state of the V species will determine its catalytic capability towards the anticipated conversion of CO_2 into carbamates. The catalysts can then be tested for the conversion of CO_2 into carbamates and cyclic carbonates.

6.2.2 Future Work on MCM-41 as an adsorbent

Besides the CO_2 conversion into carbamates, the MCM-41 material prepared in this research can be used for CO_2 removal (using MCM-41 as an adsorbent). Carbon dioxide removal is not merely a crucial subject from the environmental point of view; it also has some industrial importance as well. CO_2 removal is mandatory in cryogenic plants to avoid CO_2 solidification. CO_2 is also the primary cause of corrosion in the pipelines in oil and gas plants. Commercially CO_2 removal is done by chemical absorption of CO_2 by liquid primary amines. The regeneration of liquid amines is cost-intensive due to the high heats of absorption. Also, the leakage of amines in the system may cause corrosion. Kamrudin and Alias (2013) have proposed MCM-41 modified with MEA (monoethanolamine) and DEA (diethanolamine) for CO_2 removal. They have mentioned that the presence of amines enhanced CO_2 adsorption on MCM-41 by creating CO_2 affinity sites promoting chemisorption, which appears as enhanced CO_2 adsorption. The author has concluded that the pore channels and the structure

of the amine group play a crucial role in the CO_2 adsorption. The physisorption of CO_2 occurs mainly inside the pore channels of the amine-modified MCM-41 whereas the chemisorption occurs inside the pore channels as well as the surface channels of the amine loaded MCM-41. The amine group hence makes the high surface area of MCM-41 useful for CO_2 adsorption. However, impregnation with amines fills the pore channels of MCM-41, thereby reducing the physisorption of CO_2 due to steric hindrance (particularly with the higher and branched alkyl chain ammines).

Given the relationship between the adsorption capacity of the pore channels and the surface area of MCM-41 discussed above, it is worthwhile to mention here that for the N_2 physisorption analysis of the sample MCM-41-TEABr-(0.8); 86mg of the sample was degassed at 300^0C for 3 hours before the nitrogen physisorption analysis. The weight of MCM-41-TEABr-(0.8) after degassing was reduced to just 5.3 mg. The substantial decrease in the weight of the MCM-41-TEABr-(0.8) sample, i.e. a loss of 80.7 mg of adsorbed vapours and gases hints the high adsorption capacity of the MCM-41 material synthesised in this research. It is noteworthy to mention here that such a substantial decrease in the weight was exhibited by the sample MCM-41-TEABr-(0.8) is in the absence of any chemical species. Further investigations are, however, required to study the CO_2 dynamics of the MCM-41 sample mentioned above. The ultra-high surface area and highly ordered pore network of MCM-41TEABr-(0.8) is responsible for such a large amount of adsorbed gases.

As another direction for future work, the adsorption capacity of the MCM-41 material prepared in this project should be assessed by CO_2 Temperature Programmed Desorption (TPD) using the CATLAB facility at the Department.

Thicker pore walls improve the hydrothermal stability of MCM-41. The pore wall thickness of the MCM-41 synthesised in this research has shown significant hydrothermal stability against boiling in water for 48 hours under reflux conditions.

6.2.3 Future work to further improve MCM-41 structure

The pore wall thickness also plays a crucial role in the hydrothermal stability of MCM-41. The pore wall thickness of MCM-41 depends upon the silica precursor used in the synthesis. The TEOS based materials show the highest degree of order in the MCM-41 structure the pore walls; however, the pore walls are not as thick as those obtained using fused silica. The degree of order in case of the fused silica-based mesoporous materials is, however not as high as that for TEOS based mesoporous materials. MCM-41 pore diameter can be expanded by carrying out post-synthesis hydrothermal treatment in the mother liquor as discussed on Page 116.

References:

Brinker, C.J. and Scherer, G.W. (1989) 'Hydrolysis and condensation: Silicates', *Sol-Gel Science*, U.S. : Academic Press, INC an imprint of Elsevier Science, pp. 97.

Das, D., Tsai, C.M., and Cheng, S. (2000) 'Improvement of hydrothermal stability of Mesoporous Molecular Sieves of MCM-41 type', *Studies in Surface Science and catalysis*, 129, pp. 85

Kamarudin, K.S.N., Alias, N. (2013) 'Adsorption performance of MCM-41 impregnated with amine for CO2 removal', *Fuel Processing Technology*, 106, pp. 332.

Kruk, M., Sayri, A. and Jaroniec, M. (1999) 'A unified interpretation of high-temperature pore size expansion processes in MCM-41 mesoporous silicas', *The Journal of Physical Chemistry*, 103(22), pp. 4590.

Kruk, M., Jaroniec, M. and Sayari, A. (1998) 'Influence of hydrothermal restructuring on structural properties of mesoporous molecular sieves', *Microporous and Mesoporous Materials*, 27, pp. 217.

Khushalani, D., Kuperman, A., Ozin, G.A., Tanaka, K., Garces, J., Olken, M.K. and Coombs, N. (1995) 'Metamorphic Material: Restructuring Siliceous Mesoporous Materials', *Advanced Materials*, 7(10), pp. 842.

Linssen, T., Cassiers, K., Cool, P., Vansant, E.F., (2003)' Mesoporous templated silicates: an overview of their synthesis, catalytic activation and

evaluation of the stability', *Advances in Colloid and Interface Science*, 103(2), pp. 121.

Li, J., Qi, X, Wang, L., He, Y. and Deng, Y. (2011) 'New attempt for CO_2 utilization: One-pot catalytic syntheses of methyl, ethyl and n-butyl carbamates', *Catalysis Communications*, 12(13), pp. 1224.

Peter, J.E., Harlick and Sayari, A. (2007)' Application of Pore-Expanded Mesoporous Silica. 5. Triamine Grafterd Material with Exceptional CO_2 Dynamic and Equilibrium Adsorption Performance', *Fuel Processing Technology*, 46(2), pp.446.